CHARACTERIZATION OF POST-PLASMA ETCH RESIDUES AND PLASMA INDUCED DAMAGE EVALUATION ON PATTERNED POROUS LOW-*K* DIELECTRICS USING MIR-IR SPECTROSCOPY

Sirish Rimal, B.Sc.

Dissertation Prepared for the Degree of

DOCTOR OF PHILOSOPHY

UNIVERSITY OF NORTH TEXAS

May 2016

APPROVED:

Oliver M. R. Chyan, Major Advisor
Willaim E. Acree, Committee Member
Michael Richmond, Committee Member
Samuel Tenney, Committee Member
Michael Richmond, Chair Department of Chemistry
Mark Wardell, Dean Toulouse Graduate School

Rimal, Sirish. *Characterization of Post-Plasma Etch Residues and Plasma Induced Damage Evaluation on Patterned Porous Low-k Dielectrics using MIR-IR Spectroscopy.* Doctor of Philosophy (Chemistry-Analytical Chemistry), May 2016, 132 pp., 4 tables, 80 figures, references, 142 titles.

As the miniaturization of functional devices in integrated circuit (IC) continues to scale down to sub-nanometer size, the process complexity increases and makes materials characterization difficult. One of our research effort demonstrates the development and application of novel Multiple Internal Reflection Infrared Spectroscopy (MIR-IR) as a sensitive (sub-5 nm) metrology tool to provide precise chemical bonding information that can effectively guide through the development of more efficient process control. In this work, we investigated the chemical bonding structure of thin fluorocarbon polymer films deposited on low-*k* dielectric nanostructures, using Fourier transform infrared spectroscopy (FTIR), X-ray photoelectron spectroscopy (XPS) and scanning electron microscopy (SEM). Complemented by functional group specific chemical derivatization reactions, fluorocarbon film was established to contain fluorinated alkenes and carbonyl moieties embedded in a highly cross-linked, branched fluorocarbon structure and a model bonding structure was proposed for the first time. In addition, plasma induced damage to high aspect ratio trench low-*k* structures especially on the trench sidewalls was evaluated both qualitatively and quantitatively. Damage from different plasma processing was correlated with Si-OH formation and breakage of Si-CH3 bonds with increase in C=O functionality. In another endeavor, TiN hard mask defect formation after fluorocarbon plasma etch was characterized and investigated. Finding suggest the presence of water soluble amines that could possibly trigger the formation of TiN surface defect. An effective post etch treatment (PET) methods were applied for etch residue defect removal/suppression.

ACKNOWLEDGEMENTS

First and foremost, I express my sincere gratitude to God for his continuous blessings upon my life for which I am able to reach this point. I greatly thank and appreciate my major research advisor Dr. Oliver Chyan for his support, steady encouragement, valuable advice, positive critiques, intelligence and guidance throughout my PhD career. I have gained invaluable lessons from him and his professionalism which has shaped me to become a better person and an ardent researcher, the qualities I strive to emulate in my professional as well as personal life.

I am also grateful to my committee members Dr. Michael Richmond, Dr. William Acree and Dr. Samuel Tenney for their time and continuous guidance. Special thanks to my current and past research members Dr. Yu, Dr. Pillai, Dr. Koskey, Dr. Mukherjee, Dr. Goswami, Dr. Abdelghani, Dr. Berhe, Po-Fu and Nick for making a great team, intellectual exchange, continuous encouragement and for every possible help throughout this journey. Many thanks to our research collaborators: Intel, Lam, TEL, ATMI, SRC for giving me opportunity to get expose to variety of research endeavors and also for their funding and financial support.

Finally, my utmost thanks to my dearest parents and family members for without them this journey would not have been possible. To my parents Madhav Rimal and Bina Rimal for all their unconditional love, support, encouragement, sacrifices and confidence in my education which I am truly indebted to.

I also wish to express my gratitude to those who have encouraged and supported me to complete this endeavor. God bless!

TABLE OF CONTENTS

CHAPTER 3: SPECTROSCOPIC CHARACTERIZATION AND BONDING STRUCTURE OF POST PLASMA ETCH RESIDUES ON TRENCH LOW-*K* STRUCTURES…………………..52

LIST OF TABLES

LIST OF FIGURES

CHAPTER 1

INTRODUCTION AND INSTRUMENTATION

1.1 Introduction

Innovation is the key to proliferate in microelectronic industry. New materials, novel technologies and structures are being devised regularly that often creates front news in the media. The power and performance of electronic goods such as computers and other electronic gadgets becomes higher while the cost decreases each year with the advent of new generation devices. This was possible because of the significant advancement in the technology of making the integrated circuit (IC), which is the heart of every electronic device.

An integrated circuit is essentially a combination of diodes, resistors and transistors devised on a small piece of semiconductor materials, normally silicon. Transistors, considered as the building block of integrated circuit, is simply a voltage controlled electrical switch that can be turned on or off. Several key inventions were important which allowed to today's IC manufacturing advancement. The first transistor invented was by Shockley, Bardeen and Brattain in 1947 at Bell Laboratories using gold, germanium and plastic [1-2]. These discrete transistors were made separately and were connected by wires, hence making many circuits was not feasible. The first integrated circuit where multiple transistors were connected on a single germanium substrate was fabricated by Noyce and Kilby in 1958, Figure 1.1. Germanium substrate was replaced soon after by silicon by the IC industry starting 1960s and most chips made today use silicon. Silicon is readily available (sand) and most importantly, forms stable and good quality natural oxide (SiO_2) which is required for metal-oxide-semiconductor (MOS) operation [3].

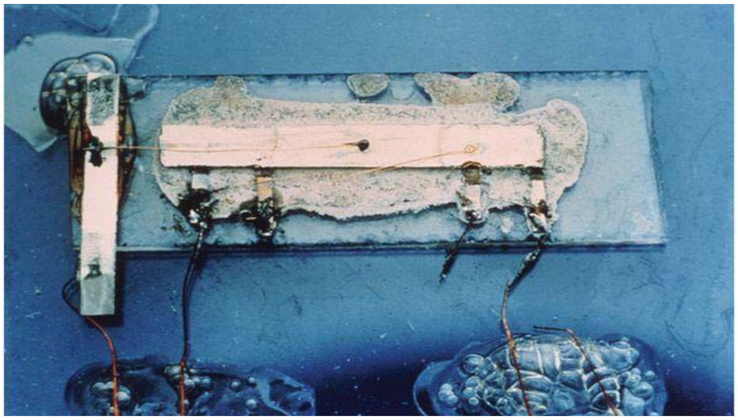

Figure 1.1 Jack Kilby's original integrated circuit [4].

Since then, the IC industry has grown exponentially where integration technology dramatically reduced the size of circuits and enabled higher complexity. The ability to incorporate many transistors on a single chip also led to substantially lower the manufacturing cost and to more complex integrated circuits. The miniaturization of transistors and the increase in integration density enabled more functionalities and improved transistor speed. Figure 1.2 shows that the number of transistors on an IC doubles every 18 to 24 months following Moore's law (1965) [5]. This exponential rate of increased integration density has been observed until now and will likely to follow for many more years to come.

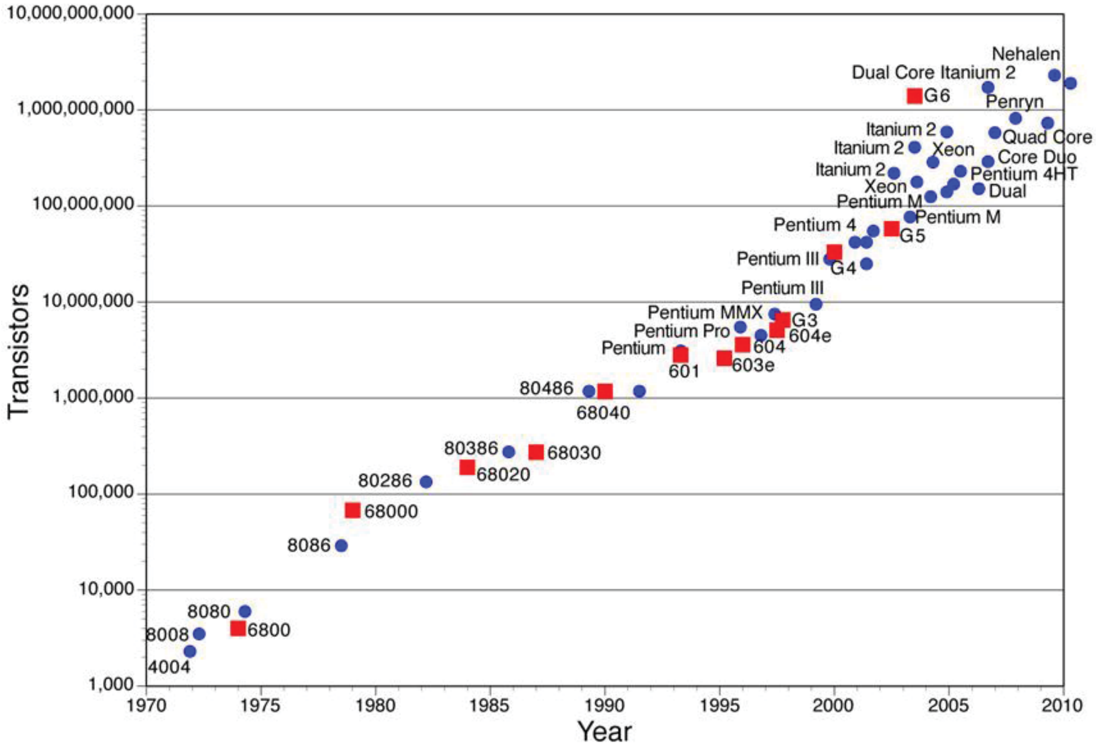

Figure 1.2 Number of transistors on a chip vs. year of introduction [6].

A number of processes are involved in making ICs. The first step involve fabrication of transistor level to the first metal level referred to as Front End Of Line (FEOL), followed by making interconnects (wiring) also called Back End Of Line (BEOL). Transistors are made in one level of the wafer while interconnects require several intricate levels with some advanced chips having up to 9 levels of interconnects. Interconnects essentially refer to wiring that connects different devices of the IC together and distribute signals. A cross section of an integrated circuit is shown in Figure 1.3. In the interconnect, the vertical wires connecting transistors and first metal level are called contacts, usually made of tungsten metal. All the other vertical wires after first metal level connecting different upper levels are called vias. The horizontal wires on the other hand are called metal lines.

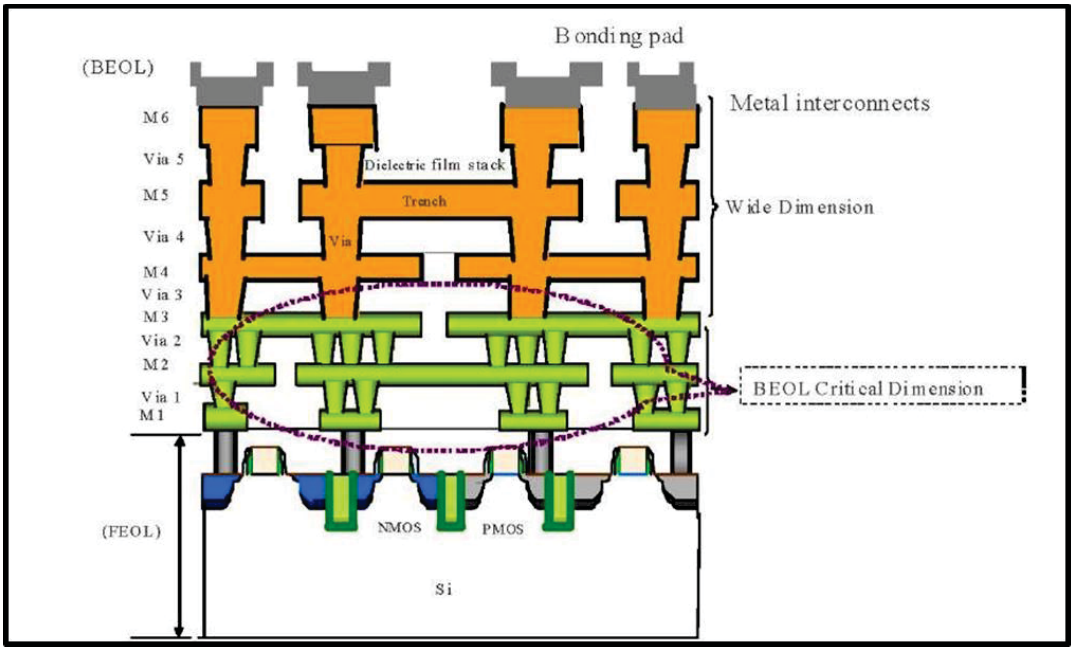

Figure 1.3 Schematic of transistor (FEOL) and interconnect wiring (BEOL) [7].

Each metal line (conductive wire) is insulated by an interlayer dielectric material otherwise short circuit can happen and creates chip malfunctioning. Aluminum was used as a conducting material for a long time as a metal of choice, and silicon dioxide (SiO_2) as an insulating material. However, as scaling continues, transistor switching speed no longer governs the overall IC performance, instead the effective device speed becomes more dominated by signal propagation through the interconnects [8-10], Figure 1.4. Hence, Resistance (R) and Capacitance (C) characteristics of the interconnect materials become an important factor, and dictates the RC delay time of the device. The RC delay time can be understood by the equation [10]:

$$RC = 2\rho\kappa\varepsilon_0 (4L^2/P^2 + L^2/T^2)$$

Where ρ = metal resistivity, ε_0 = vacuum permittivity, κ = dielectric constant of the interlayer dielectric, P = metal line pitch, T = metal thickness, and L = metal line length.

The equation clearly demonstrates that RC delay can be lowered using low resistivity metal and dielectric materials with low dielectric constant (*k*).

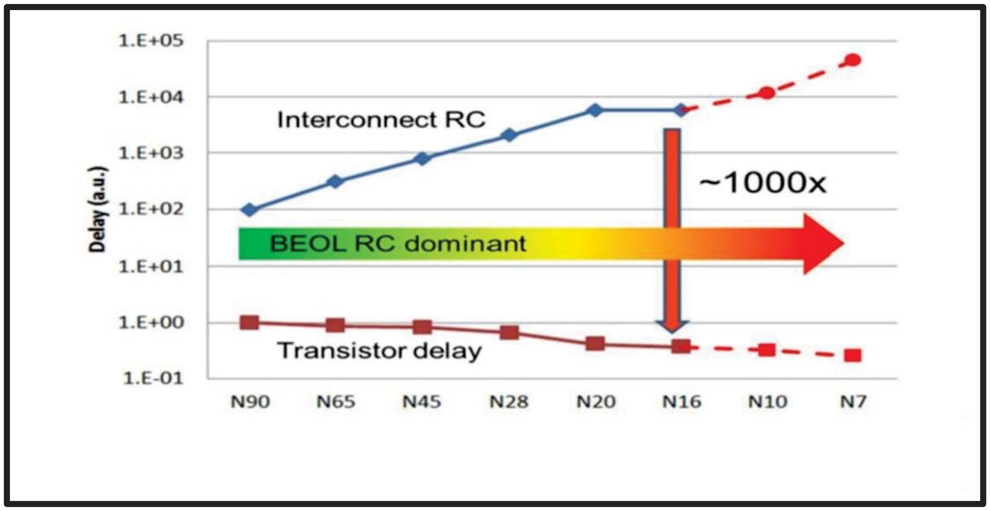

Figure 1.4 BEOL scaling issue for smaller technology nodes [11].

Copper (ρ = ~1.67 μΩ.cm) replaced aluminum (ρ = ~2.5 μΩ.cm) as the metal of choice for fabricating submicron interconnects by starting mid 90's. The primary advantages of copper is its higher electrical conductivity and higher electromigration resistance compared to aluminum [12-13]. Copper (Cu) interconnects in place of aluminum (Al) allowed continued miniaturization of devices alongside improvement of IC performance. The introduction of Cu as the interconnect material also led to adopt the damascene process as the industry standard, where the dielectric layer is deposited and patterned first followed by Cu deposition. The primary reason being unable to pattern Cu by plasma unlike direct patterning process for Al interconnect, because Cu does not form volatile Cu halides reaction products at low processing temperatures [14-15]. A simple schematic of single damascene processing of BEOL is illustrated in Figure 1.5. However, a more advanced process called dual damascene is used to pattern both trench and via layer at the same time because of its lower cost and better reliability.

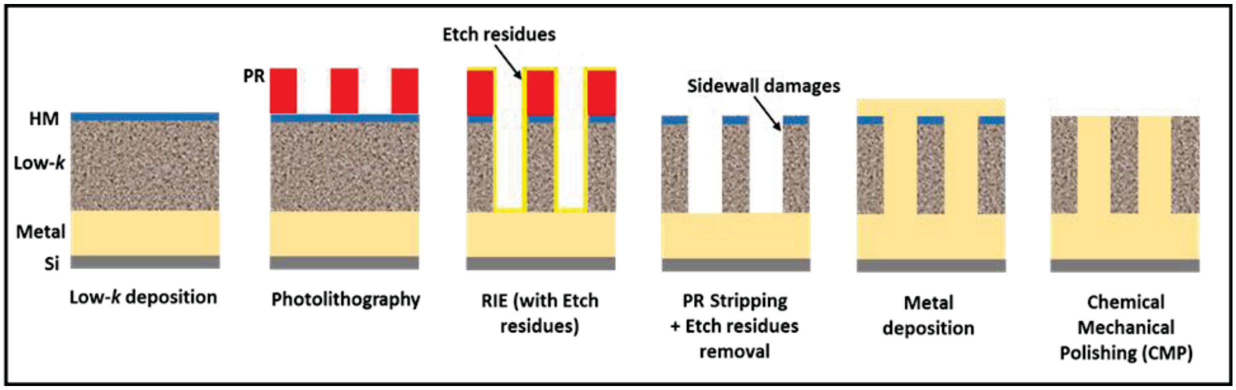

Figure 1.5 Schematic of single damascene processing.

In the damascene process, a designated thickness of ILD material is deposited by plasma enhanced chemical vapor deposition (PECVD) or by spin coating followed by photolithography patterning. In this process, a photo-sensitive organic polymer known as photoresist (PR) is selectively exposed to radiation using a mask which enables removal of exposed PR in an aqueous base, and leaving behind a defined pattern (trench or vias) where ILD is exposed. The pattern is then transferred onto ILD through hard mask using fluorocarbon (CF_x) based plasma chemistries. Hard mask is employed in the patterning process to protect the mechanically weak low-*k* (carbon doped silicon oxide) dielectrics underneath from plasma processing. Two types of masks can be employed depending on the type of low-*k* used: photoresist (softmask) and metallic materials usually titanium nitride (TiN) (hardmask). However the disadvantages of metal hardmask are the formation of metal containing etch residues which are difficult to remove, and mechanical stress upon fragile narrow lines patterned low-*k* dielectrics [16].

Anisotropic or directional plasma etching removes the exposed ILD creating trenches and vias while maintaining good etch profile (vertical sidewalls). One of the important aspect of plasma etching is to remove ILD and to maintain critical dimension (CD) intact with no/minimum damage to porous low-*k* [15]. The etching of carbon doped silicon oxide (SiOCH) low-*k* materials require fluorine (CF_x plasma) because Si is removed only by forming volatile SiF_4 reaction product, but not so much with other halides as etch rate is compromised [15]. Fluorine has been accepted because it forms volatile products with both Si (SiF_4) and Carbon (COF_2) which makes etching possible.

As a result of CF_x based plasma etching, a thin polymeric fluorocarbon residue (etch residues) is deposited on the trench sidewalls and bottom of low-*k* structure. The advantages of deposited polymer is to provide vertical etch profile, and also to seal the porous surface from unwanted plasma species penetrating into the bulk of porous low-*k* [15]. However, the post etch removal/ cleans of the thin fluorocarbon etch residues is essential for subsequent steps involved. Incomplete removal of the polymeric residues can have adverse effect such as poor adhesion to subsequent layers, fluoride diffusion, and poor electrical contact [17]. Many wet cleaning formulations [18-19] as well as dry chemistries [20-21] or the synergistic effect of both have been developed and explored over the years for efficient etch residues removal. Some formulations have shown better removal efficiency than the others, however aggressive chemicals also tend to etch away underlying porous low-*k* materials which changes features CD as well as causes low-*k* damage [22]. This is highly unacceptable especially for shrinking dimensions of the feature size.

A detailed characterization of post plasma etch residues is essential which enables better understanding of the chemical bonding structure of the etch residues. An improved understanding can facilitate to develop more efficient and less damaging wet/ dry etch residues removal formulations for small/narrow patterned nanostructures.

Further reduction of RC signal delay is achieved through introduction of lower dielectric constant materials, referred to as low-*k* dielectrics (*k* = 2-3) [23-24], which replaced conventional SiO_2 (*k* = ~4) as dielectric insulator. The reduction of dielectric constant of ILD material reduces cross talk between metal lines, which further allows improved high frequency signal propagation and close packing of interconnects. Lower dielectric constant (*k*) value can be obtained by reducing polarizability in the SiO_2 matrix, by replacing high polar Si-O bond with less polar bond such as C-C, C-H, Si-C, etc. Further lowering of *k* value ($k < 2.5$) as required by ITRS for 45 nm technology node and beyond [25] is by reducing their density by introducing porosity. Sacrificial porogens are introduced during deposition cycle which are then decomposed and desorbed during high temperature bake or by UV treatment, creating nanometer size pores. Introducing porosity in dielectrics offer advantage of lowering the *k* value, but also poses several integration challenges into microelectronic circuits [26-27].

Implementation of low-*k* dielectrics into the ICs has faced several integration and reliability issues, such as poor thermal and mechanical stability, moisture adsorption, chemical modification (especially during photolithography, etch/clean, metal deposition and planarization) and poor thermal conductivity [28]. Moreover, photoresist (PR) stripping following dry etching to create trench structures is one of the most harmful and challenging patterning steps for low-*k* materials. Oxidative plasma strip chemistries targeted for organic photoresist removal also tends to remove hydrophobic groups ($-CH_3$) from the low-*k* material, as low-*k* dielectrics are also chemically tailored to be hydrophobic. Plasma induced damage can chemically change hydrophobic low-*k* dielectrics into hydrophilic, although other detrimental effects such as densification and penetration of reactive species could be observed [15]. A hydrophilic low-*k* surface can adsorb water (*k* = ~80) causing to increase the overall *k* value, leakage current and total power consumption making the material unsuitable for integration [29-32]. Several processes have been developed and optimized to minimize the damaging effect from resist strip by changing the strip chemistry [33] and use of silylating agents to restore damage [34].

Besides the challenges of handling weak porous low-*k* materials, a lack of sensitive metrology to guide through the development of plasma treatments at various fabrication steps is a major hindrance. With the current scaling of devices beyond 22 nm technology node, the process complexity worsens even further and makes it difficult to quantify plasma induced damage especially from high aspect ratio (HAR) trench nanostructures. Hence it is imperative that the processes involved herein are carefully monitored and controlled that provides critical chemical bonding transformations information to facilitate rapid optimization of the process for successful process development.

The next step in the damascene process is the diffusion barrier deposition preferentially by plasma vapor deposition (PVD) to ensure no Cu diffuses through the porous low-*k* material. It is a conductive material that must be deposited on the trench sides and bottom as well as vias, and must exhibit good adhesion to low-*k*. A common diffusion barrier adopted for Cu integration is a thin conformal layer of Ta/TaN [35]. Following barrier deposition, a thin layer of Cu seed is deposited on top of barrier material followed by Cu metal filling in trenches and vias using electrochemical deposition (ECD) technique. Finally, chemical mechanical polishing (CMP) which exploits both physical and chemical means are used to remove excess Cu after metallization process. The process is then repeated for each subsequent wiring levels.

1.2 Instrumentation

Several thin film deposition techniques and surface characterization tools were utilized in this work. The working principles of the instruments/techniques used in the research will be discussed below in detail.

1.2.1 X-ray Photoelectron Spectroscopy (XPS)

X-ray photoelectron spectroscopy (XPS), also known as electron spectroscopy for chemical analysis (ESCA), is currently the most widely used technique for surface analysis. It is a highly sensitive measurement technique that can provide useful information about surface atomic composition, chemical/electronic states and structure of the matter [36]. The surface of the sample to be analyzed is irradiated with x-ray photons where photon (energy= hυ) interacts with a core shell electron with binding energy (E_B) leading to ejection of the electron. XPS spectra is obtained by measuring kinetic energy (E_k) and the number of ejected electrons from the top surface (0-10 nm) of the material being analyzed. The ejected photoelectron with kinetic energy E_k must travel a relatively large distance to the detector. Hence, XPS is conducted in ultra-high vacuum environment ($<10^{-7}$ torr) so as to minimize loss of kinetic energy of the photoelectron as well as to avoid collisions with other electrons or residual gas molecules. The basic components of XPS is shown in Figure 1.6 for illustrative purpose. XPS is a surface analysis technique to study different types of material surface both in as is as well as after treatment states with detection limit in parts per thousand range. In this work, XPS was utilized to obtain chemical composition of thin post plasma etch residues after etch process, carbon loss after different strip process, and surface modification from various dry/wet treatments.

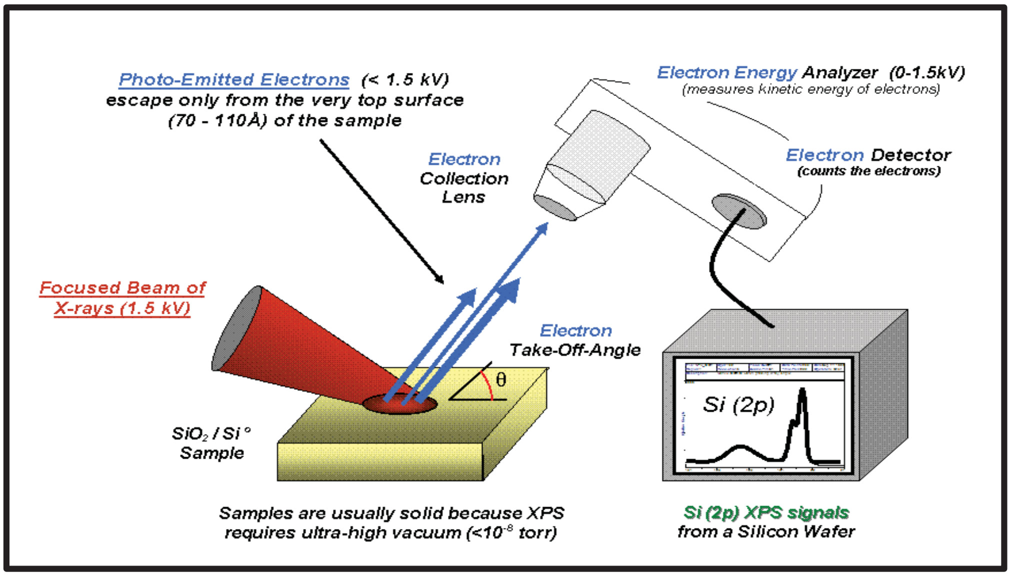

Figure 1.6 Basic components of XPS system (Wikipedia).

XPS technique is based on measuring the binding energy of ejected photoelectrons from the core shells when a monochromatic x-ray photon interacts with the sample surface. Binding energy is simply a measure of attractive force between the nucleus and the electron. The strength of this attractive force depends on the charge of the nucleus and no two elements share the same force, hence their electronic binding energies are different. This is important because it directly allows to identify the elements present on the sample surface under analysis. The intensity of spectral peak obtained also correlates to the amount of elements present in the material.

Beside the atomic composition, XPS also provides crucial information about the bonding environment of the atom from which photoelectron is analyzed. When an atom is bound to more electronegative atom, electrons on the outer shell are pulled toward the more electronegative atom which imparts a slight positive charge on the nucleus. This leads to a stronger pull to the inner core electrons by the nucleus and hence shift of binding energy to the higher energies occur. Same phenomenon occurs when an atom is bound to more electropositive atom but in reverse direction.

For example, binding energy of Si 2p electron is 99.15 eV [37], but when it is in oxide form (SiO_2) the Si 2p electron experiences a shift towards higher binding energy of 103.4 eV [37] because of the presence of electron withdrawing oxygen atom. A chemical shift toward lower binding energy would be seen if Si were to bind with some electron donating group.

All XPS measurements in our study were made using PHI 5000 Versa Probe scanning XPS system as shown in Figure 1.7. The instrument is equipped with a monochromatic Al Kα source (1486.7 eV) at 280 W with probing beam of 10 - 100 µm size for precise focusing of area under study. An Ar ion gun is available for surface cleaning and sputter depth profiling although non-destructive methods such as changing of emission angle and exciting photon energy are possible. The use of Ar ion gun also neutralizes insulating samples from charging effect. The emitted photoelectrons are collected and analyzed in concentric hemispherical analyzer (CHA) and multichannel detector respectively. First, the survey or low resolution scans are collected (0.5 eV, 50 ms/step) to identify all the elements on the sample surface followed by high resolution scans (0.05 eV, 200 ms/step) for each of the elements detected. Data collection was performed using PHI Explorer software (Physical Electronics, v3.4) and was analyzed using Multipak software (Physical Electronics v5.0A).

Figure 1.7 PHI 5000Versa Probe.

1.2.2 Fourier Transform Infrared Spectroscopy (FT-IR)

Infrared (IR) spectroscopy is the study of interaction of infrared radiation with matter. The whole of infrared region of the electromagnetic spectrum can be categorized into three sub-regions namely near IR, mid IR and far IR as shown in Table 1.1, with their respective wavelengths and energies.

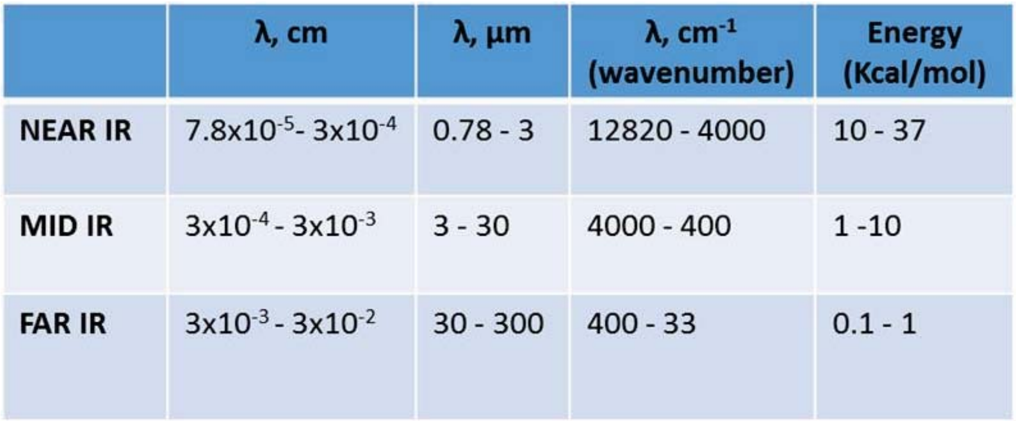

	λ, cm	λ, µm	λ, cm^{-1} (wavenumber)	Energy (Kcal/mol)
NEAR IR	$7.8x10^{-5}$- $3x10^{-4}$	0.78 - 3	12820 - 4000	10 - 37
MID IR	$3x10^{-4}$ - $3x10^{-3}$	3 - 30	4000 - 400	1 -10
FAR IR	$3x10^{-3}$ - $3x10^{-2}$	30 - 300	400 - 33	0.1 - 1

Table 1.1 Infrared region with their energies.

IR spectroscopy is a chemical analytical technique which measures infrared intensity versus wavelength (wavenumber) of light. The infrared spectrum of a sample is obtained by passing IR beam through the sample, where absorption occurs when the frequency of IR radiation is the same as the vibrational frequency of a bond. These absorptions are referred to as resonant frequencies which are related to bond strength and the mass of the atoms. Hence each functional group in a sample has its own characteristic vibrational frequency regardless of the structure of the rest of the molecule. Transmitted IR radiation exiting the sample reveals how much light has been absorbed at each frequency (wavenumber). The early stage Dispersive IR spectrometer uses monochromator to scan each wavelength passing the sample to plot IR spectrum and is time consuming. Fourier Transform IR (FT-IR) on the other hand measures all of the IR frequencies simultaneously to give rise to interferogram signal. The development of Michelson interferometer in the late 1800 led to Fourier Transform (FT) technology as illustrated in Figure 1.8.

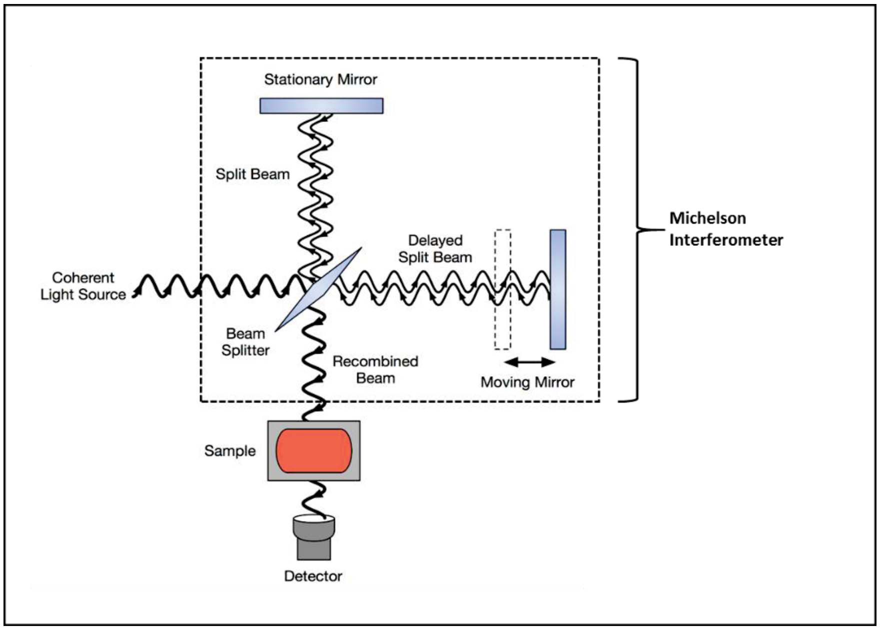

Figure 1.8 Schematic of Michelson's Interferometer (Wikipedia).

The Michelson interferometer utilizes a beamsplitter to produce interference spectra by splitting the incoming IR beam into two optical beams, so that one strikes a fixed mirror and the other onto a movable mirror. As the movable mirror travels a short distance (typically a few millimeters) along its path, the returning light beams off of the mirrors merge back together at the beamsplitter producing both constructive and destructive interferences. The recombined resulting signal is called the interferogram which has all the IR frequency encoded into it. The beam is transmitted or reflected off of the sample surface and finally detected by the detector. The interferogram signal is decoded with a mathematical function termed Fourier Transformation (FT) to give rise to a single beam spectrum of intensity vs. wavenumber. Fourier Transform is essentially the interconversion from one domain to another, eg distance/ time domain to frequency domain signals [38]. By coupling FT algorithm with the computer technology, FT-IR was finally feasible and could be used practically [39].

A single beam is basically a plot of total energy versus wavenumber, however is not a % transmission. The curve obtained is a culmination of source output, beamsplitter characteristics, detector response and other absorptions such as CO_2 and H_2O in atmosphere. FT-IR spectroscopy is a subtractive tool, hence a Transmittance (T) is obtained when a sample single beam is normalized against the single beam from background contribution as shown below:

$$T = I/I_0$$

where T is the transmittance, I is the sample single beam and I_0 is the background single beam. Absorbance (A) spectrum on the other hand can be calculated from transmittance spectrum using the following equation:

$$A= -\log (\text{Transmittance})$$

$$A= \log I_0/I = \text{Log [Background/Sample]}$$

The resultant Transmittance or Absorbance spectrum should be free of all instrumental and environmental contributions and only have the features contributing from the sample.

FT spectroscopy provides major advantages in its throughput, resolving power, reproducibility and the time needed to take a spectrum. Since FT-IR spectrometer detects all wavelengths at once, the speed and sensitivity increases giving Felldget's advantage. Also, there is a much greater signal-to-noise ratio (SNR) because the IR radiation passes directly through the sample and to the detector without radiation attenuation giving throughput or Jackquinot's advantage.

1.2.2.1 Attenuated Total Reflection Infrared Spectroscopy (ATR-IR)

The origin of attenuated total reflection (ATR) spectroscopy dates back to the early 1800's when Newton observed the phenomenon of evanescent field which is the basis of internal reflection spectroscopy [40]. Attenuated total reflection (ATR) has grown into a widely used technique in infrared spectrometry, where FT-IR is coupled with ATR technique to provide an extremely sensitive means of probing surface of the substrate of interest [40]. ATR-IR is a technique whereby a sample is placed in contact with an internal reflection element (IRE) and a spectrum is collected as a result of that contact. Here, the radiation is not transmitted through the sample unlike many other IR sampling techniques, hence the sample does not have to be thin enough to allow transmission of the radiation. One of the major benefit of ATR sampling technique comes from the very thin sampling pathlength and depth of penetration of IR beam into the sample [38]. This is in contrast to traditional FT-IR sampling by transmission where the IR beam passes through the sample and the effective pathlength is determined by the thickness of the sample. The core of ATR technique is the IRE that has a relatively high refractive index compared to the probing sample and is transparent to infrared beam. Table 1.2 below shows some of the commonly used materials as IRE's (also called ATR crystal) for ATR technique.

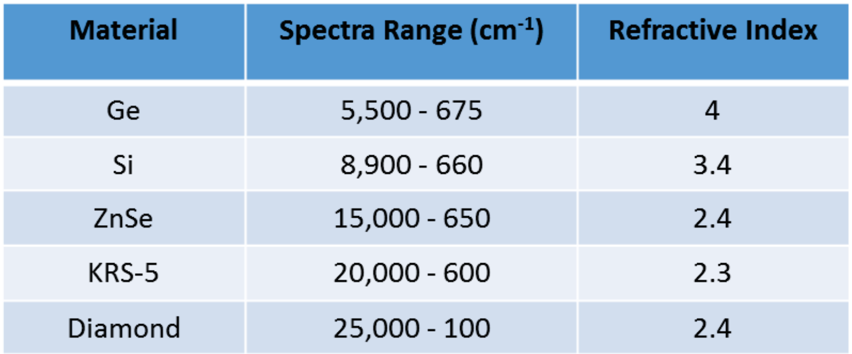

Material	Spectra Range (cm^{-1})	Refractive Index
Ge	5,500 - 675	4
Si	8,900 - 660	3.4
ZnSe	15,000 - 650	2.4
KRS-5	20,000 - 600	2.3
Diamond	25,000 - 100	2.4

Table 1.2 Common internal reflection elements (IRE).

The IR beam is allowed to pass through the bevel face (parallelogram or trapezoidal shaped) of ATR element and propagates along the waveguide generating an evanescent field at the points of contact to the surface. Some of the energy of the evanescent field is absorbed by the sample and the reflected radiation is detected by the detector. The phenomenon of internal reflection occurs when two mediums in contact have different refractive indices, optically denser medium (IRE) with higher index than the optically rarer medium. The incident IR radiation in the denser medium (refractive index n_1) undergoes total internal reflection at the interface with respect to the rarer medium (refractive index n_2), when the angle of incidence Θ exceeds the critical angle $\Theta_{c.}$ The critical angle is defined by the equation [41].

$$\Theta_{c} = \sin^{-1} (n_2/n_1)$$

Figure 1.9 below illustrates the phenomenon of IR radiation propagating through the ATR element.

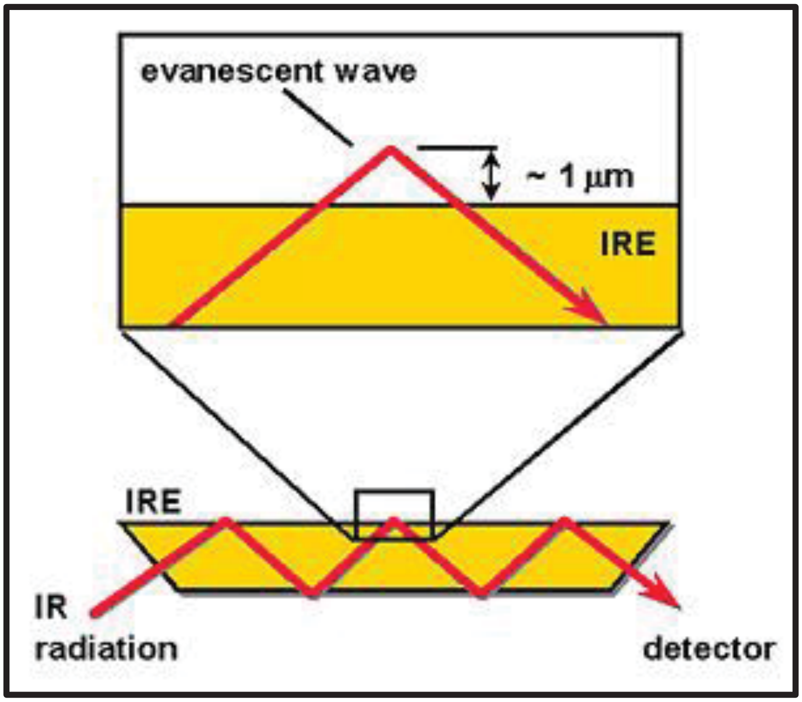

Figure 1.9 Propagation of IR radiation through an ATR element [42].

The field penetrates the rarer medium (air or sample) and decays exponentially with distance (z) perpendicular to the sample surface. The decay rate of the evanescent wave correlates directly to the wavelength of the IR radiation. The strength, E, of the field is a function of distance (z) from the surface expressed as:

$$E = E_0 \, e^{-z/\mathbf{d}_p}$$

where E_0 = field strength at the surface and d_p = depth of penetration of evanescent wave into the sample. The penetration depth (d_p) is defined as [38]:

$$d_p = \lambda/\{2\pi n_1[\sin^2\theta - (n_2/n_1)^2]^{1/2}\}$$

where λ = wavelength of incident radiation, the refractive index of the IRE (n_1), the refractive index of the sample (n_2), and the angle of incidence θ. As shown, the strength of the evanescent wave decays rapidly as it progress from the surface of the ATR element. Typical depth of penetration in ATR ranges from ~ 0.5 – 5 microns depending on the experimental conditions.

The number of reflections (R) of a given length of the crystal (L) and thickness (W) is given by an expression:

$$N = (L/W)(\cot\theta)$$

The interaction of the field with the interface leads to signal enhancement for each internal reflection. Hence this technique has way more sensitivity compared to conventional transmission and the sensitivity of detection for minor components is greatly enhanced.

1.2.3 Scanning Electron Microscopy (SEM)

SEM is a very powerful microscope that can magnify the surface topography of a sample by more than 100,000 times and with resolution of < 10 nm. Optical microscopes on the other hand are only capable of magnifying up to 1000 times and its resolution is limited by diffraction of light

[43]. Visible light with wavelength 400 – 700 nm cannot be used to visualize features of smaller size. Extreme UV (EUV) with wavelength 100 – 10 nm and x-rays with < 10 nm are not limited by diffraction when the feature size is above their wavelength, however EUV is absorbed and x-ray will penetrate most of the materials. Electron beams are ideally suited for the imaging from the surface because electrons can penetrate, or escape from only the outermost layers [44], hence producing clear contrast usable image.

The SEM comprise of an electron gun (electron source), a magnetic lens to control the size of the electron beam, a scanning coil to move electron beam in a controlled fashion, and detectors as illustrated in Figure 1.10. The entire process takes place in high vacuum.

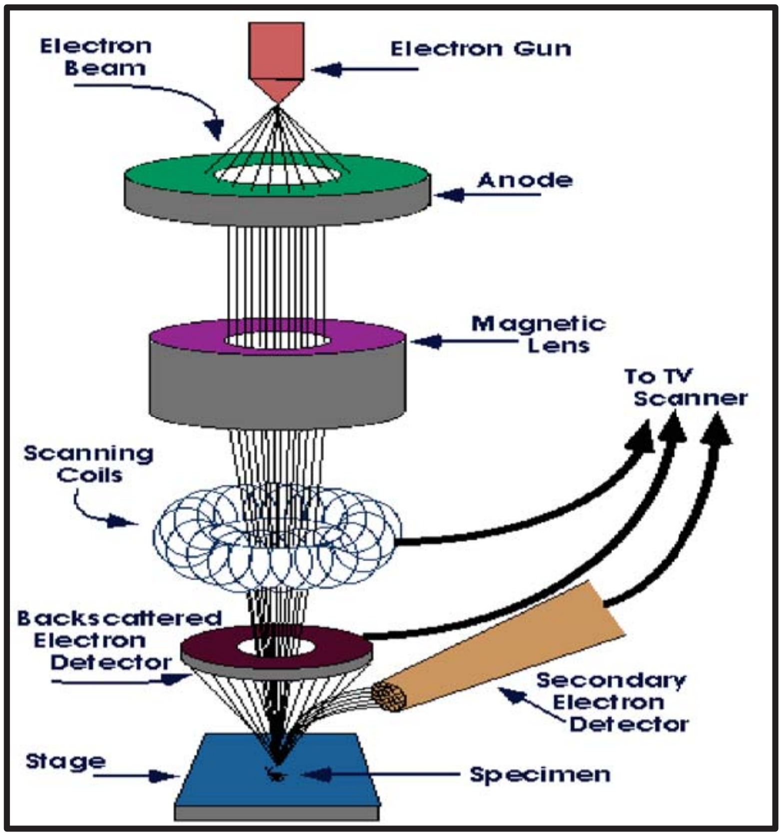

Figure 1.10 Schematic of SEM (Iowa State SEM Homepage).

An electron beam is produced at a cathode filament usually made of tungsten with electrons energy between 1 – 40 keV. The cathodic filament is maintained at a potential of 1 – 50 kV with respect to the anode where electron beam is accelerated towards. The wider electron beam next encounters an electromagnetic lens which squeezes the beam to a diameter of 5 nm or less for better focusing. The beam passes the deflection coils (scanning coils) and finally to the sample. In SEM, only one small spot is irradiated with the beam unlike light microscope where the entire sample is irradiated simultaneously. The electron beam is moved in small steps (in nm) by the process called rastering where a small electric field is applied and the beam is allowed to move in x and y coordinates. This allows to analyze the entire sample simply by scanning the electron beam. The coils that utilize this process for moving electron beam is called the scanning coils.

Once the electron beam hits and interacts with the sample surface, three different phenomena occurs. Some of the electrons will be released from the sample called secondary electrons which normally has lower energy (< 50 eV) compared to the primary electrons. The number of secondary electrons released decreases with probing depth, hence electrons from the surface that are easy to escape arrive at the detector for imaging purpose. Some of the primary electrons are scattered back called back scattered electrons after interacting with the sample. A detector positioned appropriately can be used to obtain information from back scattered electrons. A third phenomenon comes about when an electron in the inner shell is ejected out of an atom by the primary electron. Electron from an outer atomic shell falls into the vacated inner shell emitting x-rays, produced by the difference in energy between the two shells. The energy difference and therefore the x-rays generated are specific to each element in the sample, which can be evaluated to obtain chemical composition of the surface. A detector commonly used for this purpose called

Energy dispersive X-ray Spectroscopy (EDS) can be coupled with SEM for better elemental analysis of the surface [45].

1.2.4 Thin Film Deposition

A thin film deposition is the technology of depositing a very thin film of material on a given substrate. The thickness can range anywhere between a fraction of nanometers to several micrometers. Thin film deposition has a huge application in the fabrication of microelectronic devices, where precise control of layer thickness is of great importance. Two different thin film deposition techniques namely chemical vapor deposition (CVD) and physical vapor deposition (PVD) are discussed below.

1.2.4.1 Chemical Vapor Deposition (CVD)

Thin film deposition by CVD process is a chemical process, where the material to be deposited is in the gaseous (often a halide or hydride of the element) form. The CVD chamber is equipped with valves to supply gases at controlled rates and also to create vacuum. It also has a facility for controlled substrate heating. A simple schematic of a CVD chamber is shown in Figure 1.11.

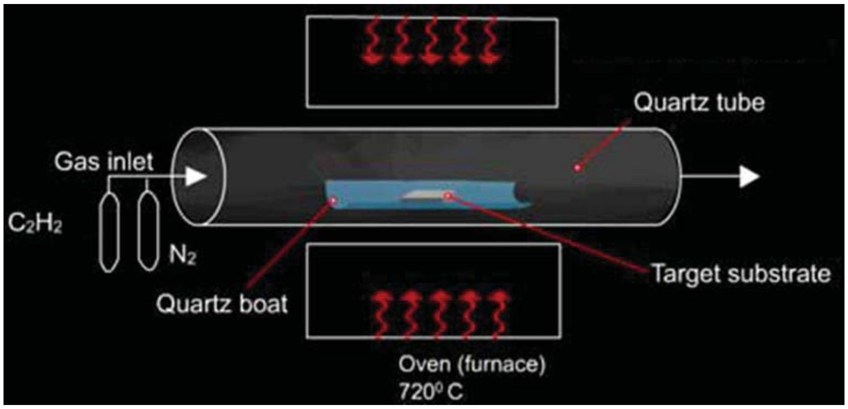

Figure 1.11 Schematic of CVD chamber [46].

The precursor gases are introduced into the evacuated reaction chamber where the substrate for deposition is placed and heated to the desired temperature. The supplied gases reacts on the surface of the substrate and deposition of the material occurs. The gas phase by-products produced from the reaction are removed from the other end of the reaction chamber. Several factors affecting the quality of thin film on the substrate are: purity and concentration of feeding gas, substrate temperature and vacuum pressure. CVD has a major advantage of producing well controlled and uniform film, with good side wall coverage [46].

A different CVD technique using plasma to deposit thin layer is called Plasma Enhanced CVD (PECVD). A high electric voltage is applied in the chamber where gases are passed through, forming plasma. This allows reaction to occur at low temperatures, a great benefit during chip manufacturing especially to transistors made with dopants which will otherwise get removed during substrate heating.

1.2.4.2 Physical Vapor Deposition (PVD, Sputtering)

Physical vapor deposition (sputtering) involves bombardment of a target material (solid material) that are to be deposited on a substrate with highly energetic Argon (Ar) ions. The choice of gas is Ar because it is an inert gas which will not react with the target nor the substrate. Sputtering takes place in the plasma environment produced by applying high electric voltage in the chamber under high vacuum condition of ~ 10^{-6} torr. The target can be kept at relatively low temperature (opposite of evaporation process), making this one of the most flexible deposition technique, especially useful for alloys.

The working principle of sputtering can be explained by Figure 1.12. A substrate is located opposite of a target (material to be deposited) inside a vacuum chamber. A feed gas (Ar) is passed inside the chamber at low pressure, where it is ionized. The positive Ar ions will move towards the negative target material, hitting the target with high force. Once the ions hit the target, a few atoms gets knocked off and fall on the substrate. The sputtering yield depends on the speed of argon ions, the angle of impact and the bond strength of the target [47]. Sometimes a substrate is rotated slowly to ensure uniform deposition.

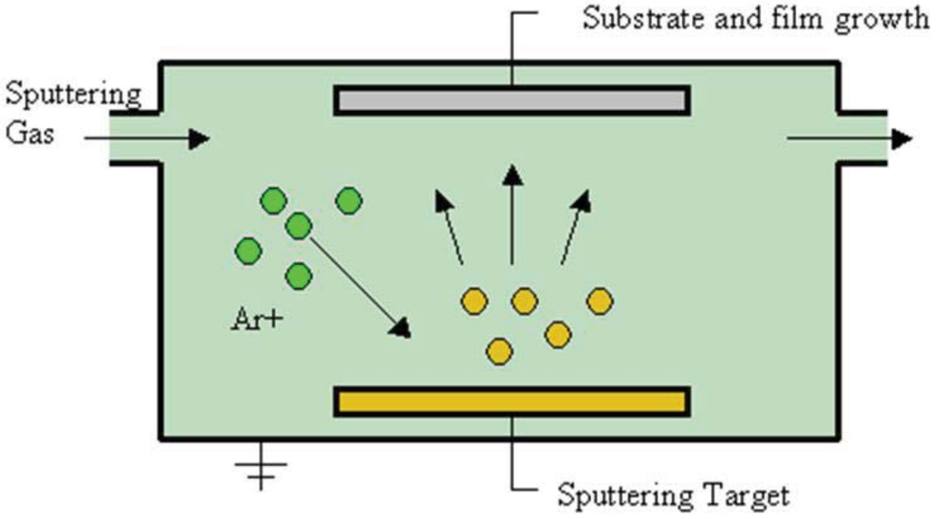

Figure 1.12 Schematic of sputtering process [47].

Magnetron sputtering utilizes magnets to trap electrons produced in the plasma, so as to prevent substrate bombardment, substrate overheating or from being damaged. They also have a capability of inducing high energy states using direct current (DC), alternating current (AC) and radio frequency (RF) magnetron sources. A dual magnetron sputtering system is shown in Figure 1.13. Metals are easy to deposit because they are conductors, however insulators such as silicon dioxide or silicon nitride can also be deposited by PVD process. Since they are insulators, accumulated charge stays on the surface, and positive Ar ions cannot effectively sputter the target.

An RF sputtering (using RF AC voltage) is used that supplies electrons to the surface of the insulator and deposition is possible.

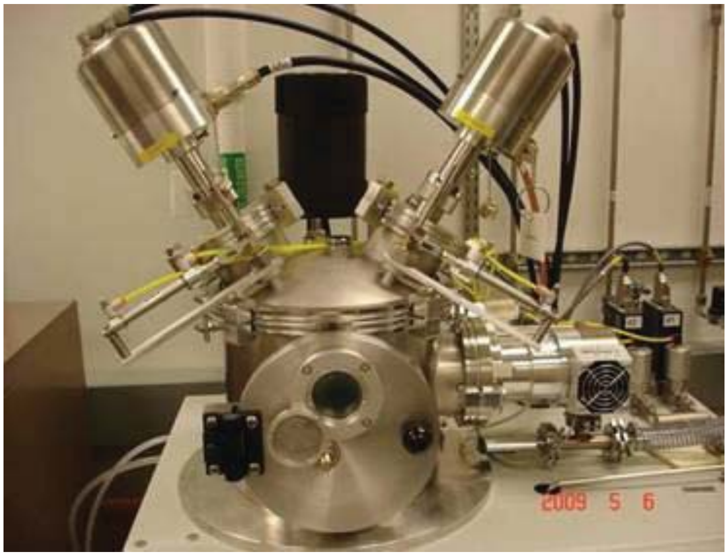

Figure 1.13 Dual magnetron sputtering system.

1.2.5 Contact Angle

Contact angle is simply the angle liquid makes with the solid surface. It is defined as an angle between the tangent of the liquid droplet to the flat, smooth solid surface where the droplet is placed, Figure 1.14. Contact angle measurement is widely used that can provide information on wettability and adhesiveness properties of a surface. The contact angle of a small, free standing droplet is a function of solid surface free energy, defined by the Young-Dupre equation [48].

$$\gamma_{lv} \cos\theta = \gamma_{sv} - \gamma_{sl}$$

where θ = contact angle, γ = interfacial free energy, lv = liquid-vapor, sl = solid-liquid, and sv = solid-vapor interfaces.

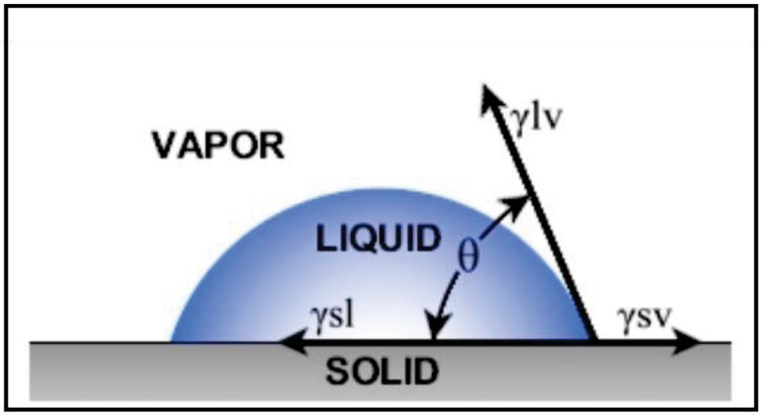

Figure 1.14 Schematic of contact angle.

The angle between a droplet and the solid surface is a function of cohesive (in liquid) and adhesive (between solid and liquid) attractions. The contact angle increases when the interaction between the solid and the liquid decreases. On the other hand, as the interaction between the solid and the liquid increases, the liquid spreads out and the value of θ decreases. Water is typically used to measure contact angle that enables to provide hydrophilicity or hydrophobicity nature of the surface.

1.2.6 Barrel Etcher (Plasma Cleaner)

A plasma is basically a partially ionized gas that contains equal numbers of unbound positive (ions) and negative (electrons) charges, and some excited and unexcited unionized neutral molecules. A typical plasma reactor consists of two parallel plate electrodes placed in a vacuum chamber. An operating gas is filled at low pressure. When subjected to RF voltage between the electrodes, a discharge current flows forming a plasma. Plasma emits a characteristic glow due to the electronically excited species in the plasma that is characteristic of the discharge gas composition [49]. For example, nitrogen gives a pink color due to the excited nitrogen molecules.

There are many types of reactors available depending on the need and function. They are all basically glow discharge systems but vary in terms of excitation frequency (5 KHz – 5 GHz), operating pressure (1 mbar – atmospheric pressure) and electrode arrangement [49]. Barrel etcher, a type of plasma reactor is mostly used for removing organic contamination and/or modify physical and chemical properties of the surface. A barrel etcher (plasma cleaner) is shown in Figure 1.15. A sample is placed in the reaction chamber. An operating gas at low flow rates (~ 5 - 10 SCFH) and low pressure (~200 - 600 mtorr) is subjected to RF voltage at 8 – 12 MHz, creating plasma at near ambient temperature, within the chamber.

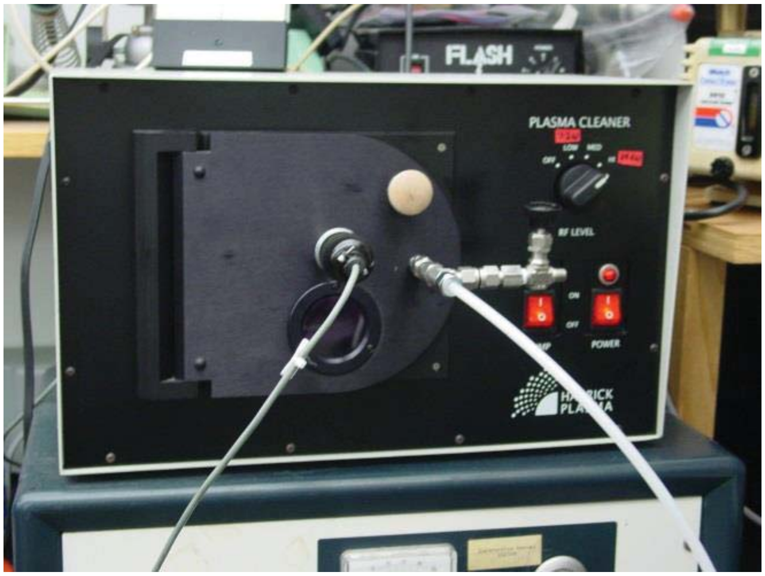

Figure 1.15 Barrel etcher (plasma cleaner).

The type of interaction of the plasma with the sample surface is dependent on parameters such as intensity and frequency of RF power, type of gas used, pressure, flow rate, type of sample and the exposure time.

Several excitation processes can occur in the plasma. In the ionization process, an electron is ejected out from an atom. An example of the ionization of Ar atom is expressed by:

$Ar \rightarrow Ar^+ + e$

In the excitation process, a transfer of energy takes place which allows electron to move to a higher energy level within the atom forming excited state atom.

$e + Ar \rightarrow Ar^* + e$

Furthermore, dissociation of a molecule can occur as well. Oxygen molecule, for example can be dissociated into two reactive oxygen atoms. However, dissociation may or may not happen with ionization.

$e + O_2 \rightarrow e + O + O$

$e + CF_4 \rightarrow e + CF_3 + F$ (Dissociation)

$e + CF_4 \rightarrow 2e + CF_3^+ + F$ (Dissociative Ionization)

The reactive species like oxygen atom tend to oxidize organic molecules more readily than oxygen molecules even at room temperature (plasma temperature) and is more controllable.

1.3 References

1. Bardeen, J.; Brattain, W. H. *Phys. Rev.* **1948**, 71, 230.
2. Online source: http://www.icknowledge.com/history/1950s.html. (retrieved on 03/07/16).
3. Online source: http://nptel.ac.in/courses/103106075/8. (retrieved on 03/07/16).
4. Online source: http://www.ti.com/corp/graphics/press/image/on_line/co1034.jpg. (retrieved on 03/07/16).
5. Moore, G. "*Cramming More Components Onto Integrated Circuits*," *Electronics*. **1965**, 38 8.

6. Online source: http://www.intel.com. (retrieved on 03/07/16).
7. Weng, C. MEMS and Nanotechnology; Springer: NY, **2011**, 4.
8. Online source: http://www.intel.com/research/silicon/mooreslaw.htm. (retrieved on 03/07/16).
9. Jeng, S.; Havemann, R.; Chang, M. ‘Advanced Metallization and Interconnect Systems for ULSI Applications, *Mat. Res. Soc. Proc*. **1996**, 337, 25.
10. Baklanov, M.; Green, M.; Maex, K. *Dielectric Films*; Wiley: Chichester, **2007**.
11. Sekar, D.; Tõkei, Z.; McGahay, V. On-Chip Interconnect Costs Spawn Research, *EE Times*. **2014**.
12. Chen, K. W.; Wang, Y. L.; Chang, L.; Chang, S. C.; Li, F. Y.; Lin, S. H. *Electrochem. Solid-St. Lett*. **2004**, 7, G238.
13. Lee, W. W.; Russell, S. “*Integration Challenges of Low k Materials*,” *Future Fab Intl*. **2002**, 8.
14. Jindal, A.; Babu, S. V. *J. Electrochem. Soc*. **2004**, 151, G709.
15. Baklanov, M. R.; Ho, P. S.; Zschech, E. *Advanced Interconnects for ULSI Technology*; Wiley: Chichester, **2012**.
16. Darnon, M.; Chevolleau, T.; Joubert, O.; Torres, J.; Undulation of sub-100 nm porous dielectric structures, *Appl. Phys. Lett*. **2007**, 91, 194103.
17. Han, Q.; White, B.; Berry, I. L.; Waldfried, C.; Escorcia, O. *Solid State Phenomena*. **2005**, 103, 341.
18. Shikida, M.; Sato, K.; Tokoro, K.; Uchikawa, D. *J. Micromech. Microeng*. **2000**, 10, 522.
19. Kohler, M. *Etching in Microsystem Technology*; John Wiley & Sons: Chichester, **1999**.

20. Somashekhar, A.; Ying, H.; Smith, P. B.; Aldrich, D. B.; Nemanich, R. J. *J. Electrochem. Soc.*, **1999**, 146, 2318.
21. Oehrlein, G. S.; Lee, Y. H. *J. Vac. Sci. Technol. A.* **1987**, 4, 1585.
22. Verhaverbeke, S.; Kuppurao, S.; Beaudry, C.; Truman, J. Semiconductor Intl. **2002**, 25, 91.
23. Tatsumi, T. *Appl. Surf. Sci*. **2007**, 253, 6716.
24. Maex, K.; Baklanov, M. R.; Shamiryan, D.; Iacopi, F.; Brongersma, S. H.; Yanovitskaya, Z. S. *J. Appl. Phys.* **2003**, 93, 8793.
25. National Technology Roadmap for Semiconductors, Semiconductor Industry Association **2004**.
26. Hoofman, R.; Verheijden, G.; Michelon, J.; Baklanov, M. R. *Microelectron. Eng*. **2005**, 80, 337-344.
27. Hoofman, R.; Verheijden, G.; Michelon, J.; Arnal, V.; Michaelson, L. Proceedings of the Int. Interconnect Tech. Conf. **2005**, 85-97.
28. Havemann, R. H.; Hutchby, J. A. *Proc. IEEE*. **2001**, 586.
29. Baklanov, M. R.; Travaly, Y.; Le, Q. T.; Shamiryan, D.; Vanhaelemeersch, S. Silicon Nitride, Silicon Dioxide, Thin Insulating Films and Other Emerging Dielectrics YIII. *ECS*. **2005**, PV 2005-01, 179-198.
30. Le, Q. T.; Baklanov, M. R.; Kesters, E.; Azioune, A.; Struyf, H.; Boullart, W.; Pireaux, -J. J.; Vanhaelemeersch, S. *Electrochem. Solid State Lett*. **2005**, 8 (7), F21-F24.
31. Iijima, T.; Lin, Q.; Chen, S.; Labelle, C.; Fuller, N.; Ponoth, S.; Cohen, S.; Lloyd, J.; Dunn, D.; Muzzy, C.; Gill, J.; Nitta, S.; Spooner, T.; Nye, H. Proceedings of IEEE IITC 2006. **2006**, 21.

32. Bao, J.; Shi, H.; Liu, J.; Huang, H.; Ho, P. S.; Goodner, M. D.; Moinpour, M.; Kloster, M. G.; McSwiney, L. M. *J. Vac. Sci. Technol. A.* **2010**, 28 (2).
33. Shi, H.; Huang, H.; Im, J.; Ho, P. S.; Zhou, Y.; Pender, J. T.; Armacost, M.; Kyser, D. *Proc. in IEEE International Interconnect Technology*. **2010**, 8.
34. Gates, S. M.; Grill, A.; Dimitrakopoulos, C.; Patel, V.; Chen, S. T.; Spooner, T.; Ryan, E. T.; Cohen, S. A.; Simonyi, E.; Liniger, E. *Proc. of Advanced Metallization Conference*. **2009**, 531.
35. Edelstein, D.; Uzoh, C.; Cabral, C. Jr.; DeHaven, P.; Buchwalter, P.; Simon, A.; Cooney, E.; Malhotra, S.; Klaus, D.; Rathode, H.; Agarwala, B.; Nguyen, D. *Proc. of Advanced Metallization Conference*. **2002**, 541.
36. Briggs, D.; Seah, M. P. *Practical Surface Analysis: Auger and X-Ray Photoelectron spectroscopy*; John Wiley & Sons: Chichester, **1996**.
37. Wagner, C. D.; Riggs, W. M.; Davis, L. E.; Moulder, J. F. *Handbook of X-ray Photoelectron Spectroscopy*; Physical Electronics: Eden Prarie, **1995**.
38. Griffiths, P. R.; de Haseth, J. A. *Fourier Transform Infrared Spectrometry*; Wiley: Hobeken, **2007**.
39. Smith, B. C. *Fundamentals of Fourier transform infrared spectroscopy*; CRC Press: New York, **1996**.
40. Harrick, N. J. *Internal Reflection Spectroscopy*; Interscience Publishers: NY, **1967**.
41. Mirabella, M. F.; Harrick, N. J. *Internal Reflection Spectroscopy: Review and Supplement*; Harrick Scientific Corporation: NY, **1985**.
42. Martin-Gil, J.; Palacious-Leblé, G.; Ramos, P. M.; Martin-Gil, F. J. *Journal of Interdisciplinary Celtics Studies*. **2007**, 5, 66.

43. Online source: http://www.nptel.ac.in/courses/103106075/39. (retrieved on 03/07/16)
44. Skoog, D. A.; Leary, J. J. *Principles of Instrumental Analysis*; Saunders, **1992**.
45. Goldstein, J. I.; Joy, D. C.; Lifshin, E. *Scanning Electron Microscopy and x-ray microanalysis*; Plenum Press: NY, **1992**.
46. Suntola, T. *Handbook of Crystal Growth*, Elsevier Science. Amsterdam, **1994**.
47. Behrisch, R. *Sputtering by Particle bombardment*; Springer: Berlin, **1981**.
48. Young, T.; Peacock, G. *Miscellaneous Works*; Murray: London, **1855**, 418, 1.
49. Online source: http://www.quorumtech.com. (retrieved on 03/07/16).

CHAPTER 2

DEVELOPMENT AND OPTIMIZATION OF NOVEL MIR-IR METROLOGY FOR POROUS LOW-*K* DIELECTRICS AND ITS APPLICATIONS[†]

2.1 Introduction

Over the past decade or so, device and integrated circuit (IC) technology has evolved rapidly with shrinking dimensions toward the use of more sophisticated structures such as 3-D structures fabricated using new materials and processes. The reduction in feature size drives the timeline for metrology needs to provide solutions for new materials, process, and structures. Since some of the feature size approaches near atomic scale dimension, precise control of the processes throughout the development cycle is a must. One of the critical areas in the IC fabrication process that requires attention is the implementation of fragile porous low-*k* dielectrics in advanced copper interconnect design. Integration of porous ultra low-*k* (ULK) interlayer dielectrics (ILD) into Cu interconnect nanostructure will continue to pose major technological challenges in back-end-of-line (BEOL) fabrication beyond 32 nm. As stated in the 2009 ITRS Roadmap, “Etching and ashing processes are among the worst for inducing damage to low-*k* materials, affecting not only defectivity, but also electrical reliability” [1]. ULK materials are more easily physically damaged because the increased porosity of carbon doped silicon oxide (CDO) inherently reduces the robustness as compared to the traditional inorganic glass dielectrics. Moreover, the higher carbon content of the ULK CDO makes it more chemically similar to organic photoresist and thus more prone to suffer collateral plasma-induced damages during RIE and photoresist stripping.

[†] This chapter is presented in its entirety from S. Rimal, N. Ross, K. S. M. Pillai, K. J. Singh, and O. Chyan, “Characterization of Post Etch Residues on Patterned Porous Low-k Dielectric Using Multiple Internal Reflection Infrared Spectroscopy,” *ECS Trans.*, **2011**, 41, 315 with permission from The Electrochemical Society.

Furthermore, stricter critical dimension (CD) requirements at sub-10 nm technology node demands low-*k* dielectric nanostructure to be fabricated with no/ very minimum (< 1 nm) dielectric damages. The stringent requirement makes qualitative/ quantitative characterization pose further challenges.

Figure 2.1 highlights some of the technical challenges in the trench patterning processes involved in patterning porous low-*k* ILD film stacks. To begin, the intense fluorine chemistry based on ion bombardment and reactive radicals also referred as reactive ion etching (i.e. RIE using C_xF_y plasmas) used to create nanometer sized high aspect ratio (HAR) trench patterns often leaves substantial polymer residues that require subsequent dry ash or wet cleans. Both the RIE and post-RIE cleaning processes could also result in ULK ILD damage resulting in enhanced moisture absorption. Consequently, the successful patterning of next-generation ULK/Cu interconnects through various non-damaging etch, ash and cleans processes represents an increasingly challenging task for the semiconductor industry.

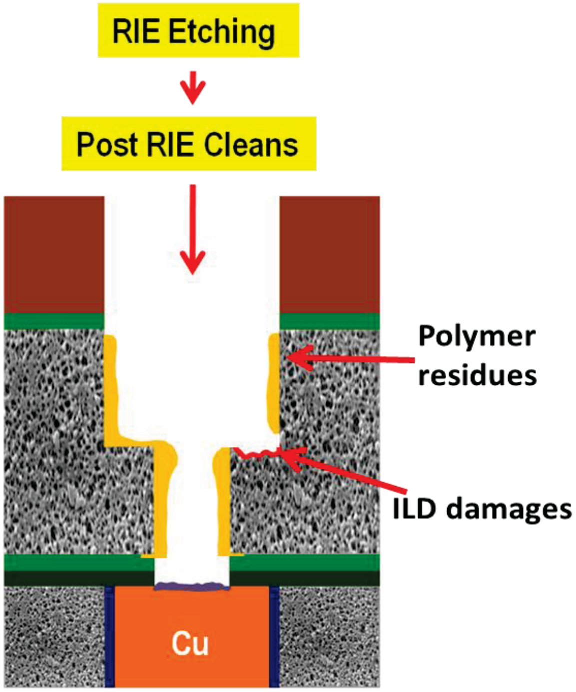

Figure 2.1 Technical challenges in the porous low-*k* trench patterning processes.

Given these difficulties, a sensitive metrology to evaluate the condition of ULK material at every step of the fabrication process would be invaluable to the systematic development of improved plasma etching, restoration and cleaning processes. However, most, if not all, currently used characterization techniques such as SEM, TEM, XPS, SIMS, Ellipsometry etc. illustrated in Figure 2.2 lack the required "specificity or sensitivity" to be useful as a reliable process monitoring tool. For example, XPS and TOF-SIMS can only determine "elemental composition" changes in ULK ILD and in the residual polymers generated. However, these methods do not yield the bonding and structural information needed to accurately access ULK ILD integrity, cross linking densities of etch residues and subsequent cleanability. These techniques are based on ion beams and are destructive to fragile dielectrics material. The morphological characteristics (feature shapes, uniformity etc.) can be assessed by SEM or TEM, however are destructive and time consuming (especially TEM). Furthermore, these characterization techniques are top down analyses techniques and hence difficult to access information from the deep trench bottom and sidewalls. Alternatively, infrared spectroscopy (IR) provides "bonds fraction" data for the ULK

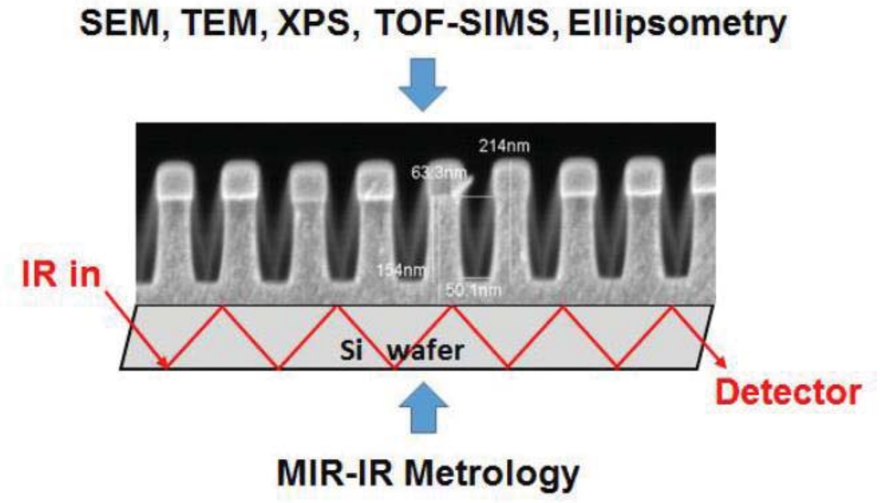

Figure 2.2 Characterization tools to assist low-*k* dielectric nanostructure fabrication.

ILD and is very useful in revealing plasma-induced ILD damage by monitoring the decreasing IR absorbance ratio of cage vs. network Si-O-Si bonds. However, state of the art transmission as well as external ATR-IR spectroscopy lacks the “sensitivity” to be useful in monitoring the progression of etching/cleaning processes, especially for patterned wafers. From the chemical bonding view point, the success on fabricating next generation Cu interconnect is achieved by the ability to control chemical bond breaking and bond formation in highly selective time sequences within restricted nanometer dimension. As such, there is a pressing need for a reliable metrology to guide BEP process development and integration efforts for shrinking technology nodes. In this work, we report achievements towards the development and optimization of novel Multiple Internal Reflection Infrared Spectroscopy (MIR-IR) and its potential application in the BEP process development.

2.2 General principle of MIR-IR spectroscopy

The working principle of MIR-IR can be understood as the advancement of the established spectroscopic technique known as ATR-IR, first described in detail by Harrick [2]. The detail description of the working principle of ATR-IR theory is described in Chapter 1. The phenomenon of internal reflection occurs when two mediums in contact have different refractive indices, optically denser medium with higher index than the optically rarer medium. The incident IR radiation in the denser medium (refractive index n_1) undergoes total internal reflection at the interface with respect to the rarer medium (refractive index n_2), when the angle of incidence Θ exceeds the critical angle Θ_c, which is defined by:

$$\Theta_c = \sin^{-1} (n_2/n_1)$$

By the interaction of the incident and reflected light, the exponentially decaying standing evanescent field is formed, which penetrates the rarer medium (air or sample) with distance (x) perpendicular to the sample surface as depicted in Figure 2.3. The penetration depth (d_p) of the evanescent wave depends on the wavelength of the incident light (λ), the angle of incidence (θ) and the refractive indices of the waveguide (n_1) and the sample (n_2):

$$d_p = \lambda/\{2\pi n_1[\sin^2\theta - (n_2/n_1)^2]^{1/2}\}$$

Whereas the amplitude E(x) of the evanescent field decreases exponentially with the distance x to the interface following:

$$E(x) = E_0 \, e^{-x/d_p}$$

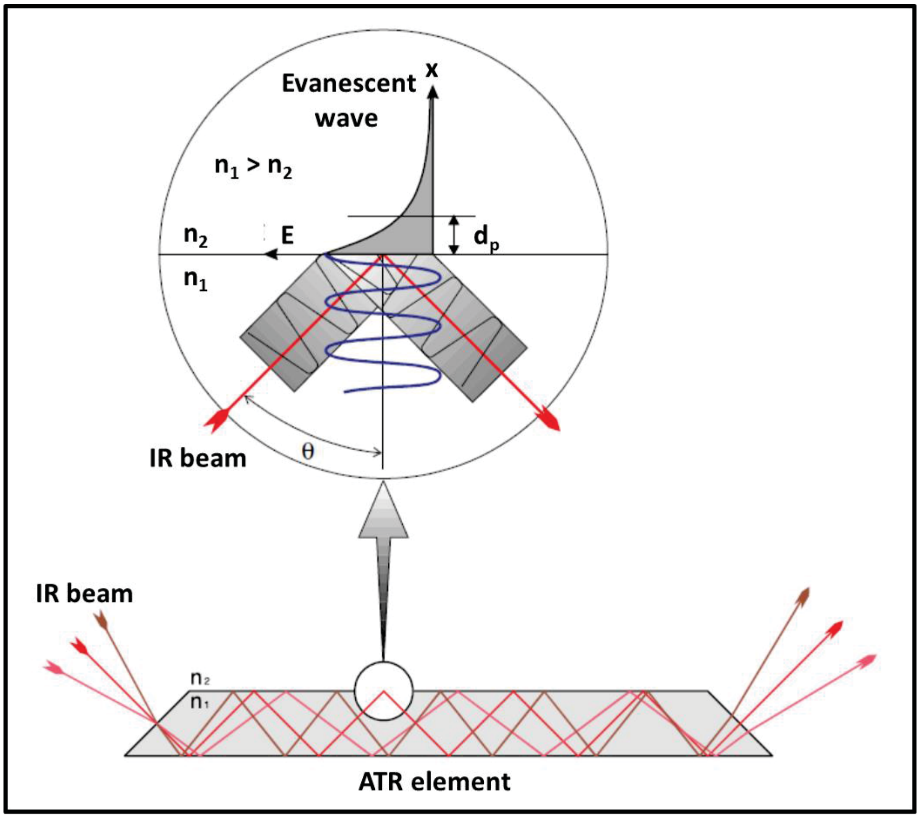

Figure 2.3 Scheme of ATR principle showing propagation of IR radiation through an ATR element [3].

The higher the penetration depth, the higher is the absorbance signal. By interaction of the evanescent field with the sample medium leads to intrinsically enhance sensitivity for each internal reflection.

Both MIR-IR and External ATR-IR spectroscopy follows the same common ATR theory, however the geometry of measurement for two different IR techniques is different, Figure 2.4. External ATR-IR is a face contact angle method, where a sample surface is squeezed against an ATR waveguide. This cause to form air gaps between sample and the waveguide producing non-reproducible results and weaker absorbance signal. In addition, squeezing sample surface with applied mechanical pressure can easily cause sample damage, especially to fragile dielectric patterned features. The technique is also hampered by low sensitivity because of the mix max of evanescent wave interaction with the sample. On the other hand, MIR-IR overcomes the sensitivity issue encountered with the ATR-IR technique, because the waveguide itself is directly prepared from the patterned wafer. In doing so, it does not have sample-contact problem and no issue of sample damage. More importantly, the waveguide itself acts as a light propagating medium, hence

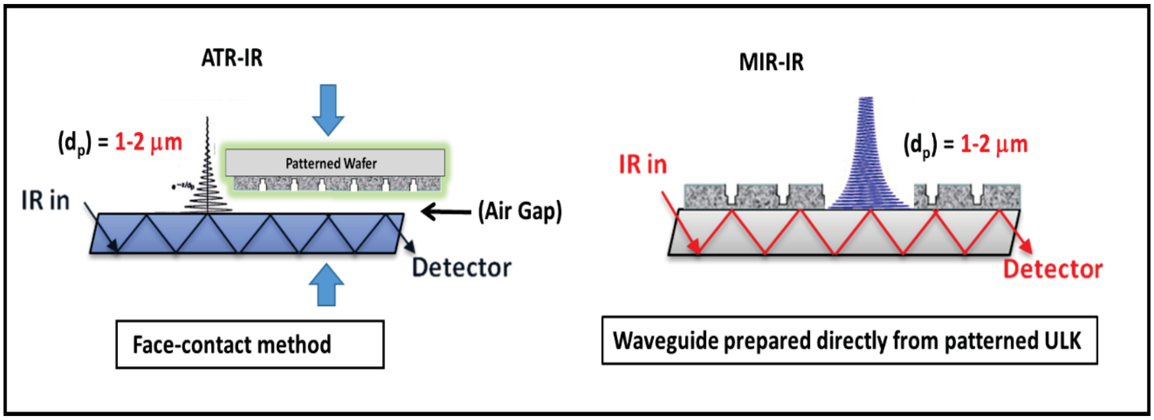

Figure 2.4 Schematics of ATR-IR and MIR-IR spectroscopy geometries.

there is a maximum evanescent wave interacting with the probing surface, and result in superior sensitivity. Figure 2.5 shows the FT-IR spectra of a thin photoresist (PR) film from two different attenuated total reflection (ATR) measuring configurations - multiple internal reflection (MIR-IR) FT-IR in Figure 2.5 (a), and external ATR FT-IR in Figure 2.5 (b). The presence of thin PR film by face-contact external ATR technique is not evident mainly because of the existence of air gap between PR thin film and the internal reflection element (IRE) used in this geometry. The air gap can diminish the interaction of surface evanescent wave with the PR film producing weak absorbance signal.

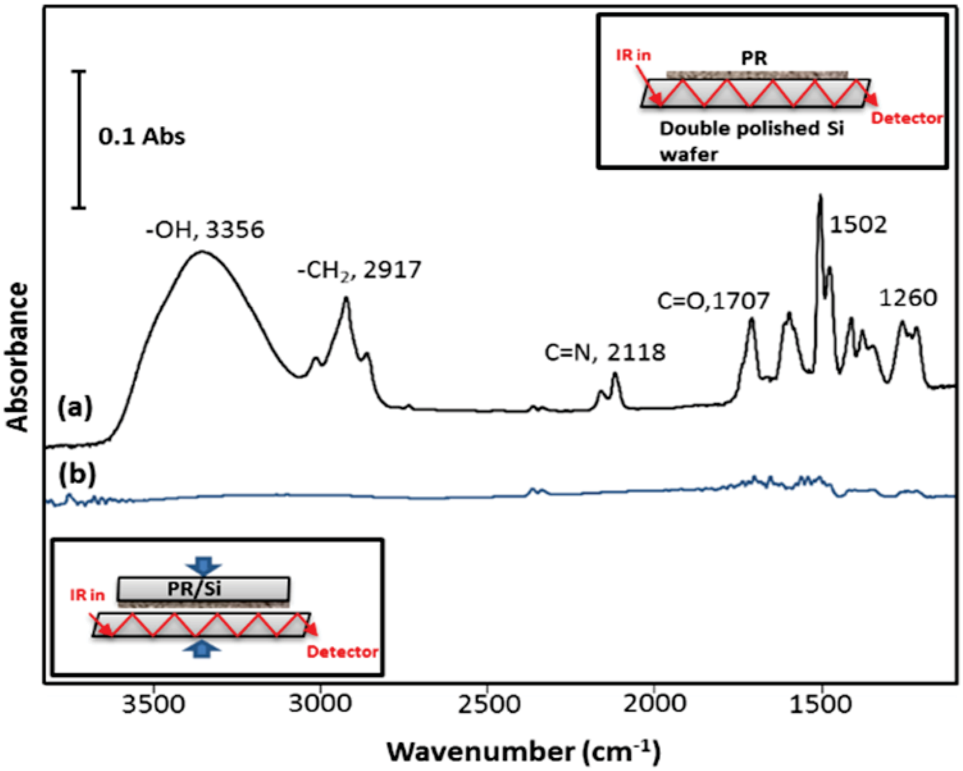

Figure 2.5 FT-IR spectra of thin Photoresist film measured by (a) MIR-IR (image, inset top right) and (b) Face-contact External ATR (image, inset bottom left).

In contrast, MIR-IR utilizes the silicon wafer substrate itself as a waveguide (fabrication process described in experimental section) which can be analyzed directly with no further additional IRE waveguide necessary. The silicon waveguide prepared directly from patterned wafer enable multiple total internal reflections, which greatly enhances IR measuring sensitivity. As shown in Figure 2.5 (a), MIR-IR is capable of detecting thin photoresist coating on a Si wafer with much higher intensity and superior spectral resolution than is possible with external ATR FT-IR. All intrinsic chemical bonding features of PR are identified as absorption peaks at ~ 3360 cm^{-1} (O-H stretch), 2917 cm^{-1} (CH_2), 2218 cm^{-1} (C=N, originated from a diazoquinone photosensitizer), 1707 cm^{-1} (C=O) and ~ 1200 – 1600 cm^{-1} (fingerprint region).

2.3 Experimental

2.3.1 Fabrication of waveguide (ATR crystal)

A fabrication technique to prepare Si waveguide directly from unpatterned as well as patterned ULK wafers have been developed. The crystal dimension of 6 x 1 x 0.7 cm coupon into an ATR waveguide is polished using multiprep polishing machine at a 45° bevel angle. To achieve fine and smooth bevel angle we start with coarse polishing using Si-carbide of 320 µm grit for bulk removal followed by fine polishing using several diamond lapping polishing pads and submicron size polycrystalline diamond suspension. The polishing continues until a very smooth bevel surface (verified by optical microscope) is achieved. Organic solvent and HF solution is used to clean the residues after polishing. Figure 2.6 shows the schematic of Si based ATR prepared directly from patterned wafer. IR beam is incident normal to the surface of the ATR element, which has a bevel angel of 45 degrees. Each internal reflection sets up a standing wave pattern (evanescent wave) due to the interference of the incoming and outgoing waves, which is confined

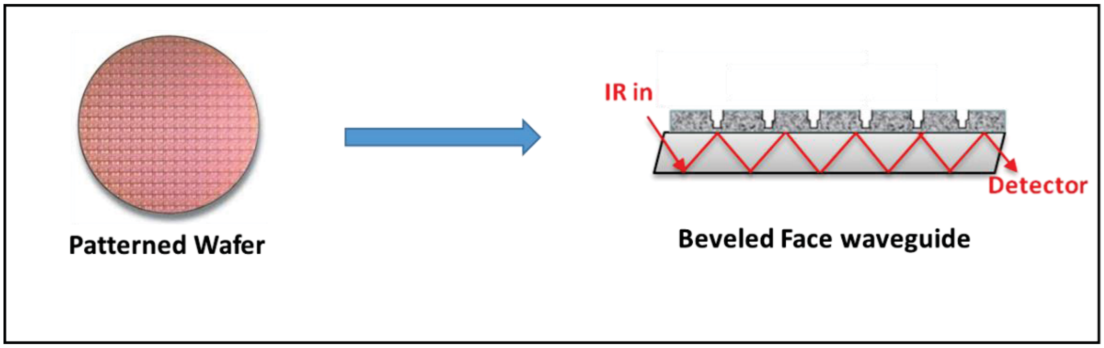

Figure 2.6 Silicon wafer based waveguide for MIR-IR spectroscopy.

to sub-micron space above the silicon surface. The number of internal reflections can be obtained using the following equation:

$$N = l/t.\ \mathrm{Cot}\Theta$$

Where N = number of reflections, l = length and t = thickness of the ATR element. These parameters can be manipulated to maximize the number of internal reflections which will further increase the sensitivity of the system. The number of internal reflections from 6 x 1 cm waveguide comes out to be about 90.

2.3.2 Prepatory cleaning of Si substrate

The treatment and preparation of Si surface is a critical process in IC fabrication to avoid device malfunctioning caused by trace level of contaminants [4-6]. Particles, metallic ions, organic residues, chemical and biological contaminations are the common. In order to remove contribution from these contamination, a clean bare Si is obtained after Standard Clean 1 solution (SC1) required for MIR-IR analysis. SC1 solution is a mixture of ammonium hydroxide, hydrogen peroxide and UPW in the ratio 1:1:5 respectively. The treatment is typically applied for organics removal, surface impurities and particulates. The bare Si crystal pre cleaned with organic solvent and UPW is immersed in SC1 solution at 80 °C for ~10 minutes. The surface is oxidized by hydrogen peroxide and solvation by ammonium hydroxide aids in organics removal process. The treatment also continuously forms and dissolute hydrous oxide film on the surface, which helps to remove the particulates. SC1 cleaning treatment often leaves the surface with chemical oxide of few angstroms thickness which is rinsed with ample amount of UPW and etched with HF acid solution (~0.5%). The SC1 cleaned bare Si waveguide was used as a reference background in the MIR-IR analysis.

2.3.3 Characterization

All MIR-IR spectra were collected on newly released Nicolet is50 FT-IR spectrometer. Figure 2.7 below shows the new instrument and the detector's specific detectivity. The new instrument comes with novel patented SiN IR source with 20% brighter radiation compared to the regular SiC IR source, to provide higher throughput. In addition, MCT A, a quantum detector with higher sensitivity given in terms of its specific detectivity (D^*), Figure 2.7 (right) in the mid-IR

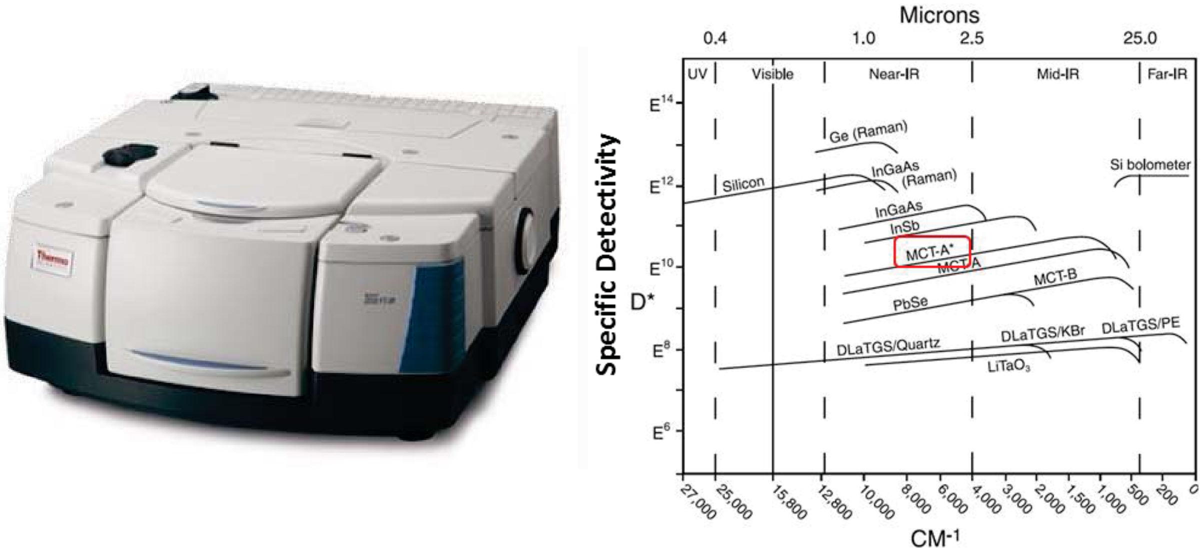

Figure 2.7 New Nicolet is50 FT-IR spectrometer (left) and plots of D^* against wavelength for a number of detectors (right).

region was used. With culmination of all the features, it provided higher signal-to-noise ratio (SNR), better stability and higher optical throughput which leads to increase sensitivity of the instrument.

To validate improved S/N ratio in is50 spectrometer eqipped with MCT-A detector, 100% T measurement was performed, Figure 2.8 and shows better S/N. In Figure 2.9, MIR-IR spectra of a 190 nm CDO was obtained using a weaker thermal DLaTGS detector, and compared to MIR-IR spectrum obtained from MCT-A detector. The spectra was comparable, and confirmed higher optical throughput obtained from 20% brighter SiN source used.

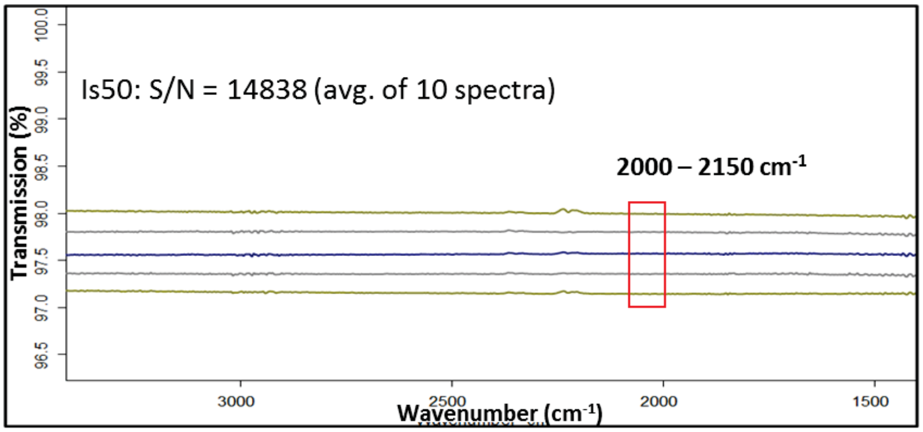

Figure 2.8 S/N ratio obtained from is50 FT-IR.

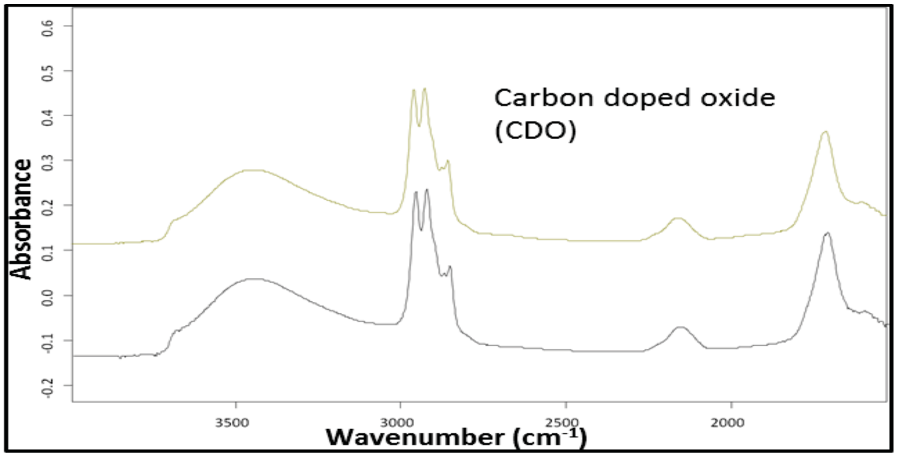

Figure 2.9 MIR-IR obtained from thermal DLaTGS detector.

The ATR measurements were performed using vertical ATR optical accessory obtained from Pike Technologies. The silicon ATR crystals were handled only by pre-cleaned Teflon based utensils to avoid organic contaminations through contact transfer. The spectrometer is constantly purged with low organics high purity nitrogen gas. The resultant IR spectra were collected at 4 cm^{-1} resolution and are the sum of 100 individual spectra.

2.3.4 Photoresist coating and ashing

Before the photoresist coating, the MIR-IR spectra of Si ATR optical elements were measured as the reference background. The photoresist (Clarion) was spin-coated on pre-cleaned Si or CDO/Si ATR optical elements. The CDO was deposited on Si wafers using standard CVD deposition method. Following a 20 minutes air dry period, the photoresist coated Si ATR element was etched in O_2 plasma for pre-set time using a Harrick Plasma Etcher (100 mtorr, 30 watts). The extent of photoresist ashing was evaluated by MIR-IR following the O_2 plasma etching.

2.4 Results and Discussion

2.4.1 Surface transformation on Si (100) induced by trace metal ions probed by MIR-IR

MIR-IR is capable of detecting a sub-monolayer surface transformation on a silicon surface. Figure 2.10 shows time-dependent MIR-IR spectra of a Si (100) wafer immersed in HF solution contaminated by trace levels of Cu^{2+} ions. The remarkable detection capacity of MIR-IR (down to 0.0001 absorbance) enables characterization of sub-monolayer hydrogen termination on Si wafer surface in fine details. As shown in Figure 2.10, the IR absorption peak of silicon di-hydrides ($Si\text{-}H_2$) is dominant for Si (100) surfaces as expected. However, surface imperfections

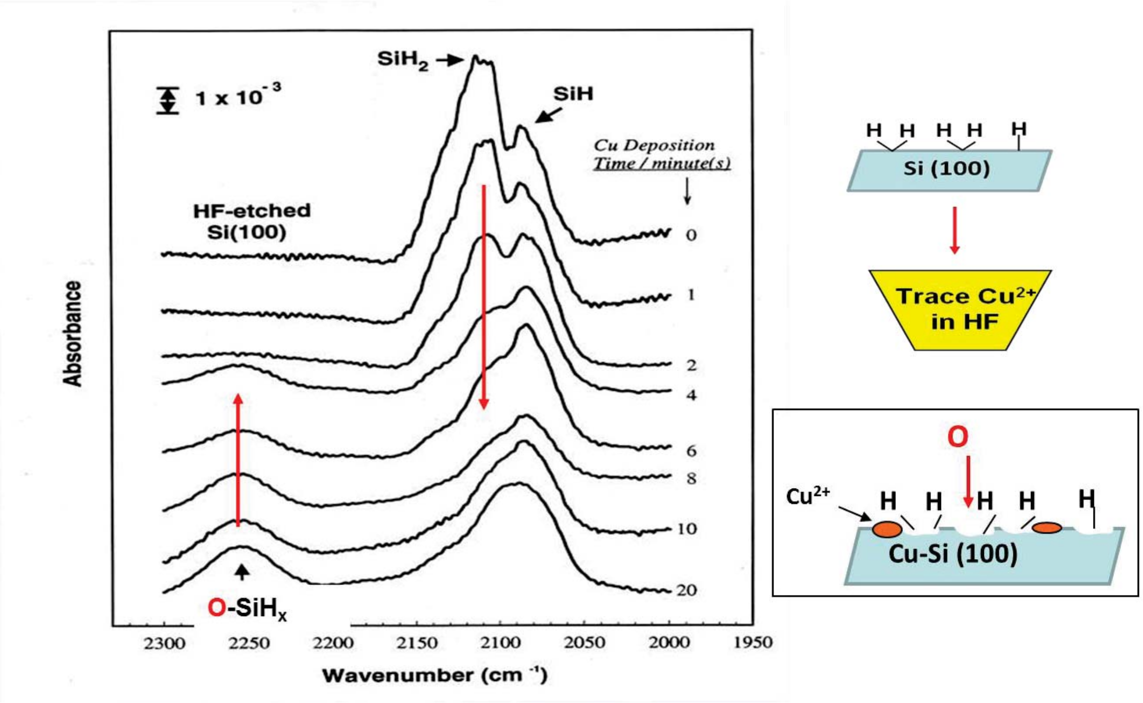

Figure 2.10 Trace metal ions induced silicon oxidation probed by MIR-IR [7].

from Si (100) surface produce some Si (111) facets that account for some silicon mono-hydrides (Si-H) observed at the lower wave number. MIR-IR clearly reveals that trace Cu^{2+} contamination results in a preferential oxidation on surface SiH_2 chemical bonding. Time-dependent MIR-IR spectra helps to resolve the surface chemical bonding transformation of SiH_2 to the oxygen back-bonded O-SiH_x state, first step of forming silicon oxide, induced by *ppb* levels of Cu^{2+} ions.

2.4.2 MIR-IR characterization of 18 nm polymer film produced by plasma polymerization

Recently, MIR-IR spectroscopy was applied to characterize an 18 nm polymer film prepared by low-pressure RF pulsed plasma polymerization [8]. As shown in Figure 2.11 (a), MIR-IR spectra allow clear identification of IR-active functional groups in the polymer thin film with fine spectral resolution. Peak assignments for these spectra are as follows: (a) the region from 3600 to 3000 cm^{-1} (N-H and O-H stretching modes); (b) 2970 cm^{-1} (- CH_3 asymmetric stretch); (c) 2930 cm^{-1} (-CH_2 asymmetric stretch, (d) 2866 cm^{-1} (-CH_3 symmetric stretch); (e) 2240 cm^{-1} (-C≡N stretch); (f) 2180 cm^{-1} (-N≡C stretch); (g) 1650 cm^{-1} (amide C=O stretch). In addition, polymer

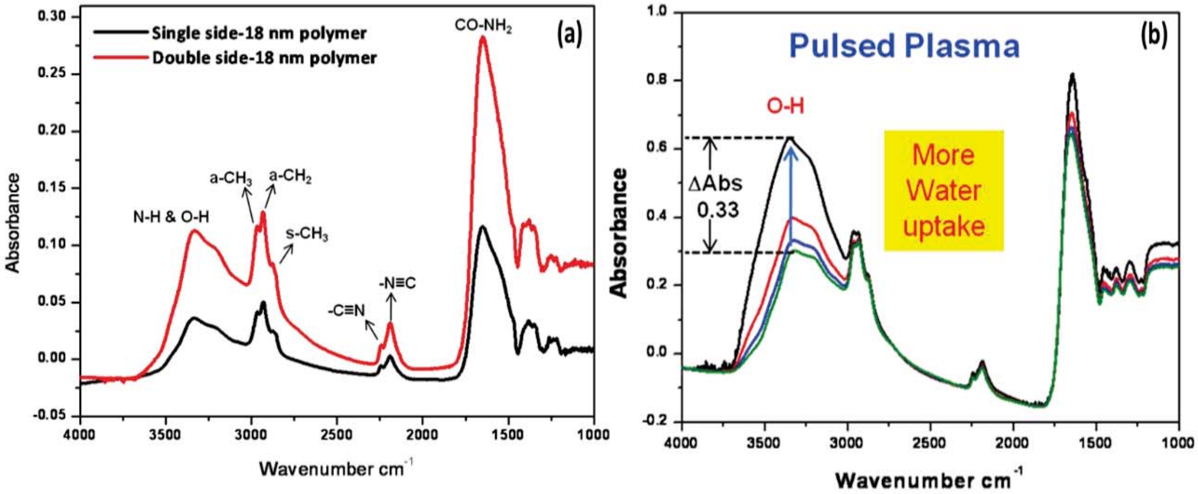

Figure 2.11 MIR-IR spectra of plasma deposited 18 nm polymer films [8].

coating on both sides of the ATR crystal resulted in corresponding increase of IR peak absorbance. MIR-IR also provides direct evidence that the new polymer created under plasma conditions can function as a hydrogel with three-dimensional hydrophilic polymeric structures able to absorb large quantities of water. As shown in Figure 2.11 (b), water uptake efficiency of the hydrogel film can be evaluated based on the absorbance increases at the region from 3600 to 3000 cm^{-1} (O-H stretching mode). With MIR-IR characterization, a hydrogel film made by pulsed plasma was found to adsorb near 100% more water than film prepared by continuous wave plasma.

2.4.3 MIR-IR characterization of photoresist ashing by oxygen plasma

To simulate a BEP plasma etching process, a thin photoresist film was spin coated on a Si wafer and subjected to increasing O_2 plasma ashing. Figure 2.12 shows the IR spectra of photoresist thin film obtained from both MIR-IR and Transmission IR. As seen in Figure 2.12, MIR-IR is capable of detecting the thin photoresist coating on a Si wafer with 60 times higher intensity and superior spectral resolution than is possible with conventional transmission IR. MIR-IR was applied to monitor the complete photoresist ashing process by O_2 plasma. The test clearly demonstrated that MIR-IR is well suited for monitoring time-dependent chemical bonding and structure transformation of organic polymer subjected to plasma etching. It is also interesting to

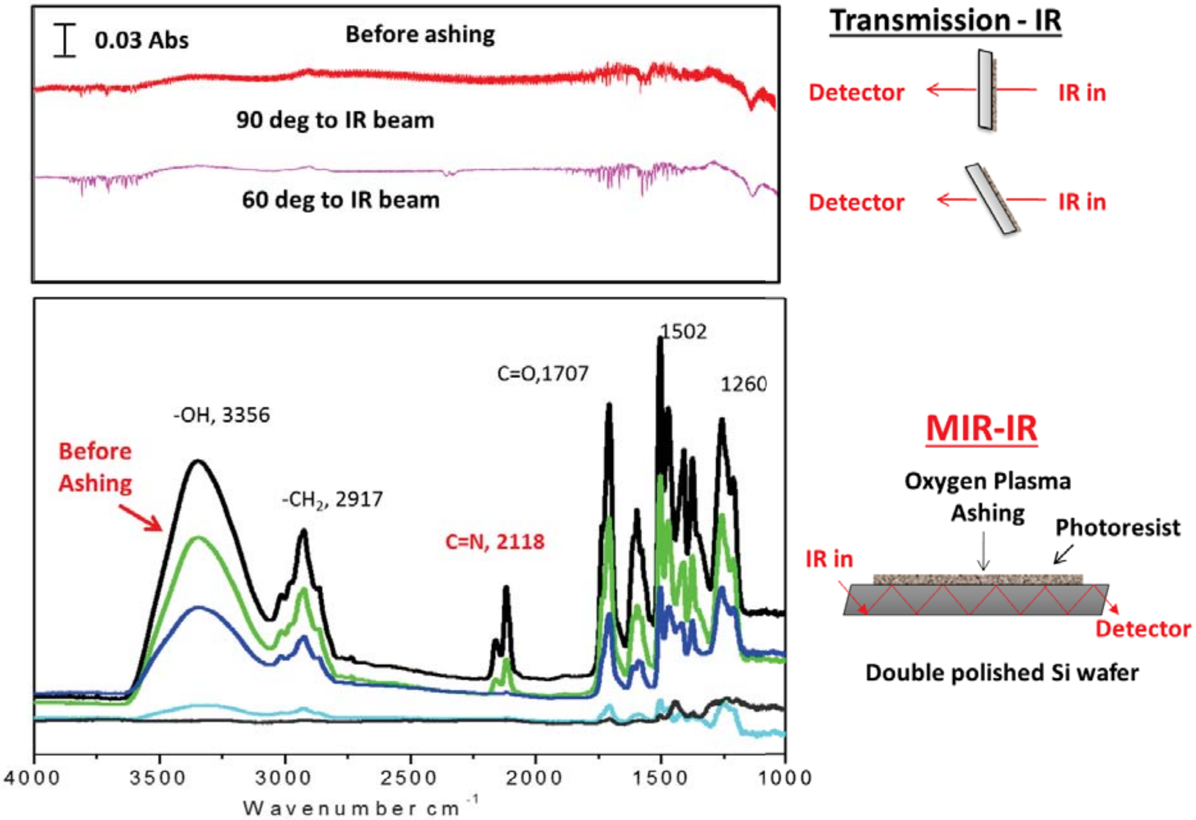

Figure 2.12 MIR-IR monitoring of plasma ashing of photoresist film.

note that C=N bonds (2118 cm^{-1}) in this photoresist coating, Figure 2.12, were found to break more easily, and hence removed earlier under O_2 plasma ashing. The observed enhanced reactivity of C=N bonds corresponds well with the intended chemistry of diazoquinone photo-sensitizer commonly used in photoresists.

2.4.4 MIR-IR characterization of polymer films on carbon doped silicon oxide

To further explore MIR-IR as a potential metrology tool for BEP application, diluted photoresist polymer films were spin-coated on a 190 nm low-*k* CDO film and analyzed by MIR IR. Figure 2.13 shows three MIR-IR spectra, in the region from 3700 to 2500 cm^{-1}, of CDO and CDO coated with two photoresist films of increasing thickness. The MIR-IR spectrum of CDO confirms the unique chemical bonding characteristics of porous low-*k* dielectric structure. The dominant IR absorption peak observed at ~2970 cm^{-1} (CH_3 asymmetric stretching) can be attributed to the extensive carbon doping, by methyl insertion, in its Si-O-Si network to create porous low-*k* CDO structure. In addition, with over coating of polymer films, MIR-IR shows additional IR absorption peaks at 3356 cm^{-1} (O-H stretch), 2930 cm^{-1} (CH_2 asymmetric stretch), 2866 cm^{-1} (CH_3 symmetric stretch) that corresponds well to the expected chemical bonding signatures of photoresist film used, Figure 2.13. Therefore, our testing clearly supports the hypothesis that MIR-IR surface evanescent wave can penetrate 190 nm low-*k* CDO film matrix to detect organic polymer films with fine resolution and high sensitivity. More importantly, as shown in Figure 2.13, MIR-IR was shown to be capable of quantitative determination of polymer residues on CDO.

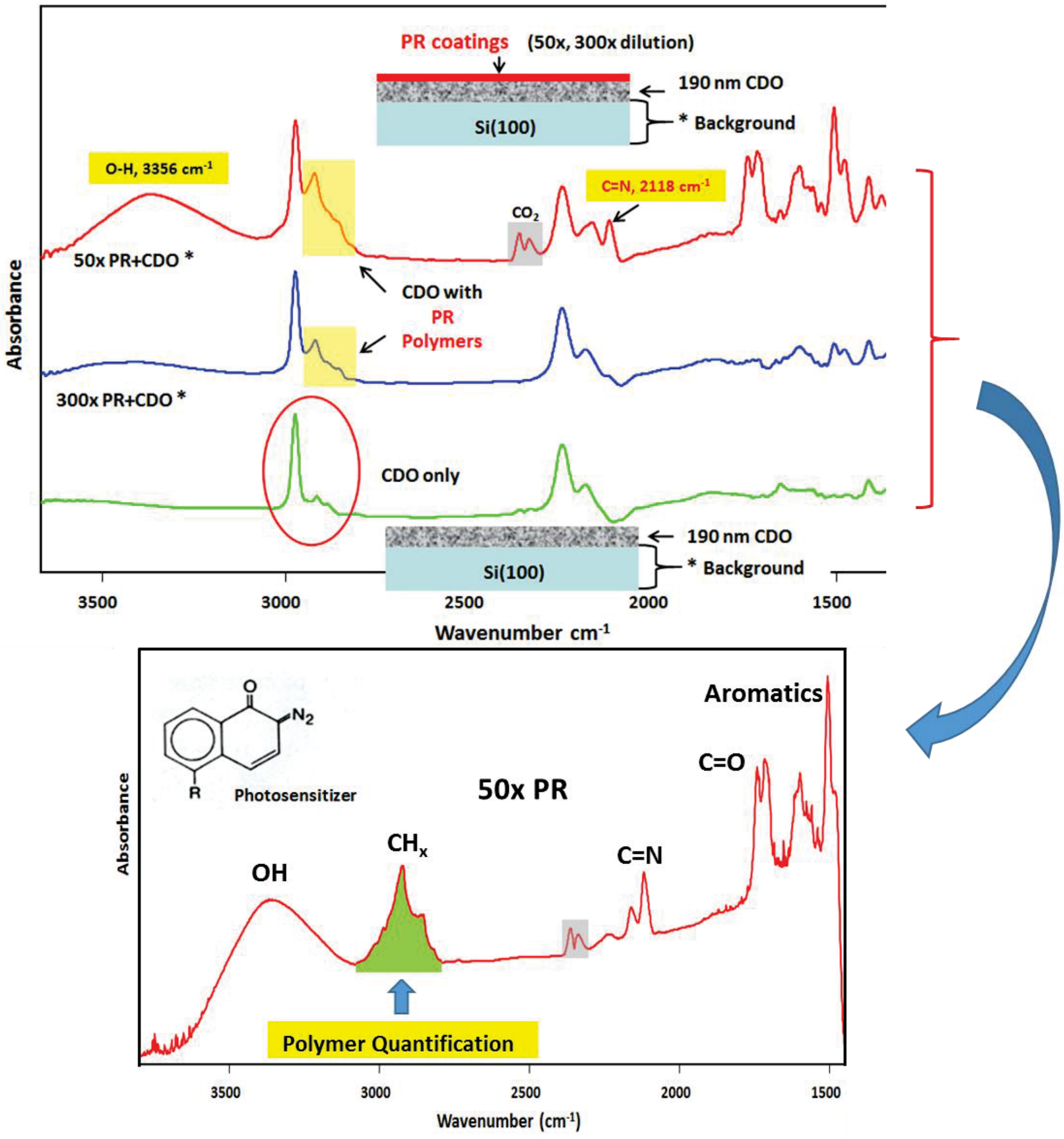

Figure 2.13 MIR-IR characterization of polymer thin films on low-*k* CDO.

2.4.5 MIR-IR characterization of organic residues removal on CDO by O_2 plasma

It is well known that oxygen plasmas will preferentially attack weaker Si-C bonds in ULK CDO and thus strip carbon, cause densification, and result in increased *k* values. In addition, carbon stripping by plasma processes also makes low-*k* ILD's more prone to water damage during subsequent wet clean processes [9-10]. In Figure 2.14, we employed MIR-IR metrology tool to monitor the time-dependent removal of organic residues from CDO surface by O_2 plasma etching. As shown in Figure 2.14, the time-progression MIR-IR spectra not only provide the valuable organic removal rate but also reveal the underlying plasma-induced damage of porous CDO. For example, early onset of moisture sensitivity due to damage from carbon stripping can be clearly seen at ~3350 cm^{-1} (O-H stretch) peak increase after 70 sec O_2 plasma etching. The increasing water uptake is self-evidenced by the rapid increasing of this ~3350 cm^{-1} (O-H stretch) MIR-IR peak with etching time. It is interesting to note that stripping carbon, i.e. methyl group extraction, can also be monitored by the growing negative IR absorption peak at ~2970 cm^{-1} (CH_3 asymmetric stretch).

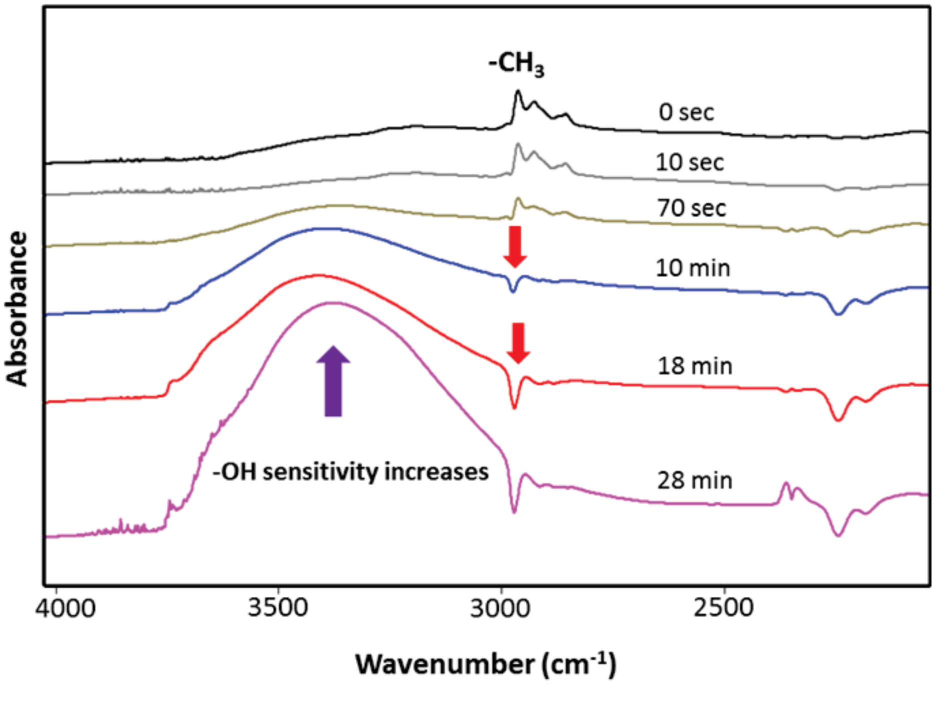

Figure 2.14 MIR-IR monitoring of dry etch cleans and underlying damages of low-*k* blanket CDO wafer.

2.5 Summary

A novel Multiple Internal Reflection Infrared Spectroscopy (MIR-IR) have been developed and optimized as a sensitive (sub-10 nm) characterization tool. MIR-IR has shown increased sensitivity compared to existing External ATR-IR and conventional transmission IR techniques. In addition, it is well compatible with patterned ILD wafer and demonstrated to be a potential tool for both front-end-line and back-end-line processing. Furthermore, MIR-IR provide critical chemical bonding information which can guide through the development of various IC fabrication steps such as silicon surface preparation, passivation, plasma processing, cleaning, restoration, doping, self-assembled monolayer (SAM) and many more.

2.6 References

1. International Technology Roadmap for Semiconductors (ITRS), 2009 edition. http://www.itrs.net/links/2009ITRS/Home2009.htm.
2. Harrick, N. J. *Internal Reflection* Spectroscopy; Wiley: New York, **1967**.
3. Mizaikoff, B. *Meas. Sci. Technol*. **1999**, 10, 1185–1194.
4. Runyan, W. R.; Bean, K. E. *Semiconductor Integrated Circuit Processing Technology*; Addison-Wesley Publishing Company: Reading, **1990**.
5. Heyns, M. M.; Nemanich, R. J. *Properties of Crystalline Silicon*: London, **1998**, 20, 219.
6. Verhaverbeke, S.; Messoussi, R.; Morinaga, H.; Ohmi, T. *Materials Research Society*: Symposium Proceedings. **1995**, 386, 3.
7. Chyan, O.; Wu, J.; Chen, J. J. *Applied Spectroscopy*. 1997, 51, 1905.
8. Bhattacharyya, D.; Pillai, K.; Chyan, O.; Tang, L.; Timmons, R. B. *Chem. Mater*. **2007**, 19, 2222.

9. Hwang, S. -W.; Lee, G. -R.; Min, J. -H.; Moon, S. H. *Surf. Coat. Technol.* **2003**, 174, 835.
10. Furusawa, T.; Ryuzaki, D.; Yoneyama, R.; Homma, Y.; Hinode, K. *Electrochem. Solid-State Lett.* **2001**, 4, G31.

CHAPTER 3

SPECTROSCOPIC CHARACTERIZATION AND BONDING STRUCTURE OF POST PLASMA ETCH-RESIDUES ON TRENCH LOW-*K* STRUCTURES

3.1 Introduction

The semiconductor industry is primarily driven by the desire related to speed and enhanced performance of the device. This is achieved through miniaturization or scaling of the number of individual functional elements into a single integrated circuit (IC) device to follow Moore's law [1]. However, the simple reduction in dimension only did not suffice on enhanced performance of the device overall speed. For instance, decrease in gate dielectric thickness led to increase leakage currents through very thin oxide layer that affected MOS transistor speed [2]. Similarly, decrease in the dimension of metal lines caused to increase in the resistance (R) and also the capacitance (C) of the interlayer increasing the overall RC delay of the interconnect thereby increasing delays in signal propagation [3]. As a result, novel materials and new techniques have been implemented in the IC fabrication schemes to support further miniaturization. Copper (Cu) replaced conventional aluminum (Al) as a metal of choice because of its higher conductivity and higher resistance to electromigration [4]. Similarly, low-*k* dielectric (lower dielectric constant) materials replaced silicon dioxide for wire insulation to reduce capacitance [5].

Although Cu is more favorable over Al as metal lines, it cannot be patterned directly by reactive ion etching (RIE) unlike Al. Cu halides, the reaction products has a very low vapor pressure, hence are non-volatile at the processing temperature [6]. An alternative technique known as 'Damascene process' is used instead, where dielectrics are patterned first and filled with copper. The schematics of BEOL processing steps is depicted in Figure 3.1. In this technique, the dielectric is deposited first via plasma enhanced chemical vapor deposition (PECVD) then patterned using photoresist (PR) mask forming trenches and vias. Plasma ashing step is performed to remove organic PR and etch residues followed by metal deposition to form interconnect between conductor layers. In modern methods, dual damascene technique is implemented where both metal lines and via holes are patterned simultaneously to reduce the number of processing steps. Excess copper after the deposition by electroplating is then removed by chemical mechanical planarization (CMP).

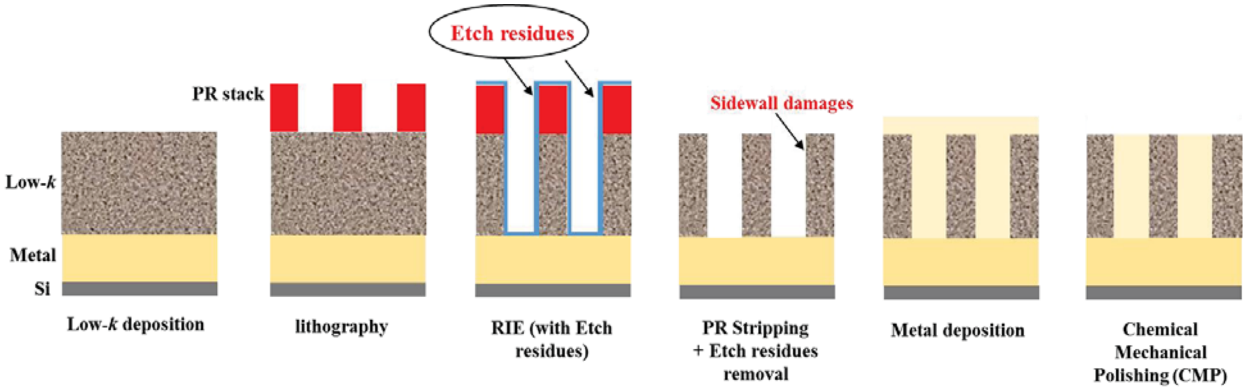

Figure 3.1 Schematic of cross section of BEOL processing steps.

Plasma technology is widely used in the semiconductor fabrication steps. One of the greatest use is for the patterning purpose of dielectric materials. Plasma generation for patterning takes place under vacuum condition usually between 1 – 100 mtorr [7], where feed gases are passed into the chamber and are ignited using an electric field in RF or microwave range. Feed gases are dissociated by the field generating ions, electrons and radicals, where continuous collision of these species form the plasma environment. Reactive ion etching (RIE), a specific type of plasma reactor is usually used for precision patterning (etching) purpose by the combined effect of both energetic ions (ion bombardment) and reactive radicals [7]. Ion bombardment by energetic ions removes material by physical sputtering and also imparts energy to the surface that enables surface reactions for radicals to form volatile products. One of the main advantages of RIE plasma etching over wet etching to create trench patterns is its high anisotropy i.e. the ability to provide vertical etching with no effect on lateral etching (keeps critical dimension intact).

Fluorine-based plasma chemistries are usually used to etch silicon and silicon dioxide materials because of the favorable SiF_4 volatile etch product formation by the reaction between silicon and fluorine radicals. Since low-*k* dielectrics are also hybrid Si-based materials (SiOCH), similar fluorocarbon gas plasmas such as CF_4, C_2F_6, CHF_3, and C_4F_8 are used for etching of dielectrics. These gases in the plasma environment dissociates into CF_x (x= 1, 2, 3) radicals and F atoms. CF_x radicals combine to form fluorocarbon polymer deposition on all surfaces including the sidewalls of the trench structures [8], while F atoms serve for dielectrics etching. Fluoropolymers deposited on the created sidewalls serves important functions to enable etching anisotropy and profile control to retain the critical dimension (CD). Moreover, the layer also prevents radical diffusion into the porous dielectrics and minimizes dielectric degradation. Studies have shown that fluorocarbon layer thickness is inversely proportional to etch rate of the underlying dielectrics [9-10]. For example, a thicker fluoropolymer layer decreases the etch rate of the underlying dielectrics by reducing diffusion of F atoms (etchants) and also minimizes the effect of energetic ions.

Ion bombardment also plays a crucial role in controlling the etch process, and dictates the fluorocarbon layer thickness. Without ion bombardment, the CF_x etch chemistry only deposits residues on both the sidewalls and trench bottoms. However with significant bombardment, residue thickness on the trench bottom is depleted while not affecting sidewalls, hence providing controlled anisotropy. This allows fluoropolymer thickness reduction, enhances reaction rate as well as enables diffusion of reactants through the layer for reactions [11]. Fluoropolymer thickness is critical because it dictates the etch rate of the underlying materials, and hence it is important to balance between etching and deposition of the material and polymer respectively. An important parameter to tune in the etch chemistry (fluorocarbon gas mixture) is the polymerization rate, given by the F/C ratio, which dictates the degree of etching and deposition of polymer on the dielectric surface. A weak polymerization (high F/C) will cause fluorine radicals to react with the vertical sidewalls and cause bowed profile and fluorine contamination into the porous low-*k* dielectric [12]. On the other hand, strong polymerization (low F/C) will result in heavy polymer deposition and sloped profiles and will cause post-etch cleaning difficulties. However, when the etch rate and polymerization rate is well balanced, a layer of inhibitive fluoropolymer passivates the sidewalls resulting in a vertical etch profile. There are two approaches to control the polymerization rate. First way is by mixing low (CF_4) and high polymerizing (CHF_3 or CH_2F_2) gases in a balanced/correct proportion. Second approach is by using additives such as oxygen and nitrogen along fluorocarbon gases that will prevent polymer deposition, thereby increasing etch rate [12].

Even though deposition of fluoropolymer is important to maintain vertical etch profile, subsequent removal is a must in the later process steps to obtain high adhesion and good coverage, avoid fluoride contamination and poor electrical contact [13-14]. These fluoropolymers are removed from the structures by a combination of dry strip and a wet clean. Ash chemistry based on oxygen, nitrogen and hydrogen plasmas are often used but the problem of plasma induced damage to porous dielectrics is encountered which makes dielectrics more hydrophilic [15-16]. Wet clean based on dilute HF are not efficient for polymer removal without etching the underlying dielectric leading to CD loss. An alternative approach to polymer removal is done by using organic solvents which shows good removal efficiencies, however high temperature and longer processing time is required [17-18]. Recently, effect of UV irradiation followed by wet clean have shown efficient polymer removal, however some structural modification on the underlying low-*k* was also observed [19].

In order to help create highly reliable interconnects, knowledge of detail chemical bonding information of fluorocarbon residues is essential. In-depth knowledge of the structure of polymer will facilitate better cleaning formulations with no modification/degradation of low-*k* materials. In this study, we evaluated the detail chemical bonding structure of fluorocarbon polymer deposited on a patterned low-*k* trench structures using FT-IR, XPS, SEM and functional group specific chemical derivatization. In addition, the effect of designer etch chemistry on the modification of chemical bonding composition of fluorocarbon layer was also studied, which can potentially lead to a more clean efficient plasma etching process.

3.2 Experimental

Dielectric trench pattern

Trench patterns were created on 340 nm CDO dielectric film (10-30% porosity, $d < 2$ nm) using a LAM Research 2300 Exelan etch platform. The trench patterns consisted of three different pitches: 180 nm, 270 nm, 630 nm and with three different polymer thickness 1x, 3x and 5x: referring to polymer deposition time in seconds. The etch gas mixture of CH_2F_2 and CF_4 was optimized to create patterns on the dielectric material that led to deposit minimal fluorocarbon residues. The subsequent plasma treatment of $CHF_3/C_4F_8/Ar$ gas mixture was optimized to deposit conformal MFP of varying thickness (1x, 3x, and 5 x) on the CDO trench structures.

Film characterization

Blanket and trench patterned wafers were cut and fabricated into attenuated total reflectance (ATR) coupons of 60 x 10 x 0.8 mm dimensions with 45° bevel angle edges. MIR-IR and Transmission IR (T-IR) spectra were measured using a Bruker Equinox 55 FT-IR spectrometer under constant dry air ($CO_2 < 1$ ppm) purge. All spectra were collected at 4 cm^{-1} resolution as the average of 100 individual spectra. XPS analyses were conducted using a PHI 5000 VersaProbe equipped with Al Kα (1486.7 eV) radiation and electron flood gun to neutralize the sample charging.

Functional group specific chemical reactions

All chemicals were obtained as reagent grade from Sigma-Aldrich. *For C=O*: Wafer coupons were immersed in a 2,4-dinitrophenylhydrazine (DNPH) solution (0.06 gram DNPH, 10 mL isopropyl alcohol and 150 μL of 12M HCl) and heated at 70◦C for 16 hours. *For C=C*: Wafer coupons were immersed in a 30 mL capped glass vial containing 20 mL of bromine and heated at 50◦C for 1 hour. *For CF_x:* A Na/Naphthalenide etchant (Creative Engineers, Inc.) was used. FTIR and XPS measurements were performed after wafer coupons were rinsed thoroughly with ample amount of ultrapure water (18.2 MΩ.cm, C content < 2 ppb) and isopropyl alcohol followed by N_2 blow dry.

Nafion thin film preparation

Commercially available 5 wt % Nafion (EW 1100) solution in water/alcohol mixture was obtained from Sigma-Aldrich. Nafion solutions of two different dilutions (100x and 1000x) were prepared by adding appropriate amount of isopropyl alcohol to the stock 5 wt % Nafion solution.

Drop casting method was employed to prepare thin films of Nafion on 340 nm CDO blanket wafers. After proper drying time of > 1 hour, FT-IR and AFM measurements were performed.

Post-etch residues cleaning

TMAH based proprietary chemistry (pH > 13) was used for post-etch residues cleaning. Wafer coupons were immersed in a cleaning solution at 50 °C with sonication for appropriate time. FT-IR and XPS measurements were performed after rinsing with ultrapure water followed by N_2 blow dry.

3.3 Results and Discussion

3.3.1 Nafion thin film to simulate post-etch residues on low-*k* substrate

To simulate post-etch residues on low-*k* substrate, first the chemical bonding evolution of Nafion thin film was investigated. Two different dilutions of Nafion (100x and 1000x) were spin coated on 190 nm carbon doped oxide (CDO) blanket wafer followed by vibrational spectroscopy analysis. Figure 3.2 shows IR spectra of CDO + 100x and CDO + 1000x Nafion (solid line) with their respective CDO only spectra (dashed line). Difference in the IR absorption bands between CDO only and CDO + Nafion is very subtle because the spectroscopic features of Nafion are masked by the broad absorption band of low-*k* between 700 cm^{-1} – 1400 cm^{-1}, Figure 3.2.

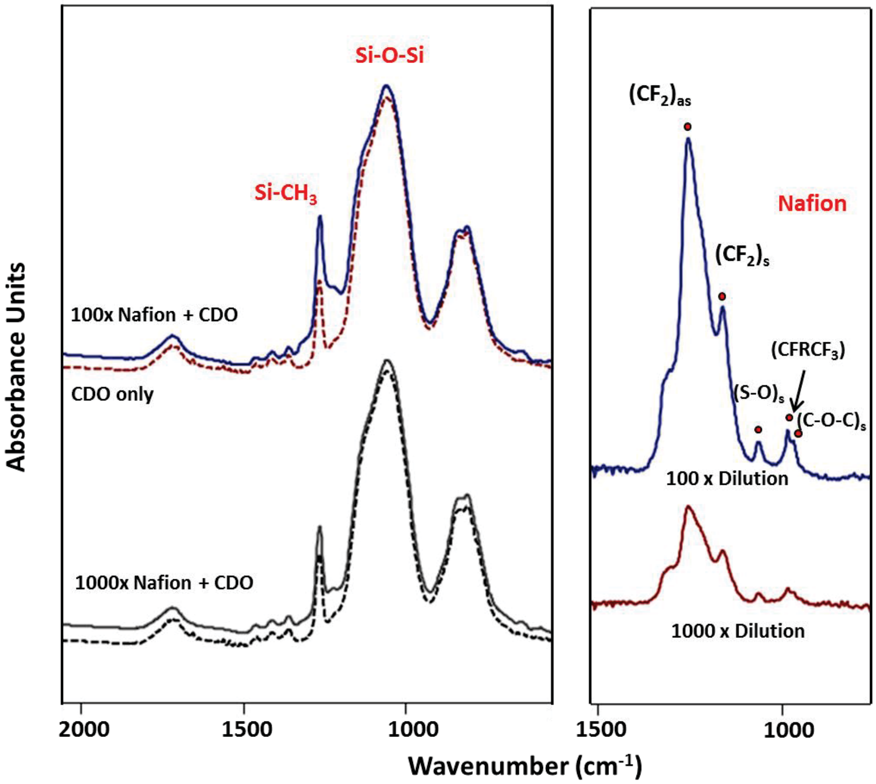

Figure 3.2 Isolate Nafion coatings from 190 nm CDO blanket wafer by proper background cancellation.

Nafion is a copolymer with a tetrafluoroethylene backbone with pendant side chains of perfluoronated vinyl-ethers terminated by sulfonic acid groups. Enabled by precise CDO background cancellation, all IR absorption peaks related to Nafion thin films on low-*k* substrate was obtained with superior spectral resolution. Figure 3.2 (right), are the IR spectra of 100x and 1000x Nafion thin films respectively obtained by cancelling out the bulk absorption CDO low-*k* substrate. Increased dilution of Nafion concentration correlates to decreased IR absorption peaks intensity as expected. Both exhibit strong and broad IR absorption bands between 1100 – 1300 cm^{-1} carrying multiple vibrations. The dominant main IR peaks at ~1160 cm^{-1} and ~1240 cm^{-1} can be assigned to symmetric and asymmetric CF$_2$ stretching modes respectively [20]. The shoulder peak at ~1310 cm^{-1} can be attributed C-C chain stretching [21]. In addition to the main CF$_2$

stretching vibrations, some fundamental vibrations of the pendant chains are also clearly recognized. Among them, the symmetric stretching of the sulfonic group ($-SO_3^-$) at ~1060 cm^{-1} [21], and the doublet peaks at ~970 cm^{-1} [21] and ~980 cm^{-1} [20] assigned to C-O-C symmetric stretching and C-F stretching ($-CF_3$ group), respectively.

3.3.2 Characterization of chemical bonding structure of model fluorocarbon polymer on low-*k* trench structures

For this study, trench patterns consisting of three different pitches of 180, 270 and 630 nm corresponding to different line spacing and with ~120 nm trench depth was created on ~340 nm low-*k* dielectrics. After trench opening, a plasma gas mixture of $CHF_3/C_4F_8/Ar$ was tuned (vary F/C ratio) to deposit conformal fluorocarbon thin films of three different thickness (1x < 3x < 5x, verified by SEM) on the low-*k* trench patterns (both sidewalls and bottom). Infact, these fluoropolymers are deposited purposely to achieve precise profile control and minimize dielectric damage in anisotropic etching of the dielectrics. No polymer low-*k* trench wafer corresponds to wafers gone through cleans treatment to remove most of the residues, however a small amount of residual polymer can be expected on the wafers. Cross section SEM images shown in Figure 3.3 corresponds to no polymer (Figure 3.3a) and with 1x polymer (Figure 3.3b) of three different pitch structures.

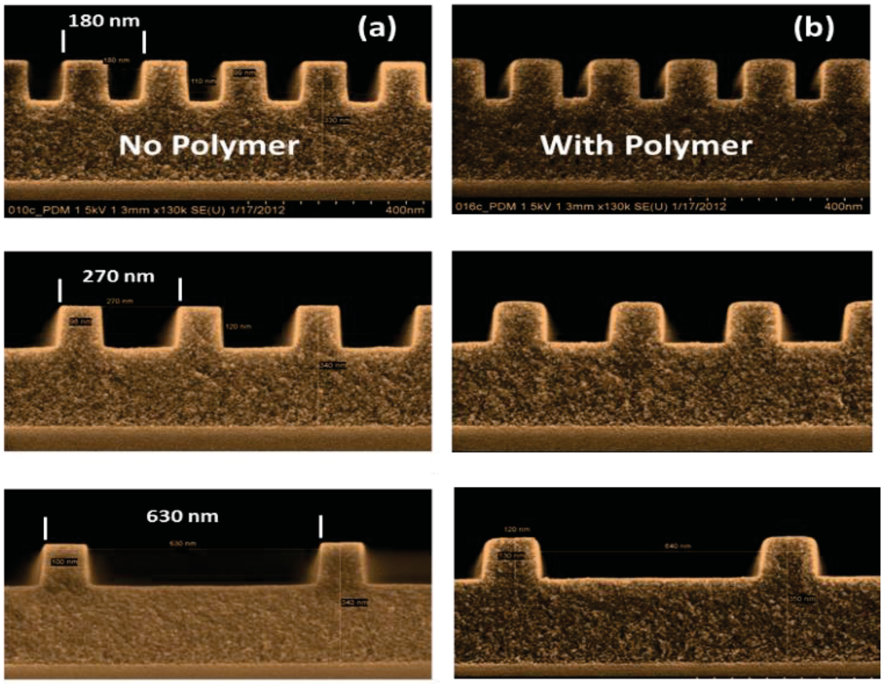

Figure 3.3 Cross section SEM images for the patterned ILD structures (a) no polymer and (b) 1x polymer on three different pitches.

FT-IR spectroscopy in transmission (T-IR) mode fully optimized at brewster angle was applied to trench patterned structures to extract useful chemical bonding information of the MFP residues. Figure 3.4 shows T-IR spectra of patterned low-*k* only with no polymer of three different pitches. The characteristic features of low-*k* such as Si-O-Si cage (~1130 cm^{-1}), Si-O-Si network (~1060 cm^{-1}), Si-CH_3 bending (~1265 cm^{-1}) and Si-CH_3 rocking mode (~830 cm^{-1}) can be observed and is consistent with previous studies done on low-*k* materials [15].

T-IR spectra reveal that ILD content increased with tighter pitch (180p > 270p > 630p) as can be seen from the corresponding increase of all the characteristic low-*k* IR absorption bands, Figure 3.4. The obtained IR spectrum of the low-*k* dielectrics from each pitch structure was then used to subtract from their respective low-*k* with polymer structure to obtain spectrum of the etch polymer only, Figure 3.5.

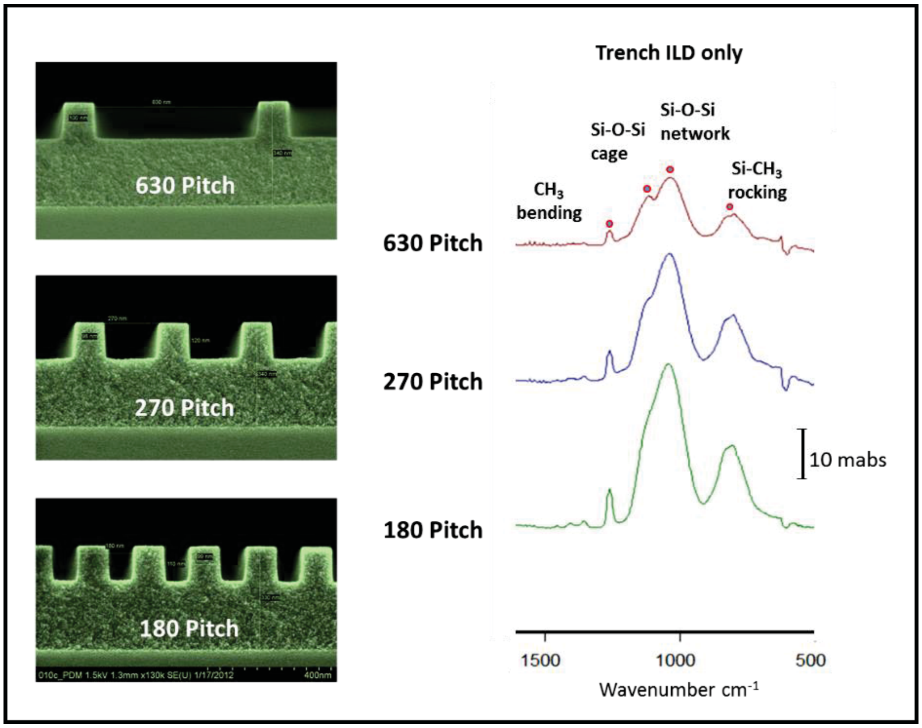

Figure 3.4 Bonding structure of low-*k* substrate only from three different pitch (630p, 270p and 180p).

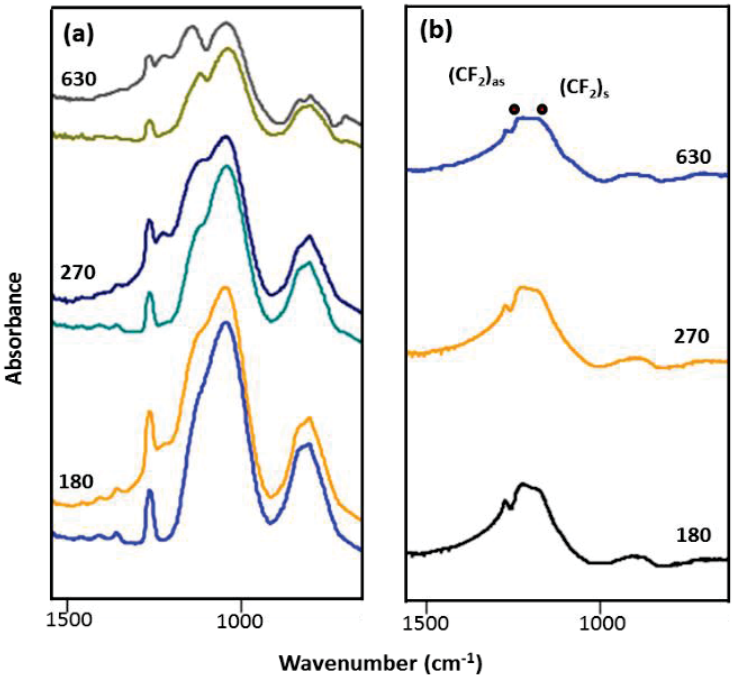

Figure 3.5 Isolate 1x FC polymer from three different pitches (630 nm, 270 nm and 180 nm). ILD + polymer and ILD only (a) and 1x polymer only (b).

Figure 3.5a shows two different types of spectra obtained from low-*k* + 1x polymer (top) with their respective low-*k* only spectra (bottom) from 180, 270 and 630 pitch. Each of the spectrum shown is collected with respect to clean bare Si (HF etched back to remove low-*k* stack followed by SC1 clean to remove organics) of the same crystal, a technique termed as "single crystal subtraction". The technique is basically utilized to minimize any background cancellation issues it might have (e.g. from different dopant level between different substrates and or organics adsorbed etc.). Figure 3.5b represents spectra of 1x polymer only isolated from low-*k* + 1x polymer structures by cancelling out the bulk absorption contribution from the low-*k* material. This can be achieved in two ways: (i) by subtracting low-*k* only ratio spectra from low-*k* + polymer ratio spectra, and (ii) direct rationing of low-*k* + polymer single beam (as sample) with respect to low-*k* single beam (as background). Either case, the resultant ratio spectra of the polymer would be the same. The obtained IR spectra of 1x MFP from three different pitch structures (Figure 3.5b) contains majority of IR peak absorption at ~1230 cm^{-1} for CF_2 asymmetric stretch and ~1180 cm^{-1} for CF_2 symmetric stretch, referring to large amount of CF_2 groups in the MFP residues. When CF_2 IR peak intensity, corresponding to the amount of CF_2 groups is plotted against different pitch sizes, Figure 3.6, shows increasing amount of residues with tighter pitch trench structures. With more of a sidewalls surface exposed and higher ILD content in 180 nm pitch, more etch residues is observed in the IR spectra, than wider pitch structures (180p > 270p > 630p).

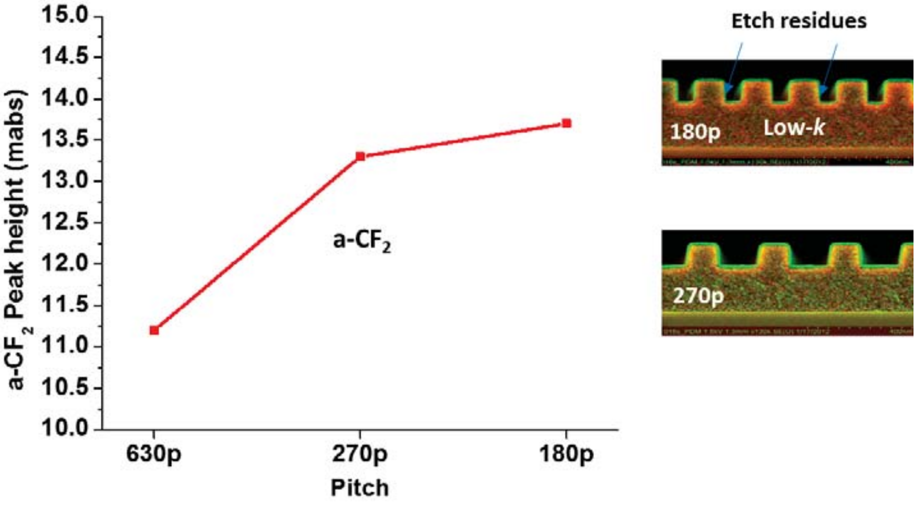

Figure 3.6 Plot of CF_2 peak intensity of FC 1x polymer (~6 nm) on 630 nm, 270 nm and 180 nm pitch structures.

Figure 3.7 shows IR spectra of 1x, 3x and 5x (corresponding to different deposition times) MFP residues on 180 nm pitch (~80 nm wide low-*k* trench line) low-*k* structure. Cross section SEM reveals 1x, 3x and 5x MFP corresponds to 6 nm, 17 nm and 28 nm polymer thickness (±2 nm), respectively. IR data show that all three MFP residues of different thickness exhibit similar IR spectroscopic features. The major (strongest) IR absorption bands (Figure 3.7) is observed at ~1230 cm^{-1} and ~1180 cm^{-1} assigned to asymmetric and symmetric stretching modes of the CF_2 group, respectively [22-23]. However, the broad 1050 – 1500 cm^{-1} region carries multiple other peaks beside CF_2 stretching vibrations. Stretching vibrations in the region ~1325 – 1365 cm^{-1} can be assigned to terminal CF_3 group (CF_3CF_2) [22] and CH_3 bending mode at ~1460 cm^{-1}. Besides the strongest IR bands between 1050 – 1500 cm^{-1} region, other weaker absorptions such as internal CF_3 group vibrations at ~930 cm^{-1} [24] and CF_2 deformations (amorphous) at ~730 cm^{-1} [23] are also observed.

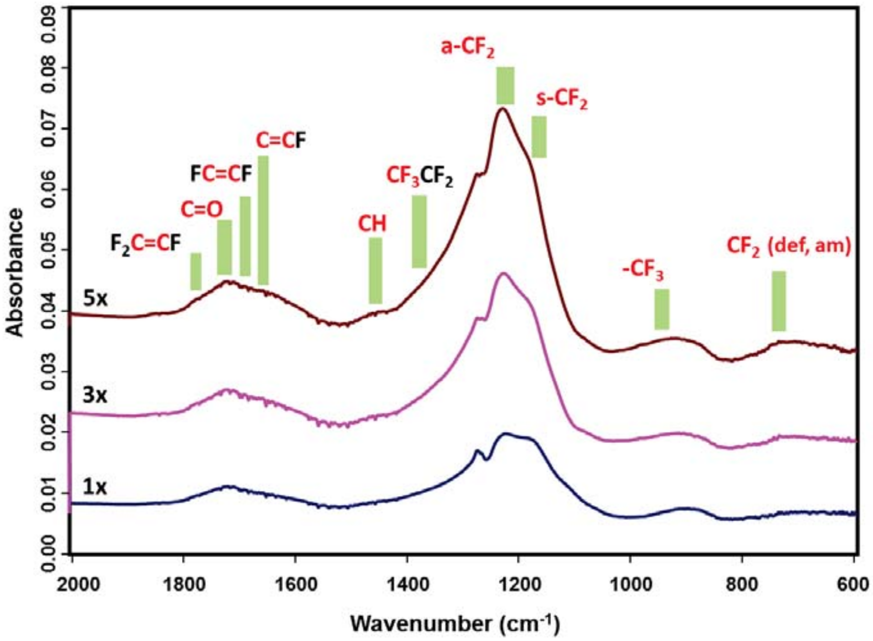

Figure 3.7 IR spectroscopic features of three different polymer thickness (1x, 3x and 5x) from 180 nm pitch trench low-*k* structure.

XPS analyses on the comparison of 1X, 3X and 5X polymer samples (Figure 3.8) also show consistent increase in the peaks with considerable differences between 1X sample and the rest which did not show much difference between them. This could be because the thickness in 3X and 5X samples is already way more than the X-ray penetration in XPS and that why we could not see much difference between 3X and 5X polymer samples. Moreover, all IR spectroscopic features of fluorocarbon (FC) residues increases in peak intensity with increasing deposition times (1x < 3x < 5x), as shown in Figure 3.7. IR spectra also show that thicker film exhibits sharper spectroscopic features compared to the thinner FC film. IR data correlated very well with the FC polymer thickness observed by SEM. Figure 3.9 is a plot of IR peak (CF_2) intensity and polymer thickness (SEM) correlating to 1x, 3x and 5x polymer. Both data show linear increases with higher deposition time (increased thickness).

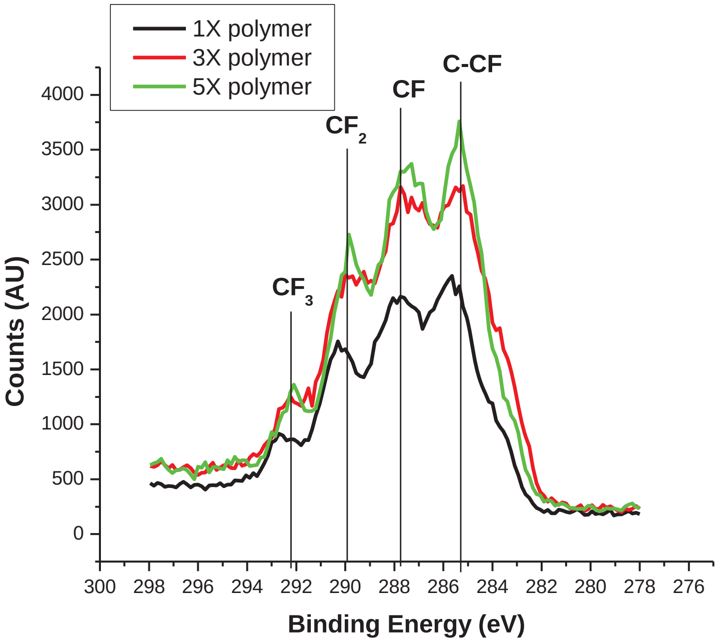

Figure 3.8 XPS C 1s spectra of 1x, 3x and 5x MFP fluoropolymer.

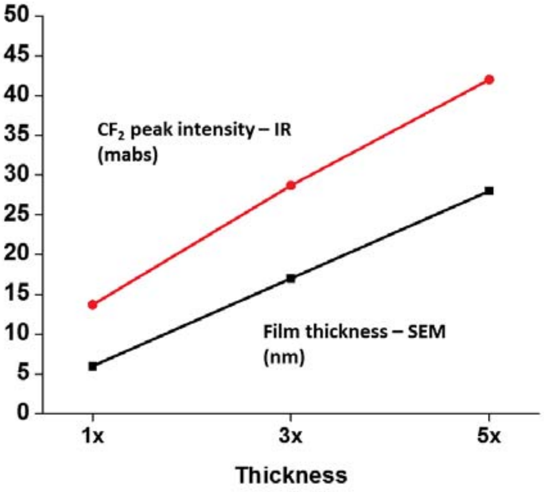

Figure 3.9 Plot of CF_2 peak intensity (IR) with different deposition times of FC residues, compared to thickness measured by SEM.

The obtained IR spectra of MFP residues was then compared with two other polymers with the fluorocarbon groups (Teflon and Nafion), to delve more into the detail structure of etch residues polymer. Figure 3.10 shows the FT-IR spectral comparison of Teflon, Nafion and 5x etch polymer (~28 nm), all three showing dominant IR absorption band at ~1230 cm^{-1} and ~1180 cm^{-1} for CF_2 asymmetric and symmetric stretching respectively. Teflon (polytetrafluoroethylene, PTFE) is a long linear $-(CF_2-CF_2)-_n$ polymer chain, produced by free-radical polymerization of tetrafluoroethylene ($F_2C=CF_2$) monomers. IR shows several distinct, well resolved, rather than broad regions of absorption, attributed to the existence of discrete configurations resulting from the high rotational barriers [25]. The observation of sharp peaks on the lower end at 641 cm^{-1}, 555 cm^{-1} and 512 cm^{-1} assigned to CF_2 wag, CF_2 deformation and CF_2 rocking modes respectively [20-21], is also consistent with the highly crystalline and more ordered nature of Teflon. Nafion on the other hand has major absorption bands in the broad region of 1100 – 1360 cm^{-1}. As discussed earlier, several vibrations can be accounted for within the broad region beside major CF_2 stretching vibrations. Nafion membrane can be described as PTFE backbone with pendant side chain with terminating sulfonic groups. The broadening of the main peaks can be due to the disorder induced by grafting of side pendant etheroxide chains [21]. The ionic character of these chains can also promote the disorder [21]. Furthermore, CF_2 wagging, deformation and rocking vibrational modes are not sharp, are broad and reduced in intensity, indicating loss of PTFE crystallinity.

In contrast, IR spectrum show significant differences in chemical bonding structure in the MFP residue. It shows higher extent of broadness of CF_x ($x = 1 - 3$) bands in the region 1040 – 1500 cm^{-1} where dominant absorptions are observed, Figure 3.10. This most likely represents a composite overlap between various bonding of CF_2 stretching modes (a-CF_2 and s-CF_2), CF

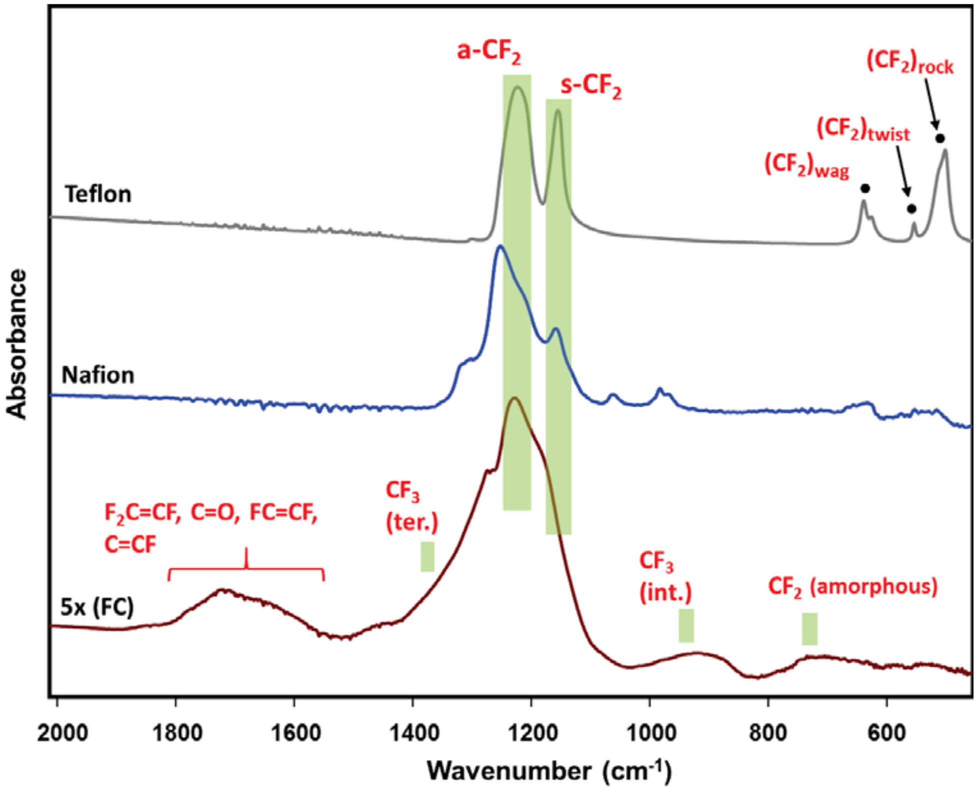

Figure 3.10 FT-IR spectral comparison between Teflon, Nafion and 5x polymer (28 nm).

stretch (~1340 cm-1) and terminal CF_3 group (1325 – 1365 cm^{-1}). The lack of definite distinction between less resolved CF_2 stretching modes (a-CF_2 and s-CF_2) in the residues suggest a highly complex, disordered and highly amorphous polymeric thin film. The small peak observed at ~740 cm^{-1} for amorphous CF_2 deformation also supports the chain disorder. More evidently, the lack of CF_2 wagging, deformation and rocking modes (641 cm^{-1}, 555 cm^{-1} and 512 cm^{-1} respectively) is an indication of heavy loss in crystallinity of the MFP film as compared to more ordered Teflon structure. The observation of terminal CF_3 group vibrations (1325 – 1365 cm^{-1}), CF vibration (1340 cm^{-1}), internal CF_3 group vibration (~ 930 cm^{-1}) and amorphous CF_2 deformation (740 cm^{-1}) is consistent with crosslinking/branching within the polymeric microstructure.

In addition, a broad absorption bands in the region 1530 – 1850 cm^{-1} observed in the IR spectrum provide other useful chemical bonding information in the MFP residues, beside the major CF_2 vibrations, Figure 3.10. The broad region can be attributed to unsaturated olefins (C=C) with different number of fluorine groups attached, and a carbonyl (C=O) functionality. Fluorinated double bonds such as –C=CF-, -FC=CF- and F_2C=CF- are accounted at 1671 cm^{-1}, 1717-1730 cm^{-1} and 1780-1800 cm^{-1} respectively [26]. The stretching mode of C=O functionality is assigned at 1705 – 1725 cm^{-1} [22]. Overall, etch residue polymer showed a complex film composition and structure. This can be linked to complex plasma environment, where plasma excitation generates a large number of different activated species such as energetic ions, electrons and reactive radicals because of the presence of higher energy electrons (wide energy distribution). The variability in monomer fragmentation into polymerizable radicals (CF_x) in the PECVD medium can result into various bonding configurations that are observed in the IR spectrum of deposited polymeric film.

To support FT-IR data, XPS analysis was conducted which gave further insight into the composition of the thin polymer film. Figure 3.11 shows the C 1s XPS spectra of low-*k* film after being etched (no polymer deposition) and with subsequent 1x polymer deposition (~6 nm) on 180 nm pitch low-*k* structure. No polymer dielectric surface as expected showed a huge peak intensity of C-C, C-Si groups (284.6 eV) coming from the dielectric material composition. XPS analysis of sample without polymer coating after dielectric etch also exhibited some fluorine containing groups (C-CF_x) at the surface. After 1 min of Ar^+ sputtering the C-CF_x peak was removed and a considerable increase in Si-C peak was observed (spectra not shown). F 1s peak showed a huge CF_2 peak at 688 eV and after 1 minute of Ar^+ sputter the peak was greatly reduced and shifted to 686 eV which corresponds to F-Si peak. The subsequent sputtering resulted in reduction of the F-Si peak. Analysis of Si 2p spectra further confirmed the presence of Si-C peak which was present even before Ar$^+$ sputtering together with SiO_x peak. After 5 minutes of sputtering, both peaks were still present (spectra not shown). The C 1s spectrum of 1x MFP film indicates the existence of

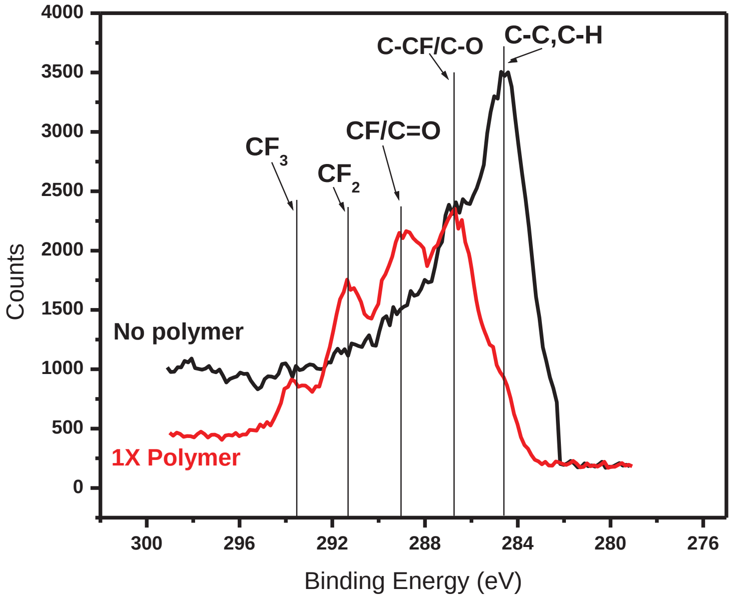

Figure 3.11 XPS C 1s spectra of 1X Polymer (6 nm) Vs. No Polymer.

various CF_x moieties and can be deconvoluted into five gaussian peaks (deconvolution not shown) assigned to CF_3 (293.5 eV), CF_2 (291.3 eV), CF/C=O (289 eV), C-CF_x/C-O (286.8 eV) and C-C or C-H (284.6 eV) which symbolizes the presence of fluorocarbon polymer, Figure 3.11. The absolute binding energies of the mentioned specific bonds in the polymer fall well within the range given in the literatures [26]. The surface composition of the thin fluoropolymeric film acquired was 55% carbon, 35% fluorine, and 10% oxygen. Incorporation of oxygen is common in plasma deposited films which is likely due to atmospheric exposure following the plasma deposition process [8]. The F/C ratio can easily be calculated from the integrated intensities of the various components derived of deconvoluted C 1s spectrum. The presence of fluoropolymer was further confirmed by F 1s peak at 688.4 eV (spectra not shown). Time dependent Ar$^+$ sputtering was done and resulted in lowering of the peak intensities but even after 10 minutes the fluorocarbon signature peaks were still present. Si 2p peak was absent even after 10 minutes of Ar^+ sputtering which indicates that the polymer coating was thick and the 10 minutes of sputtering did not reach the ULK dielectric underneath.

3.3.3 Functional group specific chemical derivatization reactions

FT-IR spectrum of MFP (Figure 3.10) shows overlapping absorption bands in the region 1530 – 1850 cm^{-1} for fluorinated alkenes and carbonyl functionalities, also supported by XPS measurement (CF/C=O) (Figure 3.11). The spectrum also shows overlapping of CF_x stretching modes. To unravel overlapping absorption bands, functional group specific chemical reactions that specifically attack the targeted groups were performed to confirm CF_x, alkene and carbonyl moieties embedded in the polymer chain. The obtained IR spectrum from the derivatization reactions clearly reveals the associated bonding transformations on the fluorocarbon polymer and confirms the presence of the functional groups mentioned above.

Sodium naphthalene complexes are commonly used radical anions known to be an effective defluorinating agent to modify fluorocarbon surfaces [27]. When the complex is treated on fluorocarbon polymer, the electron transfer from the naphthalene radical anion to the electron poor carbon backbone (on polymer) destabilizes the polymer, which causes C-F bond to break and the resulting F^- is scavenged by the Na^+ cation [28-29]. Figure 3.12 demonstrates FT-IR spectra of time dependent defluorination reaction of 28 nm MFP residues on low-*k* trench patterns at room temperature. Progressive defluorination process is explained by the gradual decrease of CF_2 stretching vibration band at 1180 and 1230 cm^{-1}. Radical anion treatment showed ~50% decrease

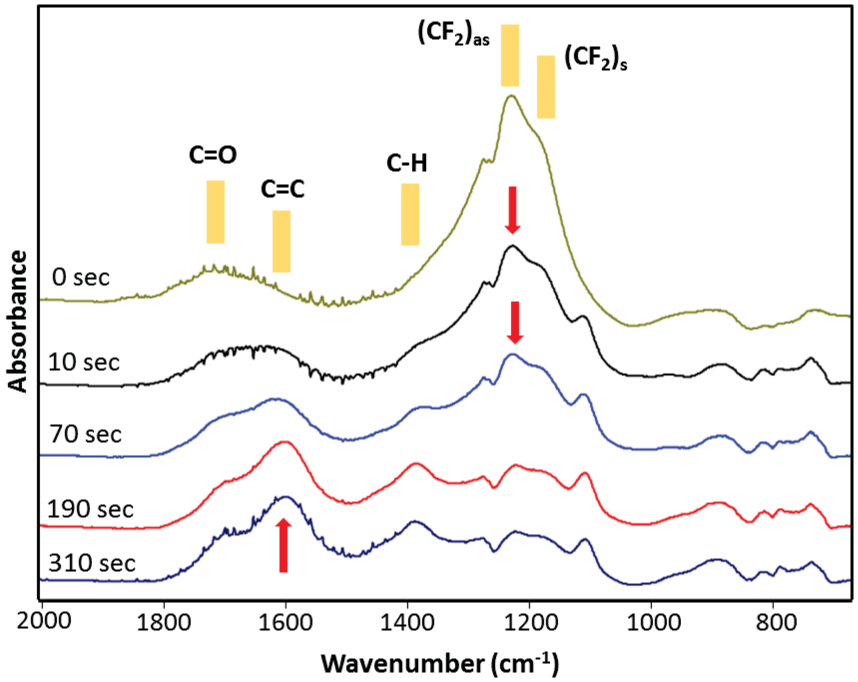

Figure 3.12 Time dependent FT-IR spectra of 28 nm fluoropolymer upon radical anion treatment (0 – 310 sec).

in 10 sec and defluorination near completion at ~300 sec of the treatment time. The difference in removal rates might come from diffusion-limited reaction as the reactant penetrates the fluorocarbon film. Concurrently, two new increasing absorption bands are also observed with progressive defluorination at ~1396 and ~1600 cm^{-1} accounted for CH deformation and C=C stretching (alkene products) respectively. The formation of alkene products come from carbon radical coupling and is consistent with previous literatures [29].

Brady's test, a well-known chemical analysis based on the reaction between 2, 4-dinitrophenylhydrazine (DNPH) and carbonyl functionality (C=O) was used to verify the presence of carbonyl of a ketone or aldehyde in the fluorocarbon matrix. The reaction can be described as addition-elimination reaction whereby nucleophilic addition of $–NH_2$ group to C=O group followed by elimination of a H_2O molecule. The mechanism for the reaction between DNPH that specifically targets C=O functionality forming a dinitrophenylhydrazone product is shown in Equation 1 below [30].

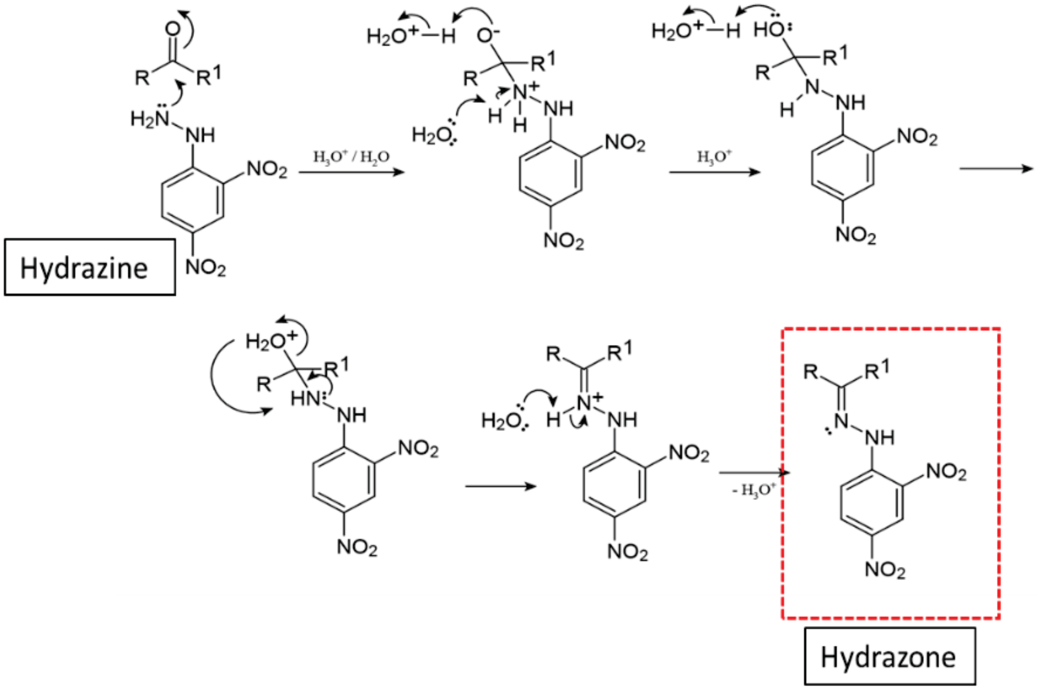

IR spectra in Figure 3.13 reveals detail chemical bonding transformation taking place on the MFP residues after the derivatization reaction with DNPH. The differential spectrum (after reaction – before reaction) in Figure 3.13(i) shows a negative absorbance (removal) band at 1710 cm^{-1} that is attributed to C=O stretching frequency and is indicative of the presence of C=O functionality in the MFP residue. The dinitrophenylhydrazone adduct formed after the derivatization process is indicated by the emergence of strong positive absorption band at 1619 cm^{-1} for C=N (imine) stretching vibration. Other significant absorption bands associated with the adduct formation are: N-H (amine) bending at 1596 cm^{-1}, NO_2 symmetric and asymmetric stretching vibrations at 1341 cm^{-1} and 1505 cm^{-1} respectively, and C=C of aromatic ring stretching at ~1500 cm^{-1} [31]. The observation of small positive peak at the higher frequency (~3314 cm^{-1})

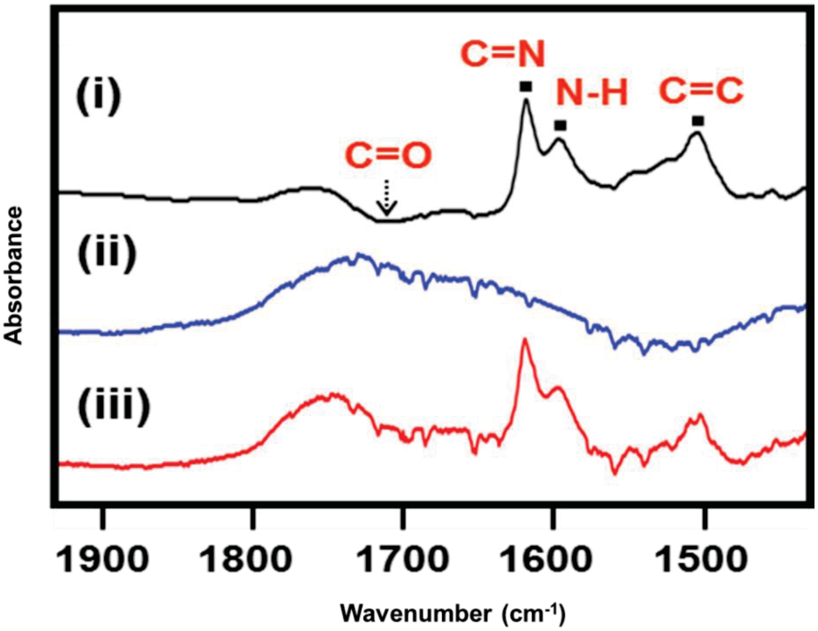

Figure 3.13 Identification of C=O by DNPH derivatization reaction. Differential spectrum (i) obtained by subtracting (ii) from (iii), as-deposited MFP spectrum (ii), and film after derivatization (iii).

is consistent with N-H stretching of the hydrazone and indicates the presence of ketone in a parent MFP residue [31]. XPS N 1s analysis also shows the appearance of a weak C=N band at ~401 eV

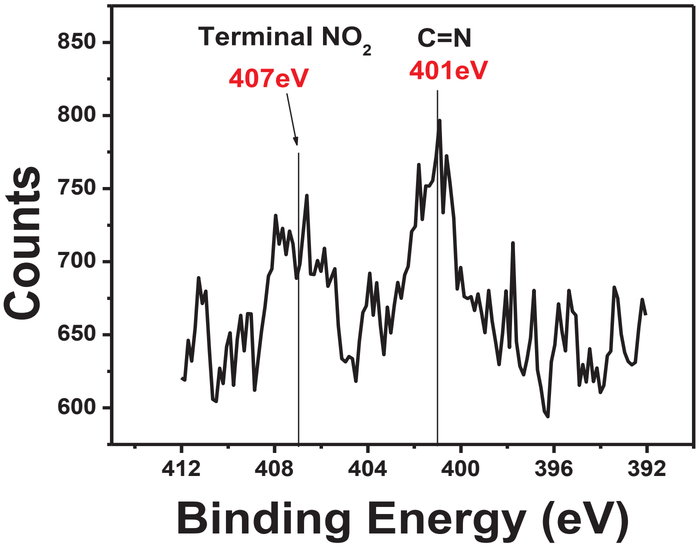

Figure 3.14 XPS analysis of N 1s spectrum after DNPH treated MFP residue.

and NO_2 at ~407 eV consistent with hydrazone derivative formation as shown in Figure 3.14, also supports the observation from IR analysis (Figure 3.13). To further delve into the amount of C=O in the as-deposited MFP residue, 1 and 2 minutes Ar^+ sputtering was performed as shown in Figure 3.15. After 1 minute of sputter time, XPS shows substantial decrease in the C=O peak, indicating that C=O is most likely on the surface of the residue. This can very well be accounted to oxidation of the surface with the ambient environment after plasma processing step.

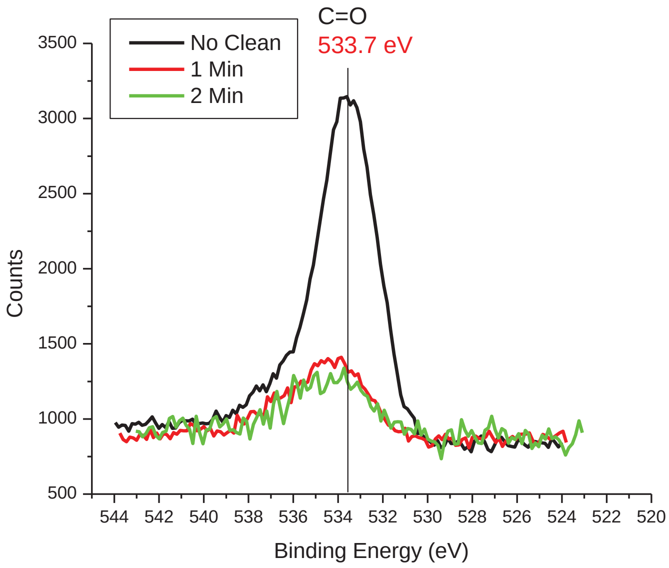

Figure 3.15 XPS analysis of C=O in as-deposited MFP before and after Ar^+ sputtering.

Bromination (Br_2 addition) is a chemical reaction in organic chemistry to react with alkene bond to form bromo products. To decipher the broad overlapping IR absorption band at 1530 – 1850 cm^{-1}, and confirm the presence of alkene groups (C=C) within, bromination reaction was carried out on the MFP residue. The mechanism scheme is illustrated in Equation 2 below. Figure 3.16 shows IR spectra of 28 nm MFP treated with bromine solution with detail chemical bonding modification on the surface. The differential spectra 3.16(a)i which is the net change after Br_2

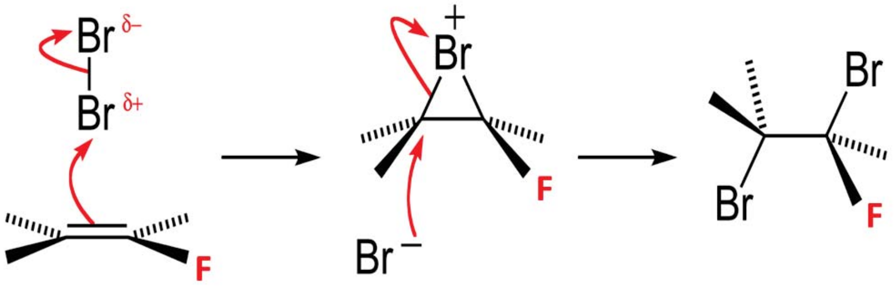

treatment results in a broad negative band centered around 1670 cm^{-1} conforming selective removal of double bonds (C=C) from the residue. Since both C=O and C=C has π bonds, however weaker π bond in C=C (~1670 cm^{-1}) is more prone to Br_2 addition reaction than C=O (~1710 cm^{-1}), and is observed in the IR spectra. Concurrently, other significant bonding modifications are

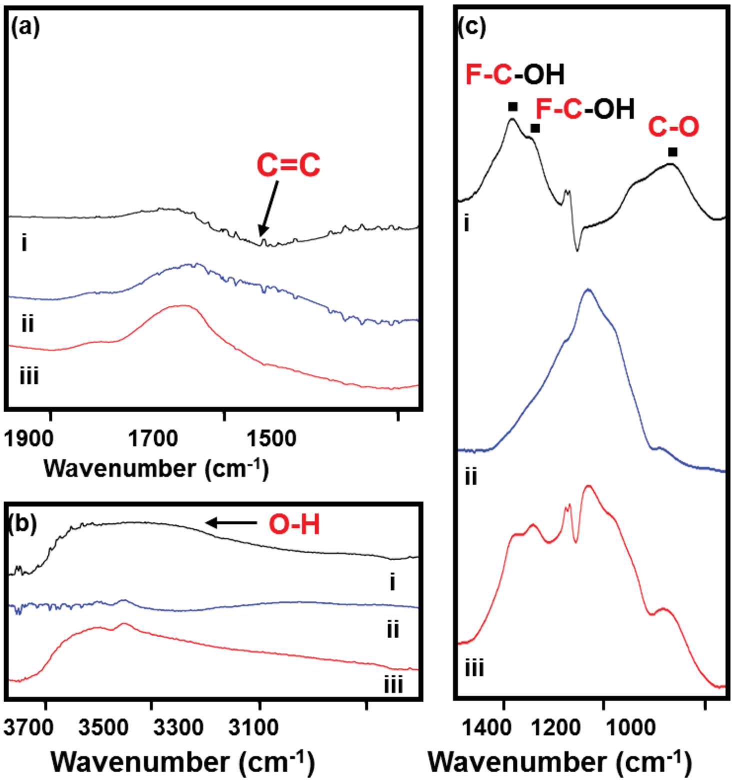

Figure 3.16 Comparison of (a) C=C stretching, (b) O-H stretching and (c) C-F/C-O stretching bands in FT-IR spectra of a Br_2 treated 5x MFP; (i) differential, (ii) before treatment and (iii) after treatment.

also observed on the film surface. The expected bromo product after Br_2 addition to C=C is observed at ~1400 cm^{-1} for FC-Br vibration. XPS analysis also confirms the observation of new Br 3d peak (71.2 eV) formed after the treatment as shown in Figure 3.17. Both IR and XPS analyses supports C=C functionality in the fluoropolymer residue. In addition, a different reaction pathway also follows when water molecules react with the bromonium ion (intermediate product) to form di-hydroxy product (FC-OH) as seen in the IR spectra. The observation of increase of O-H stretching band at 3100 – 3700 cm^{-1}, -OH and –Br substituted C-F at ~1400 cm^{-1}, C-O at ~1100 cm^{-1}, and the decrease of C=C bonds at ~1671 cm^{-1} in the differential spectra (Figure 3.16) is consistent with Br_2 addition reaction and confirmed olefinic functionalities in the MFP residue.

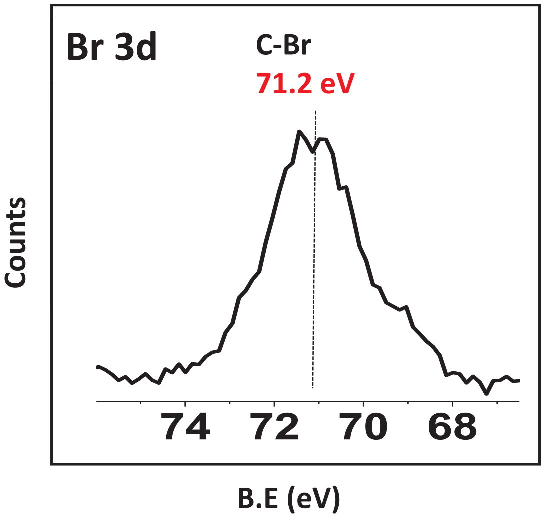

Figure 3.17 Formation of new C-Br bond after Br_2 addition reaction supported by XPS analysis.

A pictorial representation of the model chemical bonding structure of the MFP residue is proposed as shown in Figure 3.18 (b). The proposed structure is based on the detail assignments of specific vibrational modes to the observed IR absorption bands, Figure 3.18 (a), also verified by functional group specific chemical reactions discussed earlier. The model bonding structure depicts that the MFP residue consists of lower molecular weight (oligomeric) fluorocarbon configuration with substantial cross-linking (CF) and branching (CF, CF_3) within the CF_2 chain. Other functional groups include unsaturations like fluorinated alkenes (mostly internal) and carbonyls.

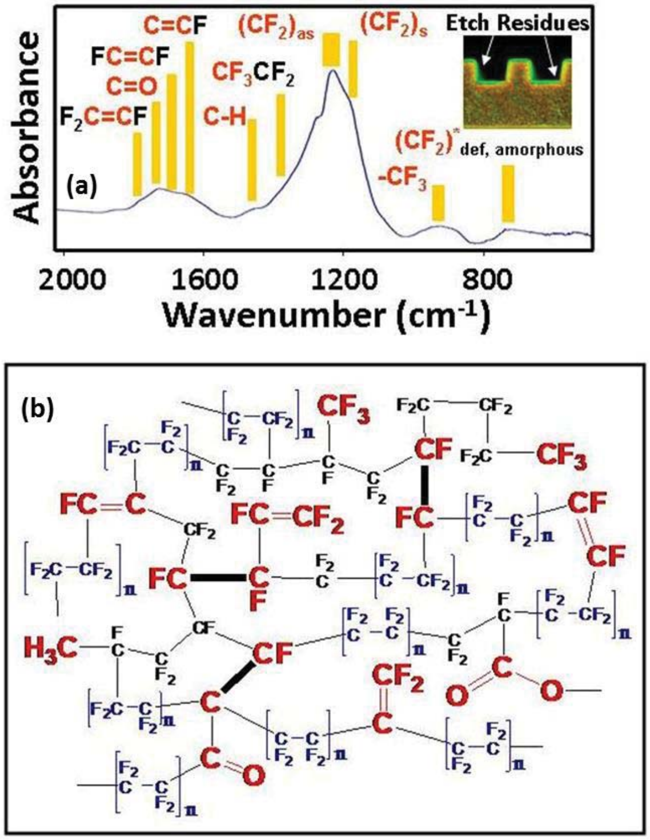

Figure 3.18 FT-IR spectrum of (a) 28 nm fluorocarbon polymer residue on 90 nm CDO trench line (SEM image, inset right) and (b) the proposed model structure of FC polymer.

3.3.4 Effect of plasma chemistry on etch residues profile

Plasma composition plays a vital role in modifying etch polymer structure during fluorocarbon based plasma etching process. To study the effect of plasma chemistry in modifying fluorocarbon polymer, additive gases like O_2 and NF_3 was added to the main feedstock gas plasma

(CHF_3/C_4F_8). Fluorocarbon based feed gas mix for plasma etching dissociates into reactive species such as CF_x (x= 1-3) and F radicals in the plasma. CF_x radicals combine to deposit fluorocarbon polymer whereas F radicals are the efficient etchants for dielectrics etching. Since CF_x radicals are responsible for polymer growth, controlling the concentration of radicals in the plasma can alter bonding structure and functionalities [32].

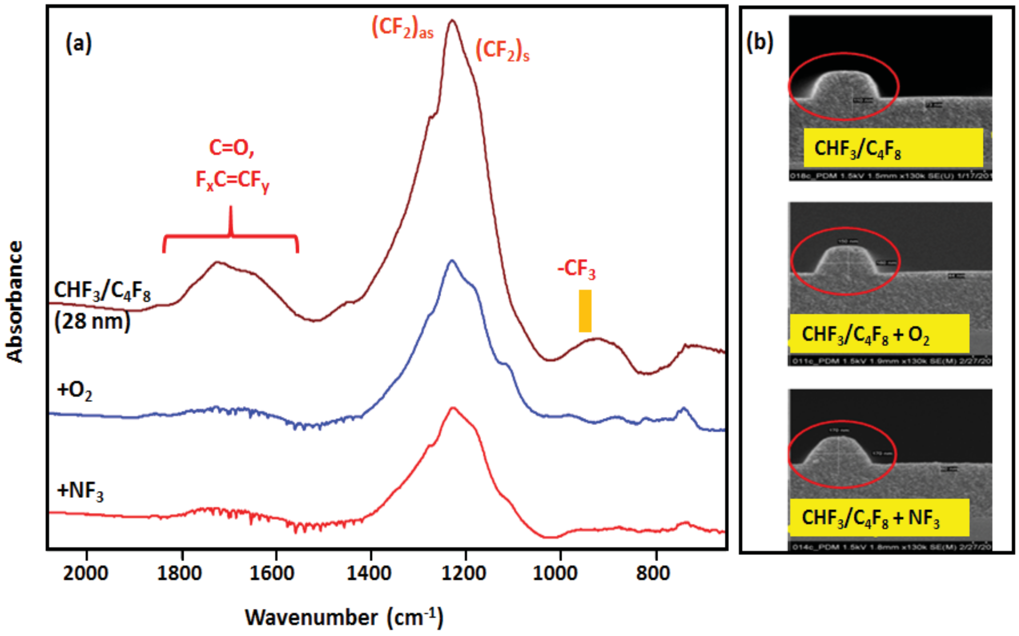

Figure 3.19 FT-IR spectra of MFP deposited during (a) CHF_3/C_4F_8 (original recipe), +O_2 and +NF_3 plasma etching on 90 nm CDO trench line, and (b) Corresponding SEM images.

Figure 3.19a compares IR spectra of MFP films deposited by original plasma recipe (CHF_3/C_4F_8/Ar) only and with additive gases such as O_2 and NF_3 to the original feedstock respectively. IR spectra reveal the reduction in all major absorption band intensities (CF_2, CF_3, $F_xC=CF_y$, C=O) and significant change in etch profile when additive gases (O_2 and NF_3) were added to the original plasma recipe that were optimized to deposit 28 nm fluoropolymer. SEM images in Figure 3.19b show that the MFP residue coating profile on low-*k* dielectric lines were altered significantly by the additive gases. The dielectric pillars show slightly tapered topography compared to the original structure, Figure 3.19b, indicating there is more etching involved (increase in F atoms). Addition of oxidants like O_2 aids in burning (decomposition) of CF_x (x= 1-3) fragments either in the gas phase or on the surface and thus increasing F atom density thereby increasing F/C ratio [33]; for example,

$$CF_3 + O \rightarrow COF_2 + \mathbf{F}$$

The F/C ratio at the substrate is an important process parameter, because it controls the isotropic or anisotropic nature of etching. A high F/C ratio can lead to isotropic etching, whereas a low F/C can lead to film deposition. The intermediate ratio where inhibitor film (MFP film) can be deposited on sidewalls and bottom is the basis for anisotropic ion enhanced inhibitor etching and is preferred for etch profile control [33]. Addition of NF_3 also directly increases F radical density in the plasma via homolytic bond cleavage, thus increasing F/C ratio [34]. XPS analyses (data not shown) also supports higher F/C content in $+O_2$ and $+NF_3$ plasma compared to CHF_3/C_4F_8 plasma deposited fluoropolymer. F/C calculated were 0.76, 0.81 and 0.82 for CHF_3/C_4F_8, $+O_2$ and $+NF_3$ respectively, indicating fewer CF_x fragments but higher F radicals. IR spectra (Figure 3.19a) shows a substantial reduction (~50%) of polymer deposition as indicated by the CF_2 absorption band and a major reduction (~80%) of C=O and $F_xC=CF_y$ (olefins) functionalities from the resulting F rich plasma environment ($+O_2$ and $+NF_3$ additives). Both observations are resulted from the extinction of CF_x fragments (higher F/C ratio) in the plasma. Since $F_xC=CF_y$ bonds (olefins) are formed via radical coupling on the fluoropolymer chain, a substantial decrease in the IR region 1600 – 1850 cm^{-1} for fluorinated olefins corroborates well with fewer CF_x radicals in the plasma environment. Moreover, a huge decrease in C=O peak intensity at 1710 cm^{-1} after O_2 addition to the plasma (Figure 3.19), confirms that additional O_2 did not contribute to C=O formation in the fluorocarbon polymer.

A more clear observation can be obtained from the plot of IR intensity vs. functional groups and the chemical structural change caused by the addition of O_2 and NF_3 to the original plasma feedstock, Figure 3.20. All chemical functionalities show reduction in the IR peak intensities caused by the added gases. Addition of NF_3 resulted in slightly more peak reduction compared to $+O_2$, most likely because NF_3 creates more etchants (F radicals) in the system (more tapered pillars also observed in SEM image).

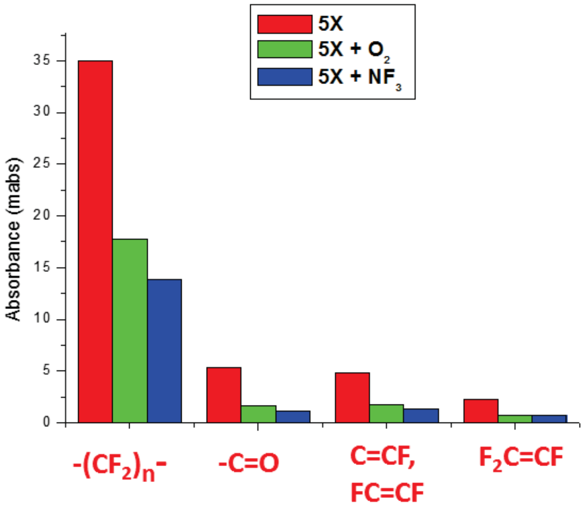

Figure 3.20 IR plot showing the effect of O_2 and NF_3 additives on the chemical bonding structure of the original structure (5x MFP ≈ 28 nm).

3.3.5 Effect of post-etch residues cleaning

The cleaning of post-etch residues from deep trench sidewalls and bottom has posed serious challenges with technology nodes below 22 nm and demands more complex and stringent requirements. The key prerequisite for a wet chemistry is to achieve efficient removal of post-etch residues without degrading the properties of underlying porous low-*k* stack. Current metrology tools for characterization of chemical structure and its removal efficiency by wet cleans are however lacking for sidewall polymer residues [35]. More importantly, the damage to low-*k* materials associated with wet cleans also needs to be monitored to effectively preserve its integrity.

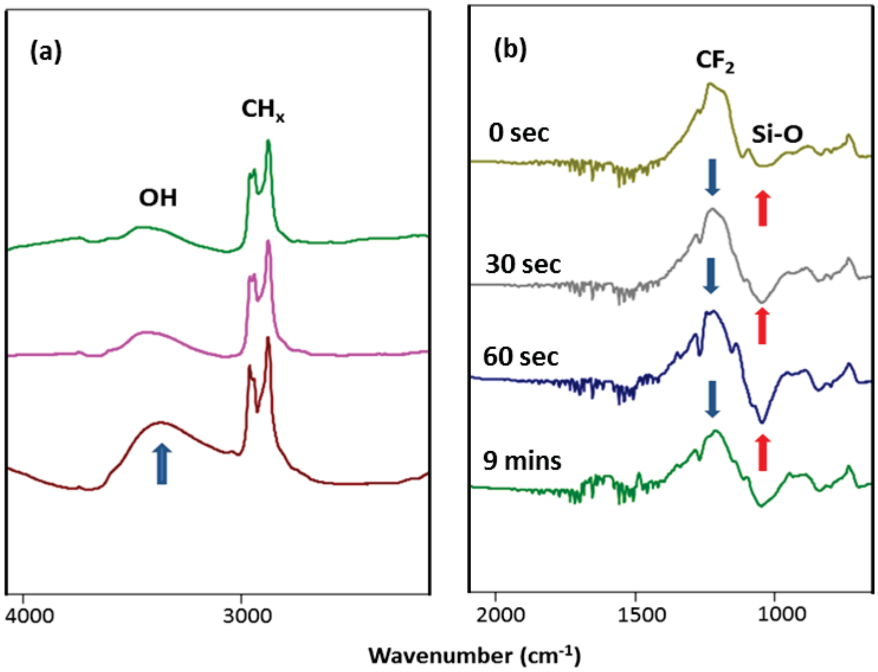

Figure 3.21 FT-IR spectra of FC polymer removal (cleaning) by commercial cleaning solvent.

In our study, MIR-IR and T-IR were employed as an efficient monitoring tool for residues removal and identification of low-*k* damage. Figure 3.21b shows T-IR spectra of a 1x polymer with time dependent TMAH based wet cleaning. The IR absorption peak centered at ~ 1235 cm^{-1} and 1180 cm^{-1} for C-F stretching of the CF_2 backbone shows a small decrease in peak height with cleaning time. However the cleaning efficiency was not substantial to remove majority of the fluorocarbon residues. The T-IR spectrum after 60 sec of clean shows a removal of only ~ 19% when compared to no clean (0 sec) spectrum. The complete removal of fluorocarbon residues was not achieved even after 9 mins of cleaning (data not shown) which strongly suggests insufficient cleaning nature of the chemistry used. The IR data also shows an increasing negative absorbance at ~ 1080 cm^{-1} which is assigned to Si-O-Si framework suggesting additional dielectric etching caused by post-etch cleans. Additionally, MIR-IR spectra (Figure 3.21a) reveals water sensitivity (Si-OH) starting as early as 30 sec of the clean treatment and monitors increasing trend as time progresses. MIR-IR data clearly indicates the removal of polymeric residues by undercutting the dielectric material and not by chemical attack by high pH TMAH based cleaning solution.

XPS analysis gave further insight into the inefficient removal of fluorocarbon residues. Figure 3.22 shows the C 1s spectra for the polymeric residues remained after 30 sec and 60 sec clean treatment. The intensity at 291.2 eV for CF_2 shows a slight decrease only as compared to no clean C 1s spectra, suggesting majority of the polymer still remained on the sidewalls. This data showed a good correlation with IR, however the critical low-*k* damage information was not possible from XPS.

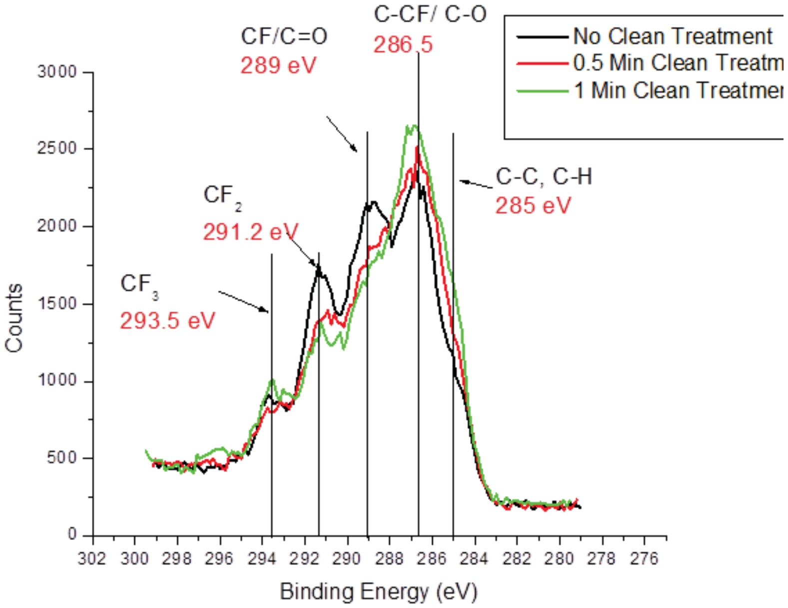

Figure 3.22 XPS spectra of FC polymer removal (cleaning) by commercial cleaning solvent.

3.4 Summary

Characterization of model fluorocarbon polymer deposited on low-*k* narrow trench patterns enabled by precise background cancellation revealed presence of fluorinated alkene and carbonyl functionalities embedded on fluorocarbon (CF_2) chain. A chemical bonding structure model of the fluorocarbon film was proposed after each functional groups were confirmed by specific derivatization reactions, supported by FT-IR and XPS. A chemical bonding structure and the topography of the polymer was altered by changing plasma chemistry (adding O_2 and NF_3). The ability to manipulate chemical functionalities of the residues by different plasma chemistries can guide to formulating more efficient (polymer removal) and effective (dielectrics compatible) post-etch clean that targets specific functional groups, such as the alkenes for electrophilic reagents. A proprietary alkaline based wet clean solution was also studied for residues removal from patterned structures which caused degradation of underlying low-*k* layer by aggressive TMAH chemistry.

3.5 References

1. Moore, G. *Electronics*. **1965**, 38.
2. Shamiryan, D.; Paraschiv, V.; Boullart, W.; Baklanov, M. R. *High Energy Chemistry*. **2009**, 43, 3.
3. Dang, R.; Shigyo, N. *IEEE Electron Device Letters*. **1981**, EDL-2, 196.
4. Bohr, M. T. *Solid State Technol*. **1996**, 39, 105.
5. Standaert, T. E. F. M.; Matsuo, P. J.; Allen, S. D.; Oehrlein, G. S.; Dalton, T. J. *J. Vac. Sci. Technol. A.* **1999**, 17, 741.
6. Hu, C. K.; Harper, J. M. E. *Materials Chemistry and Physics*. **1998**, 52, 5.
7. Manos, D.; Flamm, D. *An Introduction to Plasma Etching*; Academic Press: San Diego, Ca.

8. Hynes, A.; Shenton, M.; Badyal, J. *Macromolecules.* **1996**, 29, 18.
9. Schaepkens, M.; Oehrlein, G. S. *J. Electrochem. Soc*. **2001**, 148, C211.
10. Jaso, M.; Oehrlein, G. *J. Vac. Sci. Technol. A*. **1988**, 6, 1397.
11. Potter, G.; Morrison, G.; Charvat, P.; Ruoff, A. *J. Vac. Sci. Technol. B*. **1992**, 10, 2398.
12. Bailley, F.; David, T.; Chevollea, T.; Darnon, M.; Posseme, N.; Bouyssou, R.; Ducote, J.; Joubert, O.; Cardinaud, C. Roughening of porous SiCOH materials in fluorocarbon plasmas, *J. Appl. Phys*. **2010**, 108, 014906.
13. Ling, L.; Hua, X.; Zheng, L.; Oehrlein, G. S.; Hudson, E. A.; Jiang, P. *J. Vac. Sci. Technol. B*. **2008**, 26, 11.
14. Le, Q. T.; Claes, M.; Conrad, T.; Kesters, E.; Lux, M.; Vereecke, G. *Microelectron. Eng*. **2009**, 86, 181.
15. Maex, K.; Baklanov, M. R.; Shamiryan, D.; Iacopi, F.; Brongersma, S. H.; Yanovitskaya, Z. S. *J. Appl. Phys*. **2003**, 93, 8793.
16. Le, Q. T.; Keldermans, J.; Chiodarelli, N.; Kesters, E.; Lux, M.; Claes, M.; Vereecke, G. *Jpn. J. Appl. Phys.* **2008**, 47, 6870.
17. Claes, M.; Le, Q. T.; Kesters, E.; Lux, M.; Urionabarrenetxea, A.; Vereecke, G.; Mertens, P. W, *ECS Trans*. **2007**, **11**, 177.
18. Le, Q. T.; Chiodarelli, N.; Blum, I.; Kesters, E.; Lux, M.; Claes, M.; Vereecke, G.; Mertens, P. W. *Sematech Surface Preparation and Cleaning Conference*. **2007**.
19. Le, Q. T.; de Marneffe, J. -F.; Conard, T.; Vaesen, I.; Struyf, H.; Vereecke, G. *J. Electrochem. Soc*. **2012**, 159, H208.
20. Liang, Z.; Chen, W.; Liu, J.; Wang, S.; Zhou, Z.; Li, W.; Sun, G.; Xin, Q. *Journal of Membrane Science*. **2004**, 233, 39.

21. Gruger, A.; Regis, A.; Schmatko, T.; Colomban, P. *Vibrational Spectroscopy*. **2001**, 26, 215.
22. Colthup, N. B.; Daley, L. H. *Introduction to Infrared and Raman Spectroscopy*. 3rd ed., Academic Press: San Diego, **1990**.
23. Liang, C. Y.; Krimm, S. *J. Chem. Phys.* **1956**, 25, 563.
24. Wright, A.; Burgess, W. R.; William, R.; Wilkus, E. V. *US 3787382*.**1974**.
25. Moynihan, R. E. *Molecular Structure of Perfluorocarbon Polymers*. **1959**, 81, 1045.
26. Huang, K. P.; Lin, P.; Shih, H. C. *J. Appl. Phys.* **2004**, 96, 354.
27. Timmons, C. L. Fluorocarbon Post-etch Residue Removal using Radical Anion Chemistry. Ph.D. Thesis, Georgia Institute of Technology, November **2004**.
28. Ha, K.; McClain, S.; Suib, S. L.; Garton, A. *J. Adhesion*. **1991**, 33, 169.
29. Costello, C.; McCarthy, T. *Macromolecules*. **1987**, 20, 2819.
30. Hill, G.; Holman, J. *Chemistry in Context*. **2000**, 4.
31. Jones, L. A.; Holmes, J. C.; Seligman, R. B. *Analytical Chemistry*, **1956**, 28 (2), 191.
32. Rossnagel, S. M.; Cuomo, J. J.; Westwood, W. D. *Handbook of Plasma Processing Technology*; Noyes Publications: New York, **1990**.
33. Lieberman, M. A.; Lichtengerg, A. J. *Principles of Plasma Discharges and Materials Processing*. **2005**.
34. Tasaka, A.; Watanabe, E.; Kai, T.; Shimizu, W.; Kanatani, T.; Inaba, M.; Tojo, T.; Tanaka, M.; Abe, T.; Ogumi, Z. *J. Vac. Sci. Technol. A.* **2007**, 25, 391.
35. Baklanov, M. R.; Ho, P. S.; Zschech, E. *Advanced Interconnects for ULSI Technology*; John Wiley & Sons: **2012**.

CHAPTER 4

QUANTITATIVE EVALUATION OF PLASMA DAMAGE TO POROUS LOW-*K* DIELECTRIC TRENCH NANOSTRUCTURES USING MIR-IR[†]

4.1 Introduction

As predicted by Moore's law in 1965, the number of transistors incorporated on an integrated circuit increased exponentially, doubling approximately every two years [1]. The semiconductor industry is primarily focused on improvements related to performance of the transistors and reduce cost through scaling of devices. With the current scaling of devices beyond 22 nm technology node, the process complexity worsens even further. Hence it is important that the processes involved herein are carefully monitored and controlled for successful development.

The main technological challenge is centered on the integration of fragile porous low-*k* dielectric materilas ($k \leq 2.5$) to minimize RC time delay in the next generation Cu interconnect nanostructure. To decrease the dielectric constant (*k*), the porosity of organosilicate glass (OSG) is varied through the replacement of more polar Si-O with low polar Si-C bonds and/or reduce their density by means of introducing porosity [2]. The methyl group (CH_3) insertion into the Si-O-Si matrix causes it to lose its thermomechanical strength, making it more prone to wet/dry etch damages. To achieve the high aspect ratio dielectric trench pattern, plasma processing is widely used in the IC fabrication process such as etching, deposition, photoresist (PR) stripping, cleaning of surfaces and many others. At the same time plasma environment can be very harmful especially to mechanically fragile low-*k* materials because of the presence of energetic ions, reactive radicals,

---

[†] This chapter is presented in its entirety from S. Rimal, T. Mukherjee, J. Abdelghani, A. Goswami, O. Chyan, J. Stillahn, Y. Chiba, and K. Maekawa, "Evaluation of Plasma Damage to Low-*k* Dielectric Trench Structures by Multiple Internal Reflection Infrared Spectroscopy," *ECS Solid State Lett.*, **2014**, 3, N1 with permission from The Electrochemical Society.

electrons and vacuum ultraviolet (VUV) light. These species have shown to break Si-CH_3 bonds and form Si-OH (silanol) bonds on the top layer of organosilicate (SiOCH) glass low-*k* materials [3]. The associated adverse effects on the porous low-*k* materials include demethylation, moisture uptake, decrease in porosity and eventually degradation of mechanical and electrical properties [2-7]. Increase in water uptake ($k \approx 80$) drasticially raises the overall dielectric constant of interlayer dielectric to increase RC delay, leakage current and total power consumption making a device futile [8-11]. Hence, plasma-induced damages, especailly in the deep sidewall region (line and via), is the main cause of the dielectric reliability loss in low-*k* materials and pose challenges during the back-end-of-line (BEOL) Cu/low-*k* integration [12-13] .

Besides the challenges of handling weak porous low-*k* materials, a lack of sensitive metrology to guide through the development of plasma treatments at various fabrication steps is a major hindrance. There are a number of analytical techniques available to characterize plasma-induced low-*k* damages for unpatterned structures. The depth of carbon depletion can be evaluated using X-ray photoelectron spectroscopy (XPS) and Time-of-flight secondary ions mass spectroscopy (TOF-SIMS), but are techniques based on ion-bombardment (causes densification) [14] and is destructive. Electron beam-based metrology techniques such as Auger, SEM and TEM also have the potential to damage low-*k* films and are time consuming (especially TEM) [2, 14]. Spectroscopic ellipsometry is another technique commonly used to characterize plasma damage of unpatterned films based on the refractive index of the damaged film. This technique is however less accurate [14].

In comparison, characterization of dielectric damages from a deep trench sidewall nanostructure is much more challenging than blanket wafer due to its inherent geometry and limited accessibility. In addition, the results obtained from the unpatterned film studies may not be directly applicable to patterned structures because of the presence of patterned structures that can perturb the local plasma density [15-16]. Currently, only few techniques reported on for sidewall detection are glancing angle XPS, electron energy loss spectroscopy (EELS) and energy filter TEM (EFTEM). EFTEM has been the most powerful technique for plasma damage even in narrow structures [17]. This tool can map the elements by filtering electrons of certain energy, hence visualizes carbon depletion with nanometer resolution. Although a successful technique, it is destructive and requires laborious sample preparation [14]. Electrical characterization (e.g. reliability and leakage current measurements) can be utilized to reveal dielectric degradation, but are only applicable to fully processed interconnects, however are costly and cannot pinpoint any particular process causing the damage [2]. Thus, there is a pressing need for a convenient metrology to identify and quantify the damage on the side walls of dielectric trench structures from plasma processing such as photoresist stripping.

In this study, we utilized multiple internal reflection infrared spectroscopy (MIR-IR) to monitor water adsorption, carbon stripping and post-etch residues during the formation of trench structures in low-*k* dielectric materials via plasma etch and strip processes. Fourier transform infrared spectroscopy (FT-IR), a fast and non-contact metrology, can provide direct observation of water adsorption and the chemical bonding structure of blanket porous low-*k* dielectric materials. Recently, applications of FT-IR to characterize patterned dielectric wafer were reported [18-20]. MIR-IR spectroscopy can increase detection sensitivity up to 100-fold compared with conventional FT-IR because the wafer itself serves as an IR waveguide allowing for multiple detections [21-22], Figure 4.1. In this work, a test pattern of ~68 nm trenches with 128 nm pitch was created through oxide hard mask plasma etching followed by organic residue stripping. Damage to the dielectric in terms of silanol formation was quantified and correlated to each plasma processing step using MIR-IR complemented by X-ray photoelectron spectroscopy (XPS) and scanning electron microscopy (SEM).

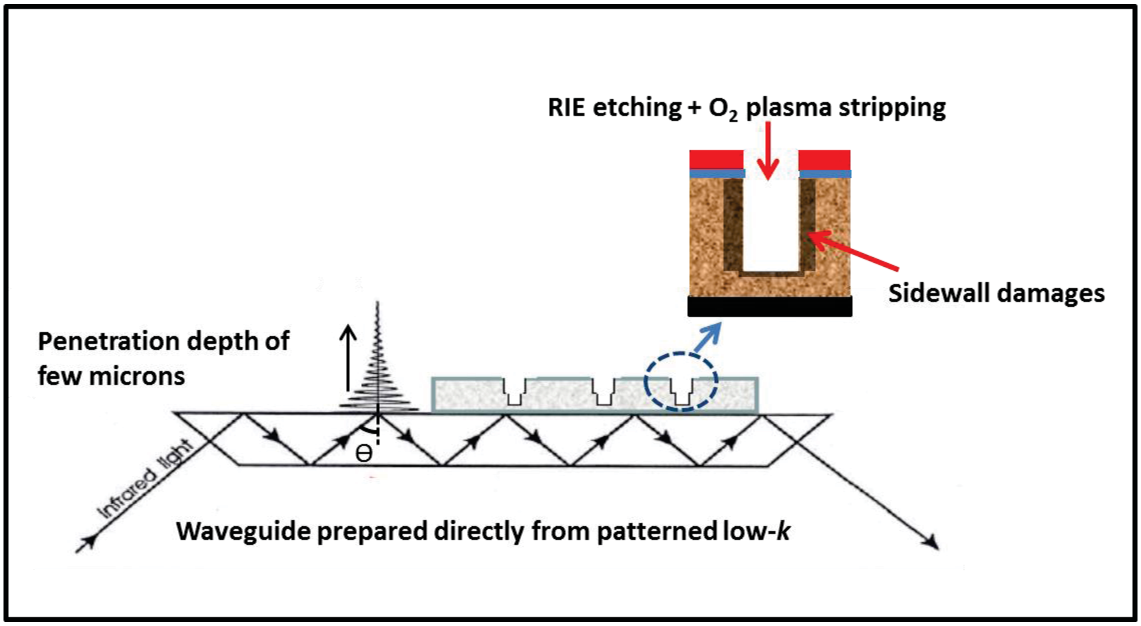

Figure 4.1 Schematic of MIR-IR for patterned structure.

4.2 Experimental

Preparation of dielectric trench pattern

In this work, a line-space pattern was transferred through an oxide hard mask (~50 nm) onto a porous SiOCH low-*k* (~350 nm) dielectric material (*k* ~2.55 nominal, ~14% porosity, d < 2 nm) in a dual-frequency capacitively coupled plasma etch reactor. The trench structures were approximately 68 nm wide and 150 nm deep with pitch ca. 128 nm. The *k* value and pore size of the low-*k* films were measured by Hg probe and ellipsometric porosimetry respectively. Three different wafers were prepared and processed as 1) post-etch: trench structures generated by conventional fluorocarbon-based reactive ion etching (RIE); 2) post-strip: oxygen-based plasma chemistry optimized to remove etch residues and remaining organic photoresist stack; 3) post-strip

+ 60 sec over-etch, Figure 4.2. Finally, two different pristine blanket wafers with and without oxide hard mask were also prepared for the control study. Low-*k* blanket film with oxide hard mask was prepared by plasma etch back of photoresist stack.

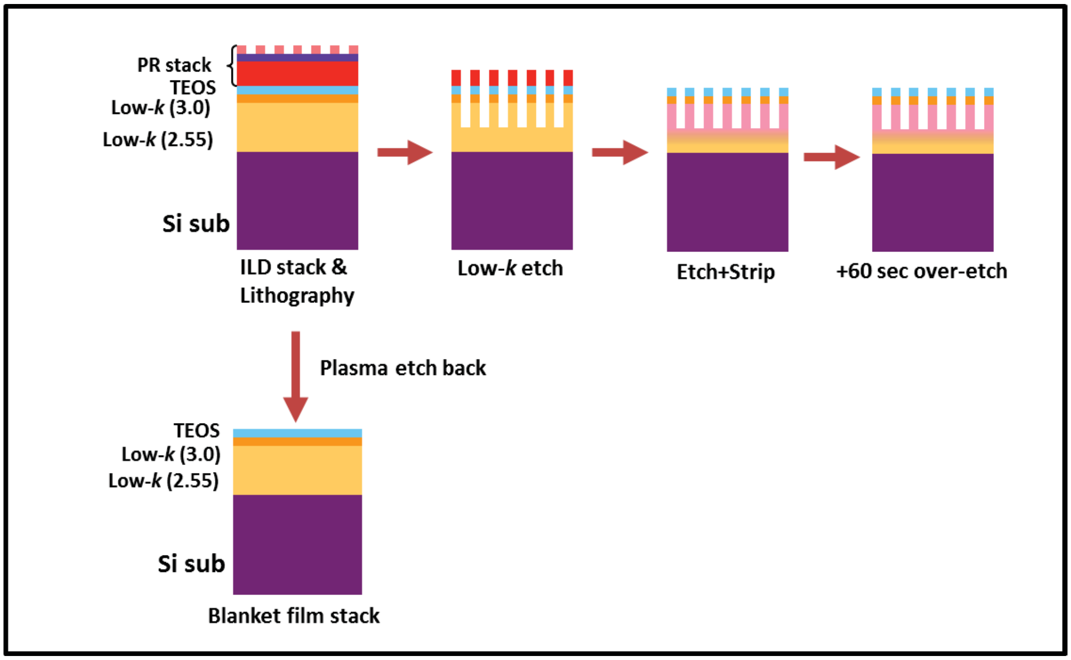

Figure 4.2 Sample preparation and stack structure.

Characterization

Trench patterned wafers were cut and fabricated into attenuated total reflectance (ATR) parallelograms (10 x 60 x 0.8 mm, 45° bevel angle) for MIR-IR characterization following previously described procedures [23-24]. Both MIR-IR and Transmission IR (T-IR) spectra were measured using a Nicolet iS50 FT-IR spectrometer under constant dry air ($CO_2 < 1$ ppm) purge. After 30 minutes purge, MIR-IR spectra of trench structures with clean bare silicon (SC1 cleaned + HF etched) substrates as background were collected at 4 cm^{-1} resolution as the average of 100 individual spectra using a vertical ATR accessory from Pike Technologies. XPS analyses were conducted using a PHI 5000 Versa Probe equipped with an Al K_α (1486.7 eV) radiation source and an electron flood gun to neutralize sample charging. HF decoration etch was carried out by dipping sample in a 0.49% HF solution for 30 sec (empirically determined by SEM to remove most of the damaged low-*k* layer) followed by 10 sec water rinse. MIR-IR and T-IR analysis also shows dHF treatment of ~30 sec removes most of the damaged low-*k* layer, Figure 4.3. Cross-sectional images were obtained with a Hitachi S-5500 FE-SEM. Blanket low-*k* film was etched in a Harrick Plasma PDC-001 Etcher. The pressure was maintained at 100 mtorr (O_2, H_2) at ~30 W power.

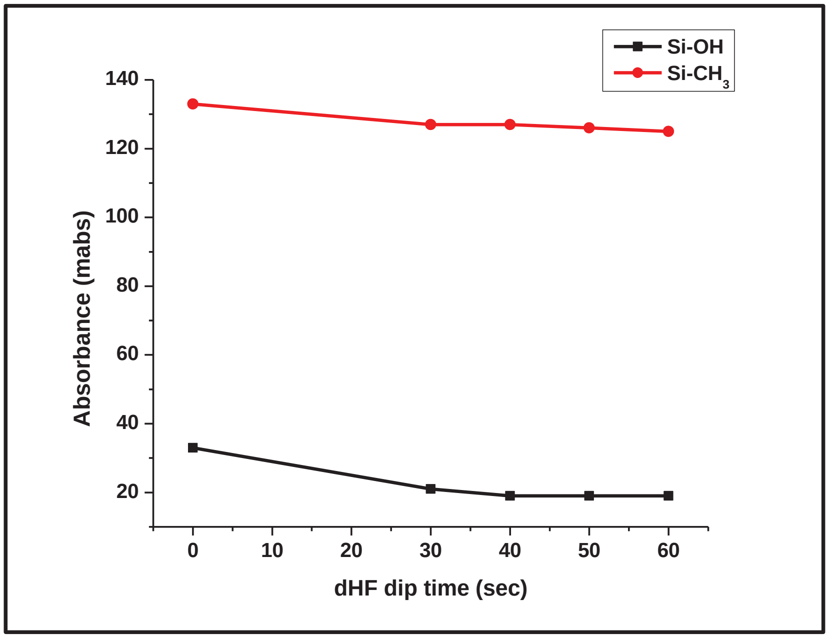

Figure 4.3 Plot showing Si-OH and $Si-CH_3$ removal on damaged sample with 100:1 dHF treatment.

Functional group specific chemical reactions

All chemicals were obtained as reagent grade from Sigma-Aldrich. For C=O identification: Wafer coupons were immersed in a 2,4-dinitrophenylhydrazine (DNPH) solution (0.06 gram

DNPH, 10 mL isopropyl alcohol and 150 μL of 12M HCl) and heated at 70°C for 16 hours. For CF_x identification: A Na/Naphthalenide etchant (Creative Engineers, Inc.) was used. FT-IR measurement was performed after wafer coupons were rinsed thoroughly with ample amount of ultrapure water (18.2 MΩ.cm, C content < 2 ppb) and isopropyl alcohol followed by N_2 blow dry.

4.3 Results and Discussion

4.3.1 Blanket low-*k* after O_2 and H_2 plasma etch

First, a study of plasma effect on blanket low-*k* film stack (no oxide hardmask) (~350 nm, *k* ~2.55) was carried out using both O_2 and H_2 gases. Figure 4.4a shows the MIR-IR spectra of low-*k* film exposed to O_2 plasma etching of increasing time duration. The pristine SiOCH film (t=0 sec) exhibits a dominant IR absorption peak at 2970 cm^{-1} originating mostly from the CH_3 asymmetric stretching of Si-CH_3 within the SiOCH framework. MIR-IR spectroscopy is found 20 times more sensitive in detecting these critical -CH_3 groups [178 milliabsorbance (mabs) CH_3 absorption peak intensity] compared to T-IR (9 mabs), Figure 4.4a. MIR-IR spectra also reveal other finer chemical bonding details such as the O-H, O-SiH_x, SiH_x, C=O, and C=C bonding of SiOCH thin films. The improved sensitivity of MIR-IR is made possible by favorable differences of refractive indices between Si wafer substrate and low-*k* film which enables multiple total internal reflections of IR probe beam within Si ATR crystal [25]. Each internal reflection sets up a standing wave pattern (evanescent wave) penetrating ~ < ¼ λ above the silicon surface to interact with low-*k* film. These multiple interactions and measurements allow MIR-IR to sensitively detect down to sub-monolayer hydrogen termination on silicon surface [24, 26].

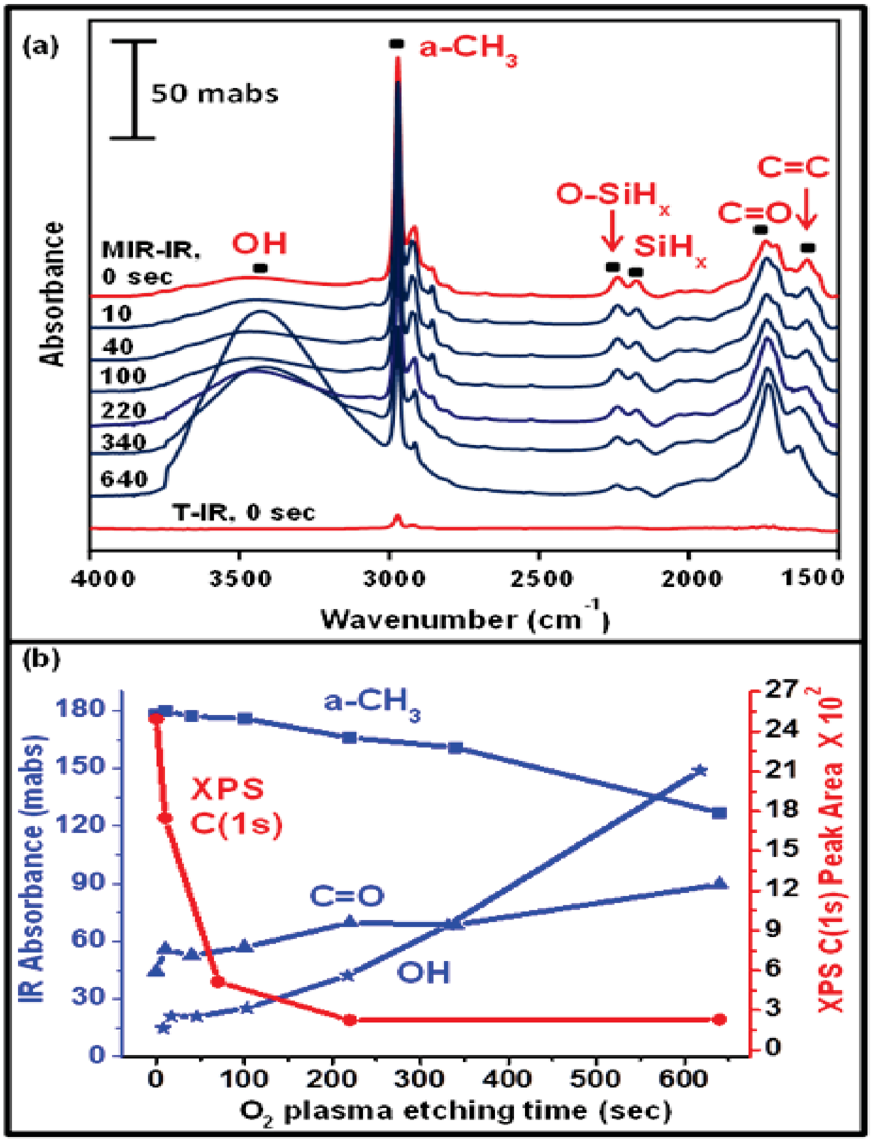

Figure 4.4 (a) MIR-IR spectra of a 350 nm blanket low-*k* film measured after O_2 plasma etching of 0-640 sec; a T-IR spectrum of pristine film is included for comparison. (b) Plots of IR absorption peak heights and XPS C (1s) of Si-CH_3 (283.4 eV) vs. etching time.

MIR-IR spectra (Figures 4.4a & 4.4b) show that increased O_2 plasma etch times correspond to a decreased CH_3 peak and a rapid increase of the O-H absorption peak in low-*k* film, changing the surface to hydrophilic. This result is also consistent with water contact angle measurements which indicate a decrease of contact angle after the plasma treatment with increasing time. Driven by thermodynamically favorable Si-O bond formation, O_2 plasma etching is known to extract weakly bonded methyl groups from Si-CH_3 and replace them with Si-OH groups. Terminal Si-OH groups (polar) with various structural configurations can readily adsorb moisture through hydrogen bonding [27]. Quantum chemistry calculations have demonstrated that the physisorbed H_2O molecule is the main cause of dielectric constant increase [28]. In addition, it is interesting to note the increase of C=O (~1720 cm^{-1}) and C=C (~1615 cm^{-1}) towards higher etching time, which can be attributed to the combination of oxygen from plasma with carbon from ILD material, and the polymerization of carbon radicals formed in the plasma respectively.

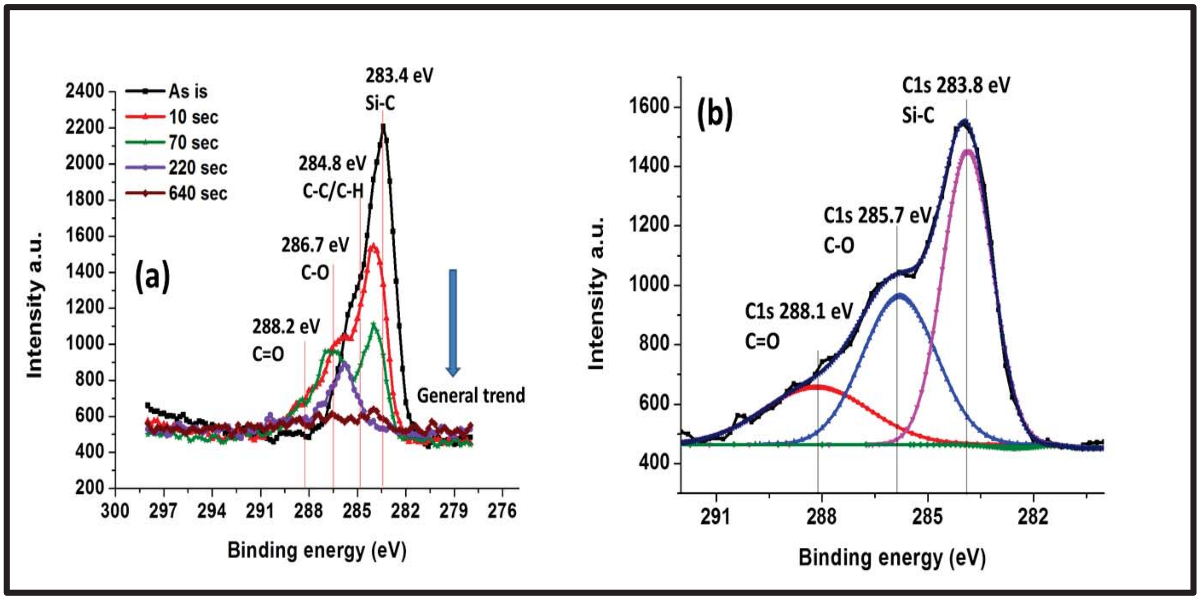

Figure 4.5 (a) XPS analysis of C (1s) peak of 350 nm blanket low-*k* with progressive O_2 plasma etching time (0-640 sec), (b) Deconvolution of overlapping C (1s) peak into three component peaks for 10 sec O_2 plasma etched low-*k* film.

In contrast to MIR-IR, XPS analyses of O_2 plasma treated low-*k* film cannot clearly resolve these changes, showing only broad overlapping C (1s) peaks that require peak fitting to extract C (1s) component of Si-CH_3 at 283.4 eV [29-30], Figure 4.5b. Figure 4.4b and 4.5a shows the trend of O_2 plasma induced carbon loss as detected by XPS measurements. After 220 sec of etching, only C (1s) signal near background level can be detected indicating the carbon depletion zone has moved beyond the probing depth of XPS (< 10 nm). On the other hand, MIR-IR with its higher probing depth (> 800 nm) can characterize both the O_2 plasma damaged surface region as well as the remaining bulk of low-*k* dielectric film. More importantly, the obtained IR absorption bands are better energy-resolved, thus giving detailed chemical bonding information necessary for rapid assessment of plasma process damages that could not otherwise be obtained.

H_2 plasma etching on blanket low-*k* stack with the same plasma processing parameters as for O_2 plasma etching shows only a subtle change in chemical bondings with etching time, Figure 4.6. Since hydrogen is generally less reactive than oxygen, it is expected that H_2 plasma imparts less damage to low-*k* materials (decrease of $-CH_3$ and increase of –OH bonds). However, when generated in CCP and ICP reactor chambers (at room temperature and in the presence of ions and VUV), H_2 plasma can have a detrimental effect on the low-*k* causing methyl depletion, densification and moisture uptake [2].

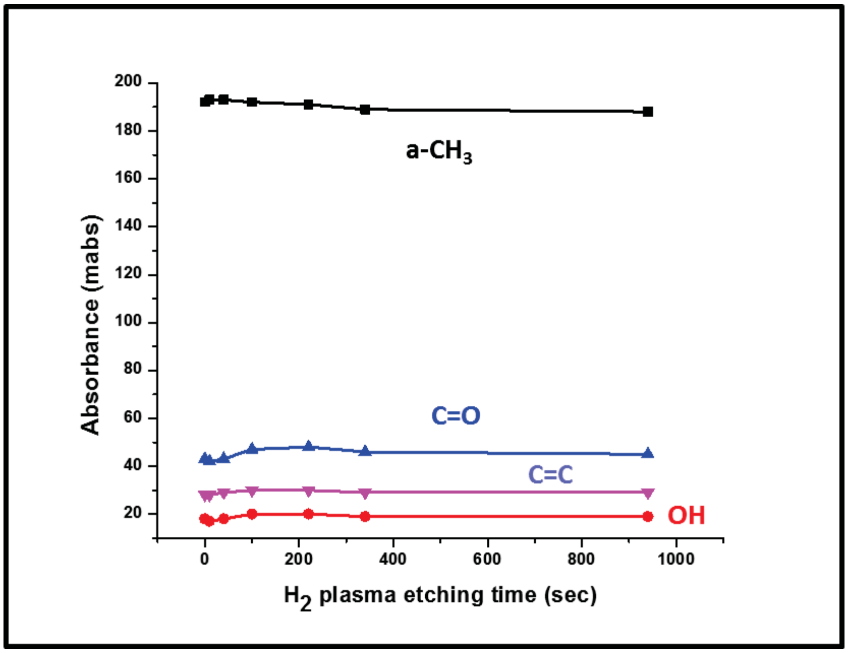

Figure 4.6 Plot of different functional group after H_2 plasma etching (0 – 940 sec), measured by MIR-IR.

4.3.2 Plasma damage on dielectric trench pattern

One of the major advantages MIR-IR provides is the capability to investigate 3-dimensional patterned surfaces such as the sidewalls of trenches. Figure 4.7a shows MIR-IR spectra of a test dielectric trench pattern (~68 nm wide, ~128 nm pitch) after an increasing number of plasma processing steps were performed. Measurements were taken as post-etch, post-strip, and 60 sec over-etch. MIR-IR shows steady increase in the broad O-H stretching band (3150 - 3850 cm^{-1}) after each successive plasma treatment. Fundamental stretching vibrations of OH groups are usually diverse, broad and overlapping mainly due to various structural states and degrees of intra- and intermolecular hydrogen bonds [27]. The IR absorption band centered at ~3430 cm^{-1} can be assigned to Si-OH stretching vibration of silanol groups in SiOCH low-*k* materials [31]. In Figure 4.7a, an additional 60 sec over-etch (43 mabs) in the post-strip (24 mabs) step causes an 80% increase of the Si-OH absorption peak height at 3430 cm^{-1}. This MIR-IR data suggests that the more aggressive plasma chemistry required to strip organic residues also tends to disrupt weaker $Si\text{-}CH_3$ bonds and some Si-O network and results in undesirable moisture-adsorbing silanol groups. Disproportional loss of $Si\text{-}CH_3$ IR absorption peak height (151 to 133 mabs) at 1276 cm^{-1}, Figure 4.7b, measured by T-IR also confirms excessive carbon loss after 60 sec over-etch.

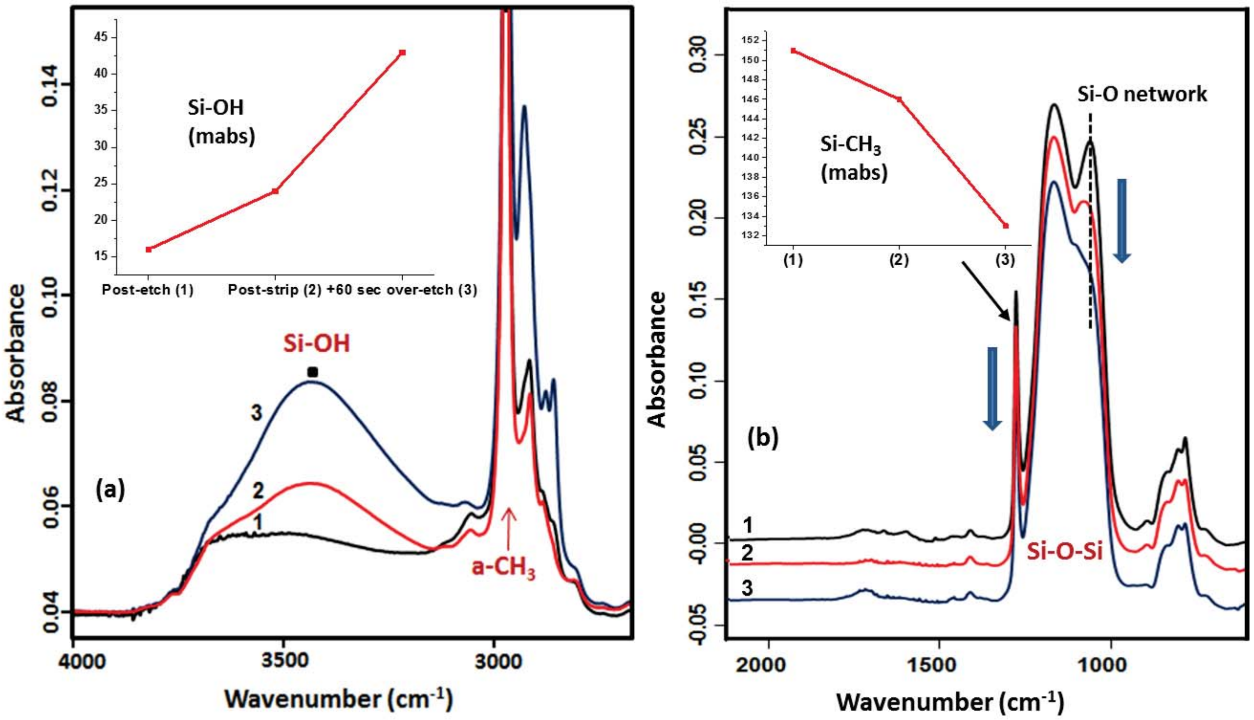

Figure 4.7 (a) MIR-IR spectra of (1) post-etch, (2) post-strip and (3) post-strip + 60 sec over-etch of low-*k* dielectric trench structures. (b) T-IR spectra of samples (1)-(3). Insets shows respective Si-OH increase and Si-CH$_3$ decrease.

4.3.3 Assessment of post-etch residues after post-etch step

Fluorocarbon-based RIE is commonly used to pattern the dielectric layer. During this process, reactive radicals can readily diffuse into the trench vertical sidewalls and cause significant dielectric damage. With proper adjustment of the polymerization rate (F/C ratio) in the plasma gas chemistry, a thin layer of fluorocarbon etch residues is deposited on the vertical sidewalls, which serves as a protective layer from ions impingement and radicals diffusion on the sidewalls. These post-etch residues must subsequently be removed during cleans step (dry/wet cleans) or else can cause reliability issue for further processing steps.

As shown in Figure 4.8 inset, the differential T-IR spectra, obtained by cancelling out the bulk absorbance of the low-*k* dielectric, provide useful insights into the chemical bonding transformation of post-etch residues caused by plasma processing. After post-etch, Figure 4.8 inset, a broad absorption band was observed in the 1530-1850 cm^{-1} region carrying multiple vibrational signatures. With functional group specific chemical derivatization, we identified that the multiple vibrational bands correlate to internal olefinic (C=C) bonding with various degrees of fluorination (-C=CF, -FC=CF- and F_2C=CF-) together with carbonyl (C=O) functionality [18]. With 60 sec over-etch, a significant increase of C=O functionality can be seen at ~1720 cm^{-1} indicating increased plasma induced damage. This result corroborates the large increase in the Si-OH vibration peak observed at 3430 cm^{-1} by MIR-IR after 60 sec over-etch, Figure 4.7a.

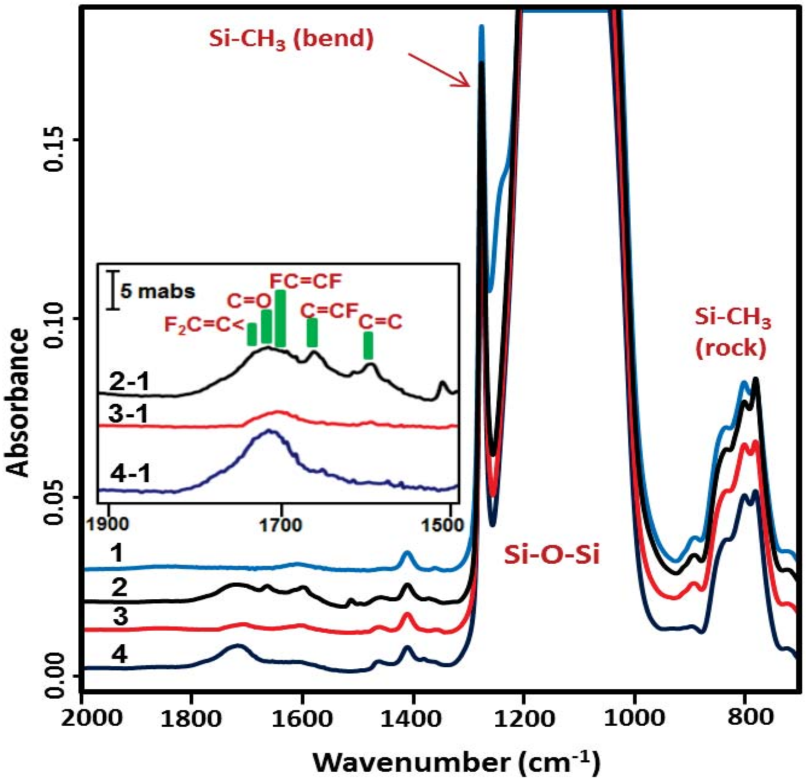

Figure 4.8 T-IR spectra of (1) pristine low-*k* blanket film, (2) post-etch, (3) post-strip and (4) post-strip + 60 sec over-etch of low-*k* dielectric trench structures. The inset shows differential T-IR spectra highlights the effects of plasma processing (2)-(4) on post-etch residue after cancelling out the bulk low-*k* absorption background (1).

Most of these post-etch residues however were removed by the subsequent stripping process except for a small residue peak observed at ~1710 cm^{-1}. XPS analyses also showed a low-level of F (1s) signal remained on post-strip trench structure, Figure 4.9. Figure 4.9 clearly shows a huge peak intensity at 688.8 eV assigned to fluorine bonded to carbon on post-etch. Interestingly, an additional +60 sec over-etch did not remove the remaining residual etch residues after post-strip. The F (1s) peak shift observed at 686.6 eV (Figure inset) in post-strip and over-etch samples could result from F ions diffusing into the low-*k* (bulk) and form a CF group linked to non-fluorinated carbon in a highly cross-linked network.

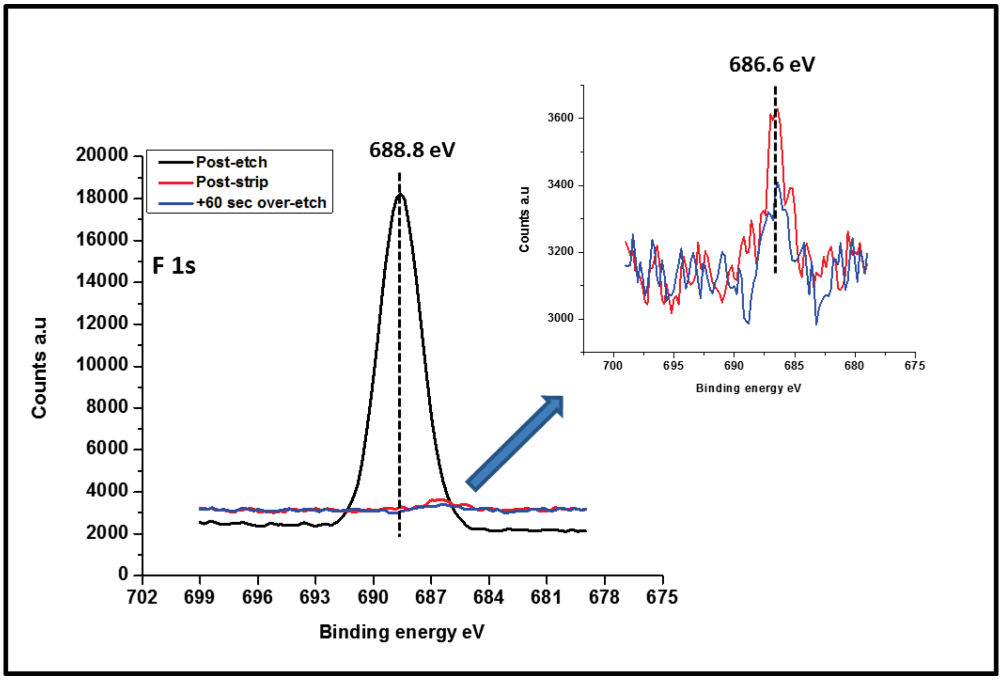

Figure 4.9 XPS analysis of F (1s) on post-etch, post-strip and +60 sec over etch samples.

To investigate further on the chemical bonding structure of post-etch residues, a functional group specific chemical reaction using Na-Napthalenide solution was performed on post-etch (highly fluorinated) sample. Na-Napthalenide solution contains highly energetic radical anions capable of breaking stronger carbon fluorine bond (C-F) and disintegrate the fluorocarbon matrix [32]. As shown in Figure 4.10, the increasing negative absorbance band at ~1235 cm^{-1} with increasing time of reductive etching, assigned to CF_2 asymmetric stretching can give an estimate of CF_2 groups in the residues. When fluorinated olefins lose C-F bond, corresponding decrease (negative bands) are expected in the differential spectra. Other functional group like carbonyl may also show negative absorption when fluorocarbon network is disintegrated or lose fluorine rich environment. The real post-etch residues composed mainly of fluorocarbon polymer consisting of about equal amount of saturated CF_2 bonds and unsaturated CF bonds (ratio ~ 1), Figure 4.10, which is different in bonding configuration than model fluorocarbon polymer (MFP) we have studied previously [18].

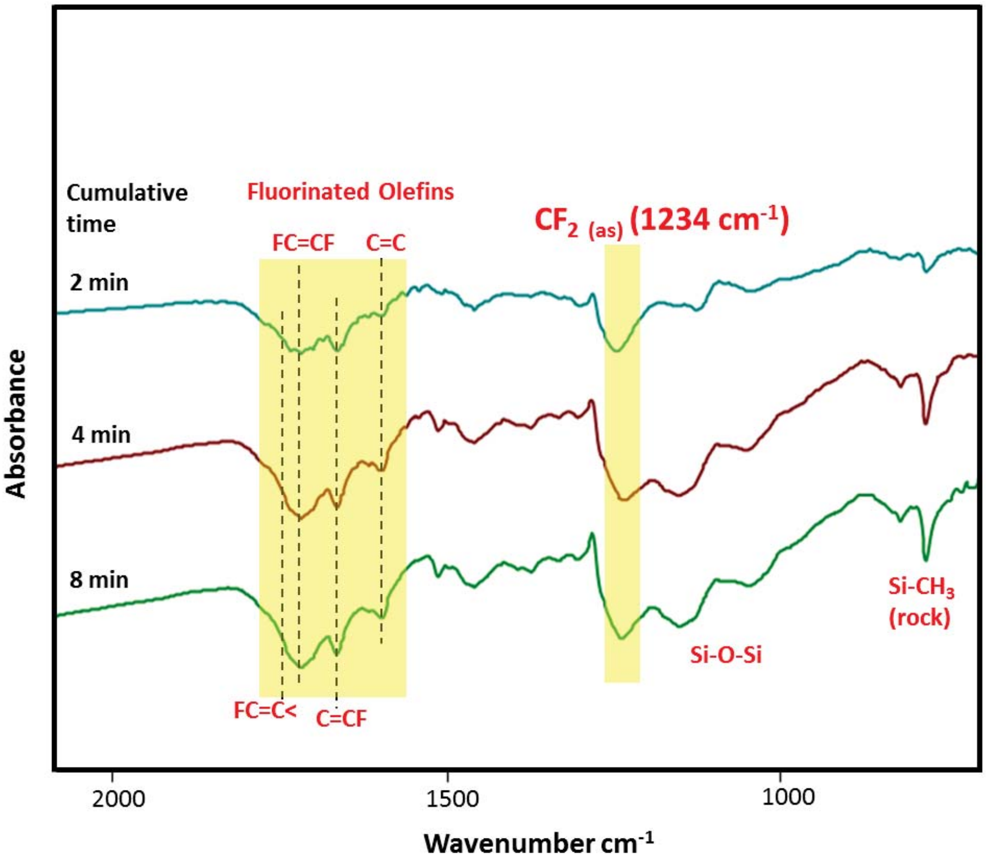

Figure 4.10 Time dependent differential spectra after reductive etching on post-etch.

4.3.4 Conformation of carbonyl functionality by DNPH derivatization on +60 sec over-etch

DNPH is expected to target carbonyl (C=O) functionality via NH_2 group, resulting in the formation of hydrazone adduct product. Removal of C=O group and the corresponding formation of new chemical bond of imine group (C=N) is expected. As shown in Figure 4.11, the differential spectra obtained after DNPH treatment shows negative band at ~ 1720 cm^{-1} corresponding to C=O functionality. The +60 sec over-etch sample shows higher C=O removal compared to post-etch sample, indicating higher C=O content in the former sample, which corroborates well with the data in Figure 4.8. The formation of C=N at ~ 1619 cm^{-1} and N-H at ~ 1596 cm^{-1} absorption bands (Figure 4.11) also correlates well after the reaction with DNPH.

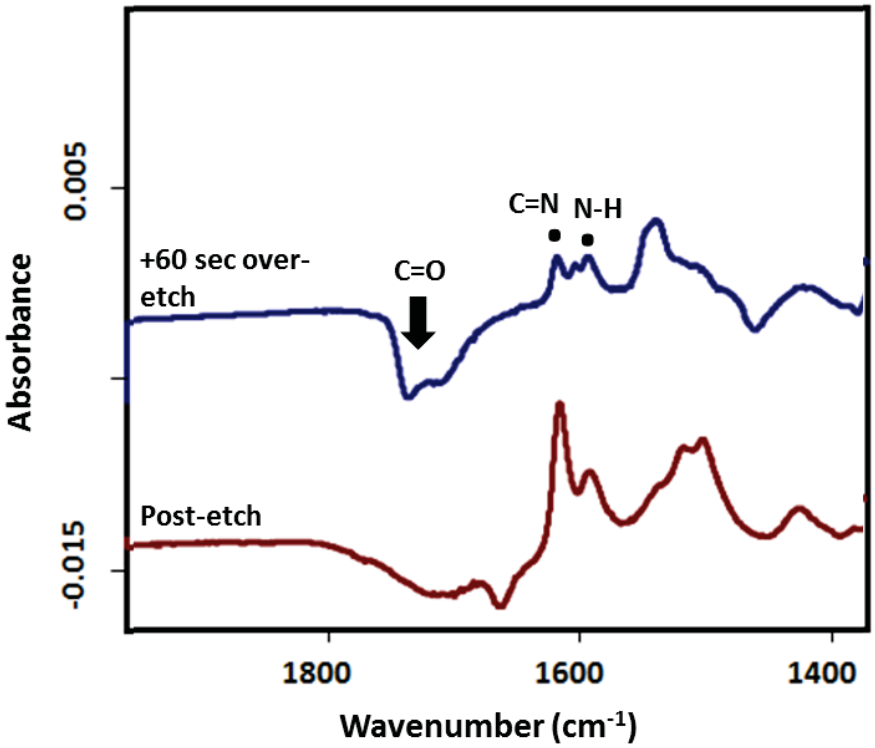

Figure 4.11 Differential FT-IR spectra (post DNPH treatment vs. before treatment) of +60 sec over-etch and post-etch after DNPH reaction.

4.3.5 Plasma damage assessment

The ultimate goal of a successful RIE pattern transfer is to meet all critical dimension requirements while retaining the dielectric properties of pristine film. To better assess plasma damage, trench patterns were compared to a pristine low-*k* blanket films using both MIR-IR and T-IR. As expected, un-etched pristine film had higher Si-CH_3 content (~198 mabs at 1276 cm^{-1}) than post-etch trench patterns (~151 mabs) since dielectric material is being removed to create the patterns. The obtained IR spectrum of pristine dielectric film was then normalized using Si-CH_3 content ratio (0.76 = 151/198), Figure 4.12, to yield a spectrum representative of an idealized dielectric trench pattern that has no plasma damage. It is worth noting that the Si-CH_3 signal ratio (0.76) based on T-IR analyses matches the ratio of dielectric volume of etched structure to that of blanket film before etch (~0.77) calculated from cross sectional SEM images (Figure not shown).

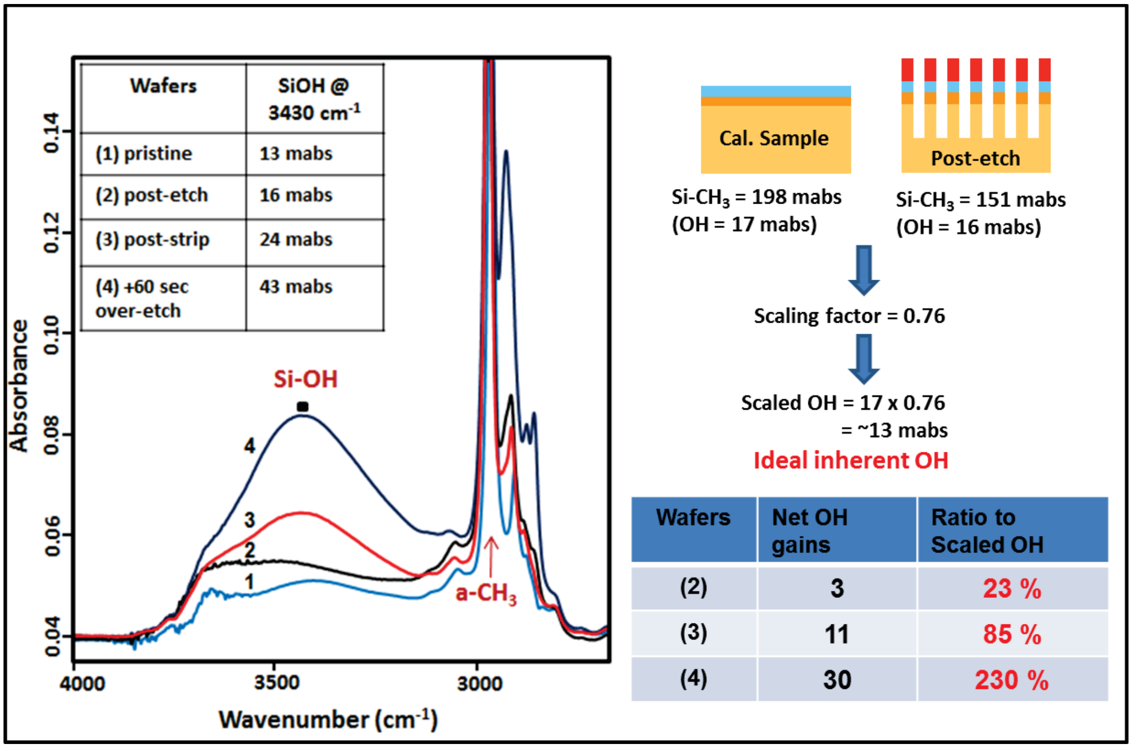

Wafers	SiOH @ 3430 cm^{-1}
(1) pristine	13 mabs
(2) post-etch	16 mabs
(3) post-strip	24 mabs
(4) +60 sec over-etch	43 mabs

Wafers	Net OH gains	Ratio to Scaled OH
(2)	3	23 %
(3)	11	85 %
(4)	30	230 %

Figure 4.12 MIR-IR spectra of (1) pristine low-*k* blanket film after normalized by 0.76 and (2) post-etch, (3) post-strip and (4) post-strip + 60 sec over-etch of low-*k* dielectric trench structures. Table on the right shows net OH gain by each plasma processes compared to ideal spectrum.

Since surface Si-OH groups directly affect water sensitivity, monitoring the change in Si-OH IR absorption can serve as a practical assessment of plasma induced damage. When compared to the scaled spectrum of the pristine film, post-etch, post-strip and 60 sec over-etch processes cause Si-OH peak height to increase by 23%, 85% and 230%, respectively, Figure 4.12. The MIR-IR analyses clearly indicate that more stringent process optimization is required at the plasma stripping step in order to avoid excessive damage. As such, the Si-OH content measured by MIR-IR can function as a sensitive and reliable (< 2.5% standard deviation) quantitative metric for the assessment of plasma induced damage, Figure 4.14.

4.3.6 MIR-IR vs. alternative method for patterned low-*k* damage assessment

The applicability of MIR-IR metrology in characterizing patterned trench structures was also corroborated by some currently used testing options. Because quantitative interpretation of angle-resolved XPS of deep trenches is difficult (requires special test structures), “HF decoration” etching was employed as an alternative testing method for evaluating plasma damage [14]. HF etch testing exploits the fact that the damaged dielectric film is preferentially etched because it is more hydrophilic. Although widely used as a quick method, the technique is unfortunately hampered by low sensitivity and limited reproducibility because it requires a right concentration of HF or else under-etch/over-etch can be an issue.

For this study, post-strip and +60 sec over-etched samples were tested by HF etching. As can be seen on the top row of Figure 4.13a, HF etch removed ~5 nm of the sidewall and ~6 nm of trench bottom from the post-strip sample. Because the +60 sec over-etched sample (Figure 4.13a, bottom row) has more plasma damage, we expect to find more removal by HF etching. HF etch removes 100% (~12 nm) more of the trench bottom but 200% (~15 nm) more low-*k* dielectrics from the mid-width. Surface densification at the trench bottom by RIE ion bombardment (vertical etching) is known to limit the extent of plasma damage. Hence most of the damage is from the isotropic reactive radicles diffusing into the porous trench sidewalls. The extent of damage is expected to increase with increasing porosity of low-*k* dielectric materials.

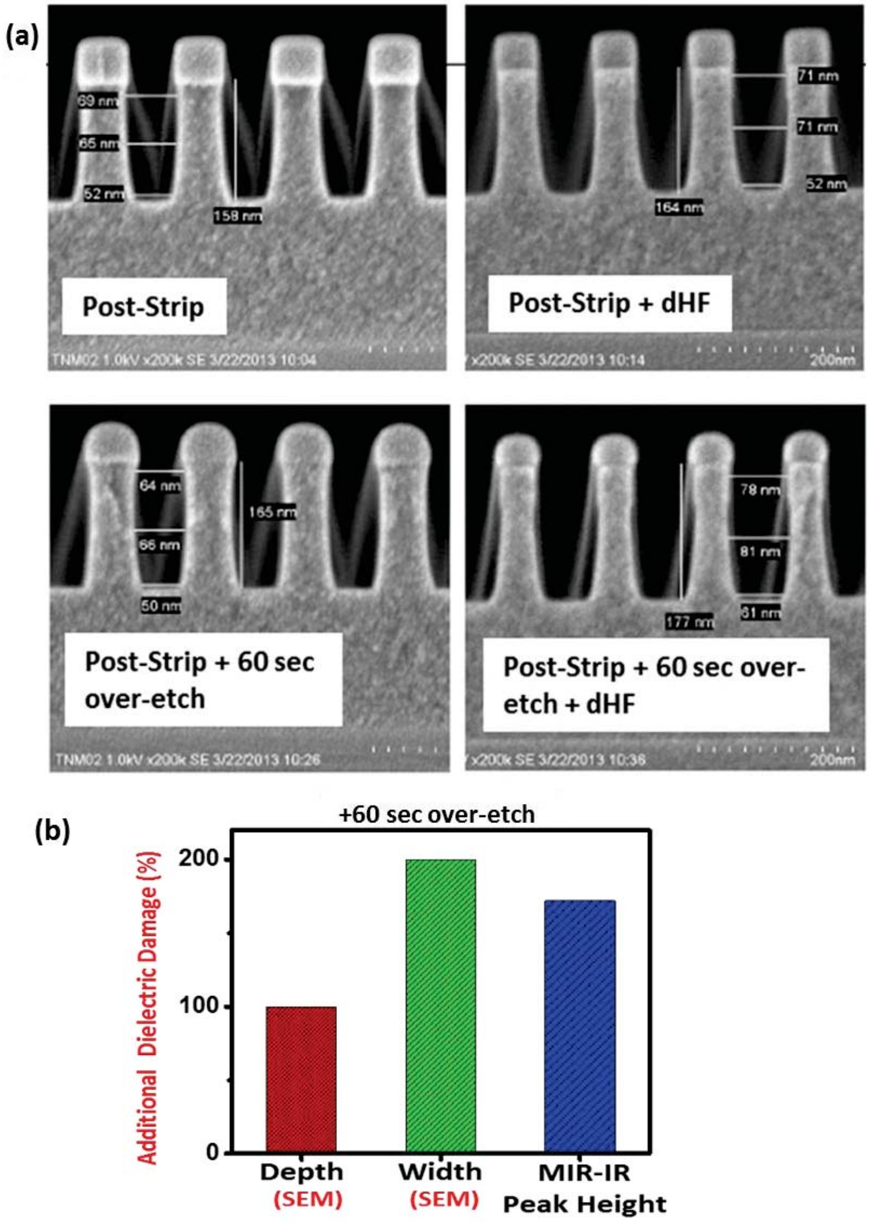

Figure 4.13 (a) Cross sectional SEM images of exact matching pair's trench structures before and after HF decoration etch. (b) Additional dielectric damage caused by +60 sec over-etch after post-strip was evaluated by SEM (vs. trench width and depth) and MIR-IR (vs. Si-OH peak height).

The post-etch ~68 nm trench structure has >80% of its exposed surface areas as sidewalls, see Figure 4.13a. With +60 sec over-etch, total additional dielectric damage assessed by SEM after HF etch is ~180% (80% of 200 + 20% of 100), Figure 4.13b, which is the weighted average of trench sidewalls and bottom. Additional damage on +60 sec over-etched sample accessed by SEM after HF etch is close to that obtained by MIR-IR evaluation based on Si-OH content (~170% additional damage), Figure 4.13b. Table 4.1 shows % increase of damage on +60 sec over-etched from post-etch step calculated from Si-OH content accessed by MIR-IR. With a larger sampling depth, MIR-IR can probe the totality of the patterned structure including both sidewalls and trench bottom. With its inherent high detection sensitivity, MIR-IR metrology can be a fast and quantitative tool to optimize plasma processing and minimize plasma induced damage.

Wafers	**Si-OH (mabs)**
Pristine (scaled)	**13**
Post-etch	**16 (+3)**
Post-strip	**24 (+11)**
+60 sec over-etch	**43 (+30)** **(+170% increase from Post-strip)**

Table 4.1 Additional dielectric damage on +60 sec over-etch sample from Post-strip evaluated by MIR-IR (Si-OH peak height).

4.4 Photometric accuracy (repeatability) test

Repeatability is a commonly encountered term used as a performance characteristic of an instrument. It is a measure of a system's consistency to achieve identical results across multiple measurements under consistent test conditions. Since Si-OH and Si-CH_3 content can serve as a practical means to evaluate plasma damage on trench low-*k*, +60 sec over-etched sample was used for the repeatability test. Si-OH and Si-CH$_3$ peak absorbance were quantified, measured by MIR-IR and T-IR respectively. As shown in top row of Figure 4.14, relative standard deviation (RSD) calculated were 2.2% (Si-OH) and 0.5% (Si-CH$_3$), measured from three different ATR crystals fabricated from the same wafer.

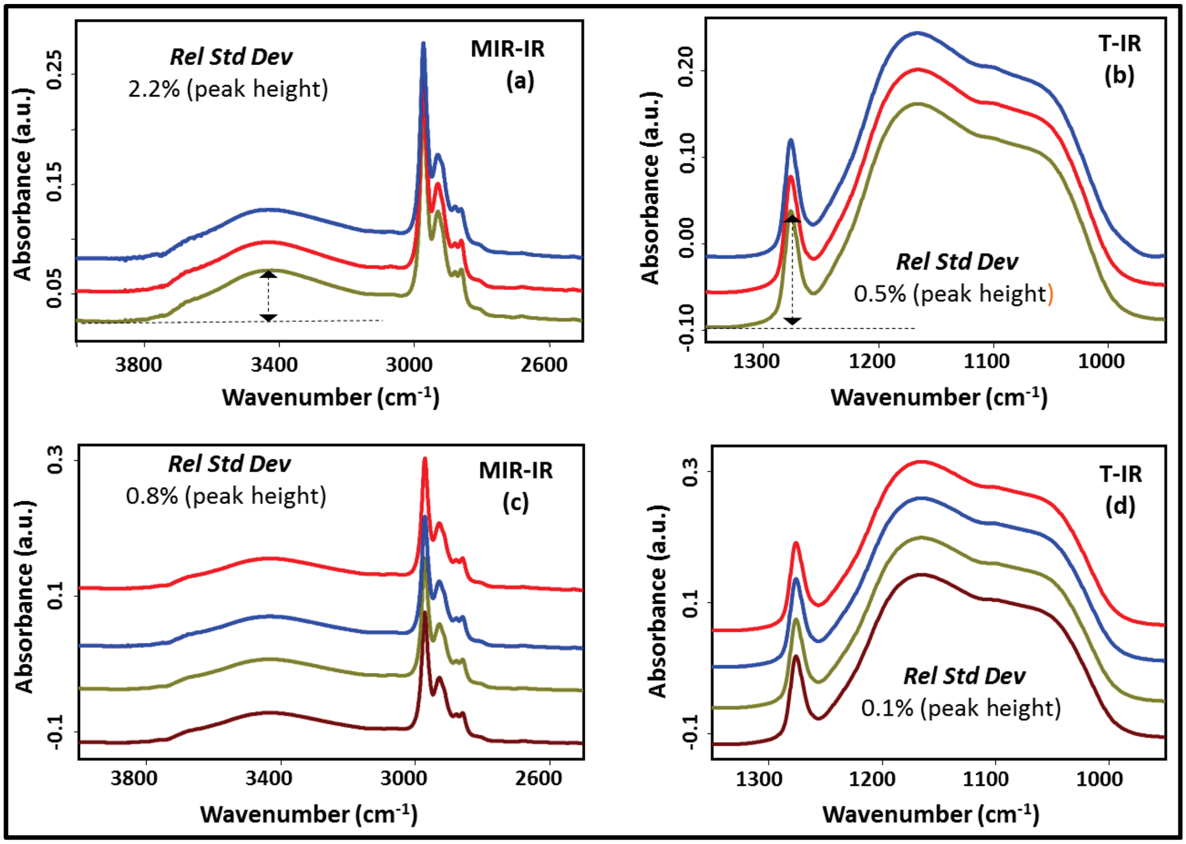

Figure 4.14 Photometric accuracy (repeatability) of +60 sec over-etch samples: MIR-IR (a) and T-IR (b) spectra with different ATR crystals prepared from the same wafer; and MIR-IR (c) and T-IR (d) spectra are quadruplet measurements of the same ATR crystal.

The RSD value lowered to 0.8% (Si-OH) and 0.1% (Si-CH$_3$) when quadruplet measurements were taken of the same ATR crystal, bottom row of Figure 4.14. The slightly higher RSD in the former measurement can attribute to sample variation across the wafer and error in exact ATR dimension fabrications. In addition, MIR-IR being highly surface sensitive can detect even the smallest change like the surface anchored Si-OH groups.

4.5 Ideal purge condition for reliable Si-OH measurement

Since surface silanol groups (Si-OH) are very prone to hydrophilic water molecules adsorption, it is critical that moisture level during spectra measurement is well controlled to obtain the true Si-OH reading. A +60 sec over-etch sample (has higher plasma damage) was chosen to find out the optimum time required where moisture has minimum effect on the surface Si-OH groups. As shown in Figure 4.15a, Si-OH (at ~ 3430 cm^{-1}) peak intensity at 0 min purge time is greatly affected by large moisture absorption at ~3600 – 3900 cm^{-1}. A large CO_2 peak (~ 2360 cm^{-1}) is also indicative of higher moisture level in the purging environment.

Majority of the moisture removal/desorption was observed within 5 mins of purging. The moisture level and the corresponding Si-OH peak height decreased with further increasing purge time, Figure 4.15a and 4.15b. A stabilized Si-OH reading obtained after 20 mins of dry air purge time, indicates optimized time where most of the water molecules has been desorbed from the sample surface, Figure 4.15b. Hence, all MIR-IR measurements in this work was carried out with 30 mins of dry air purge to obtain true Si-OH reading for accurate plasma damage quantification.

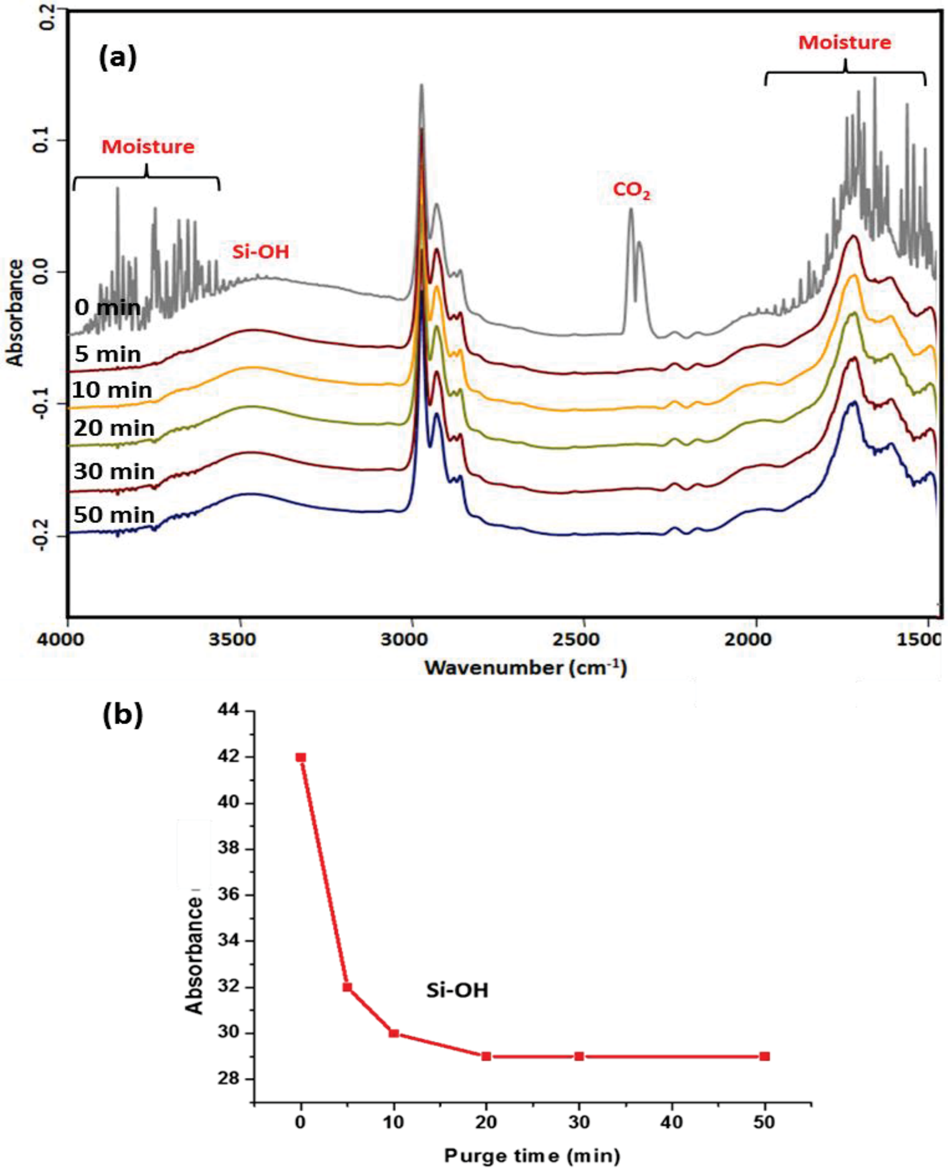

Figure 4.15 (a) MIR-IR spectra of +60 sec over-etch sample with different purge time interval. (b) Plot showing stabilized Si-OH reading with >20 mins of purging.

4.6 Summary

In summary, a novel MIR-IR metrology was used which showed useful spectroscopic details of chemical bonding transformations taking place during plasma etch and strip processing on both blanket and high aspect ratio dielectric trench structures. Plasma induced damage was quantified for each plasma processing steps. The observed increase of Si-OH and C=O and the decrease of Si-CH_3 IR absorption bands correlated well with increasing plasma induced damage, especially for more aggressive stripping process. In addition, chemical bonding structure of real post-etch residues deposited during etching process was revealed by IR and functional group specific chemical reactions. The etch residues removal efficiency by the following strip process was also monitored. Overall, MIR-IR technique is demonstrated to be a rapid and reliable comparative estimation tool for direct assessment of plasma-caused chemical bonding changes in low-*k* dielectric organosilicates and is useful for plasma process optimization to minimize plasma induced damage.

4.7 References

1) Shul, R. J.; Pearton, S. J. Handbook of Advanced Plasma Processing Techniques. Springer, NY, **2000**.
2) Baklanov, M. R.; Ho, P. S.; Zschech, E. *Advanced Interconnects for ULSI Technology*. John Wiley & Sons, Chichester, UK, **2012**.
3) Tagami, M.; Ogino, A.; Miyajima, H.; Shoba, H.; Baumann, F.; Ito, F.; Sponner, T. *ECS Transactions*. **2011**, 41 (7), 405-413.
4) Chaudhari, M.; Du, J.; Behera, S.; Manandhar, S.; Gaddam, S.; Kelber. *J. Appl. Phys. Lett*. **2009**, 94, 204102.
5) Behera, S. P.; Wang, Q.; Kelber, A. *J. J. Phys. D*. **2011**, 44, 155204.
6) Bao, J.; Shi, H.; Liu, J.; Huang, H.; Ho, P. S.; Goodner, M. D.; Moinpour, M.; Kloster, M. G. *J. Vac. Sci. Technol. B*. **2008**, 26 (1), 219.
7) Jinnai, B.; Nozawa, T.; Samukawa, S. *J. Vac. Sci. Technol*. **2008**, B 26, 1926.

8) Baklanov, M. R.; Travaly, Y.; Le, Q. T.; Shamiryan, D.; Vanhaelemeersch, S. Silicon Nitride, Silicon Dioxide, Thin Insulating Films and Other Emerging Dielectrics YIII. *ECS*. **2005**, PV 2005-01, 179-198.

9) Le, Q. T.; Baklanov, M. R.; Kesters, E.; Azioune, A.; Struyf, H.; Boullart, W.; Pireaux, -J. J.; Vanhaelemeersch, S. Electrochem. *Solid State Lett*. **2005**, 8 (7), F21-F24.

10) Iijima, T.; Lin, Q.; Chen, S.; Labelle, C.; Fuller, N.; Ponoth, S.; Cohen, S.; Lloyd, J.; Dunn, D.; Muzzy, C.; Gill, J.; Nitta, S.; Spooner, T.; Nye, H. *Proceedings of IEEE IITC 2006*. **2006**, 21.

11) Bao, J.; Shi, H.; Liu, J.; Huang, H.; Ho, P. S.; Goodner, M. D.; Moinpour, M.; Kloster, M. G.; McSwiney, L. M. *J. Vac. Sci. Technol. A*. **2010**, 28 (2).

12) Wang, Y.H.; Gui, D.; Kumar, R.; Foo, P. D. *ECS Solid State Lett*. **2003**, 6 F1.

13) Maex, K.; Baklanov, M. R.; Shamiryan, D.; Iacopi, F.; Brongersma, S. H.; Yanovitskaya, S. Z. *J Appl. Phys*. **2003**, 93, 8793-8841.

14) Abell, T.; Lee, J.; Moinpour, M. *Mater. Res. Soc. Symp. Proc*. **2006**, 914.

15) Abell, T.; Zhou, Y.; Le, Q. T.; Shamiryan, D.; Moinpour, M.; Kloster, G. Presented at ISMT Ultralow k Workshop. Burlingame, CA, **2002**.

16) Worsley, M. A.; Bent, S. F.; Fuller, C. M. N.; Tai, L. T.; Doyle, J.; Rothwell, M.; Dalton, T. *J. Appl. Phys*. **2007**, 101, 013305.

17) Iacopi, F.; Stucchi, M.; Richard, O.; Maex, K. *Electro. Chem. Sol. St. Lett*. **2004**, 7 (4), 79-82.

18) Mukherjee, T.; Rimal, S.; Koskey, S.; Chyan, O.; Singh, K. J.; Myers, A. M. *ECS Solid State Lett.* **2013**, 2, N11.

19) Le, Q. T.; de Marneffe, J. -F.; Conard, T.; Vaesen, I.; Struyf, H.; Vereecke, G. *J. Electrochem. Soc.* **2012**, 159, H208.

20) Lam, J. C. K.; Huang, M. Y. M.; Tan, H.; Mo, Z., Mai, Z.; Wong, C. P.; Sun, H.; Shen, Z. *J. Vac. Sci. Technol. A.* **2011**, 29, 5.

21) Ross, N.; Shrestha, K.; Chyan, O.; Littler, C. L.; Lopes, V. C.; Syllaios, A. J. *Mater. Res. Soc. Symp. Proc*. **2013**, 1536, 127.

22) Rimal, S.; Ross, N.; Pillai, K. S. M.; Singh, K. J.; Chyan, O. *ECS Trans.* **2011**, 41, 31.

23) Chen, J. J.; Xu, F.; Ponnuswamy, T.; Chan, R.; Wu, J. J.; Prasad, A.; Chyan, O.; Sees, J. A.; Hall, L. H. *Recent Res. Devel. Applied Spectroscopy*. **2000**, 3, 81.

24) Chyan, O.; Chen, J. J.; Xu, F.; Wu, J. *Anal. Chem*. **1997**, 69, 2434.

25) Harrick, N. J. *Internal Reflection Spectroscopy*; Interscience Publishers: NY, **1967**.

26) Burrows, V. A.; Chabal, Y. J.; Higashi, G. S.; Raghavachari, K.; Christman, S. B. *Appl. Phys. Lett.* **1988**, 53, 998.

27) Legrand, A. P, *The Surface properties of Silicas*; John Wiley & Sons: Chichester, **1998**.

28) Shi, H.; Bao, J.; Smith, R. S.; Huang, H.; Liu, J.; Ho, P. S.; McSwiney, M. L.; Moinpour, M.; Kloster, G. M. *Appl. Phys. Letters*. **2008**, 93, 192909.

29) Kim C. Y.; Kim S. H.; Navamathavan, R.; Choi, C. K.; Jeung, W.Y. *Thin Solid Film*. **2007**, 516.

30) Majumdar, A.; Das, G.; Patel, N.; Mishra, P.; Ghose, D.; Hippler, R.; *J. Electrochem. Soc.* **2008**, 155, D22-D26.

31) Uchida, Y.; Hishiya, S.; Fuji, N.; Kohmura, K.; Nakayama, T.; Tanaka, H.; Kikkawa, T. *Microelectron. Eng.* **2006**, 83, 2126.

32) Costello, C.; McCarthy, T. *Macromolecules*. **1987**, 20, 2819.

CHAPTER 5

INVESTIGATION OF ETCH RESIDUE DEFECT FORMATION ON TiN HARDMASK AFTER FLUOROCARBON PLASMA ETCH

5.1 Introduction

Resistive-capacitive (RC) delay is one of the major hindrance towards downscaling of integrated circuits (ICs). Minimizing the device dimension lead to increase in the resistance due to decrease of metal cross section and increase of wiring length, and also increase in inter-line capacitance with the reduction in interline spacing. The necessity to decrease RC delay has led to the implementation of various new materials and advanced patterning schemes in the BEOL fabrication processes. Copper replaced aluminum as metal of choice for wiring because of its lower resistivity and higher resistance to electro-migration. Similarly, conventional SiO_2 (k= ~4) was replaced by lower dielectric constant materials (k= 2-3) as inter-liner to decrease capacitance, and are termed as low k/ ultra-low k dielectrics [1-2]. Two approaches are generally used to lower the k value in dielectrics: by using low polar bonds such as C-C, C-H, $Si\text{-}CH_3$ etc, and/ or by introducing porosity to reduce their density. This reduces the inherent robustness of the dielectric material.

Implementation of low k dielectrics into Cu interconnects has faced several challenges because of some of the issues such as thermal and mechanical induced cracking, adhesion loss, poor mechanical strength, chemical interactions, and poor thermal conductivity [3]. Low k dielectrics patterning also faces critical challenges like etch rate uniformity, profile control and damage due to various plasma processing. Photoresist ashing following trench opening is one of the most challenging patterning step and is also harmful to fragile low-k dielectric materials. Strip/

Ash chemistries targeted to remove organic photoresist (PR) layer also removes organic hydrophobic groups (-CH_3) from low-*k* materials, thereby making them hydrophilic. A hydrophilic surface in turn absorbs moisture causing an increase in *k* value, which is detrimental for further processing. Moreover, as feature sizes continue to shrink, PR thickness is also going down rapidly [4]. For example, according to Semiconductor Industry Association roadmap, ~500 nm PR was used to pattern 150nm features, but for sub-100nm feature sizes only less than 200nm of PR may be required [5]. This will cause to change the etch selectivity of the underlying substrate and can result in critical dimension (CD) change. Due to the above mentioned constraints, development of advanced patterning schemes has become a necessity, especially at smaller technology nodes. In technology nodes higher than 65 nm, the structure dimensions are large enough to tolerate some sidewall damage caused by the strip process, hence patterning scheme was successful. However, the continuous shrinking of CD brings new challenges. First, there is a significant decrease of resist thickness in order to avoid pattern collapse, and second the narrow lines in low-*k* does now allow any damage on the sidewalls.

Implementation of hardmask scheme serves as an alternative to overcome the above mentioned challenges associated with the adoption of low-*k*/ ultra low-*k* dielectrics [6-7]. Studies have shown that hardmask films provide high etch selectivity to low-*k* dielectrics and PR, and also eliminate/ minimize low-*k* damage caused by the resist strip process [5]. There are two major types of hardmask that can be used: dielectric and metal. A dielectric hardmask is usually silicon based like SiO_2, SiC or SiN, and metal hardmasks consist of metal nitrides (TiN, TaN). Si-based hardmask is not well suited for carbon doped oxide (CDO) low-*k* materials, because both the low-*k* material and the hardmask contain Si and hence cannot reach a high selectivity. Because of this low selectivity, thicker hardmask must be imposed and if left on the low-*k* structure after patterning will increase the effective dielectric constant value. The Si-based hardmask is also challenging to remove and can pose problems since it has a similar composition to CDO low-*k* material. Another alternative for CDO low-*k* patterning is to use TiN hardmask. TiN provides high etch selectivity for low-*k* materials because Ti etch product i.e. TiF_4 has lower volatility as compared to SiF_4 (low-*k* etch product). Another advantage of using metal hardmask is that it does not add to the effective *k* value because it is removed at the chemical mechanical polishing (CMP) process.

Despite of many advantages of metal hardmask use, some of the disadvantages are the formation of metal-containing etch residues, formation of micromasking caused by low volatile Ti etch by-products, and mechanical stress imposed to fragile low-*k* materials (cause wiggling) [8]. Formation of metal-containing etch residues is considered one of the major drawback because they are very difficult to remove and can cause serious device reliability issue. Studies have shown that these etch residues are TiF_x based residues and are time dependent defects growing on TiN HM after fluorocarbon plasma etching. It was found that the likely factors to contribute to the formation of etch residues defects are actually triggered by F residue formed during CF_x etching and the following exposure in air, Figure 5.1 [9]. Recent report show that TiF_x defects are actually TiO_x crystals covered by TiF_x residue catalyzing the crystal growth [10]. However, the nature and growth mechanism of so called TiF_x residues are unclear and systematic studies have not been published yet.

In order to help create defect free and highly reliable interconnects, detail knowledge of chemical bonding information and growth mechanism of the TiN etch residue is essential. In this study, we tried to shed new insights into the chemical bonding associated of the etch residue defect and proposed a likely mechanism of residue growth, which can facilitate in efficient residue removal/ prevention.

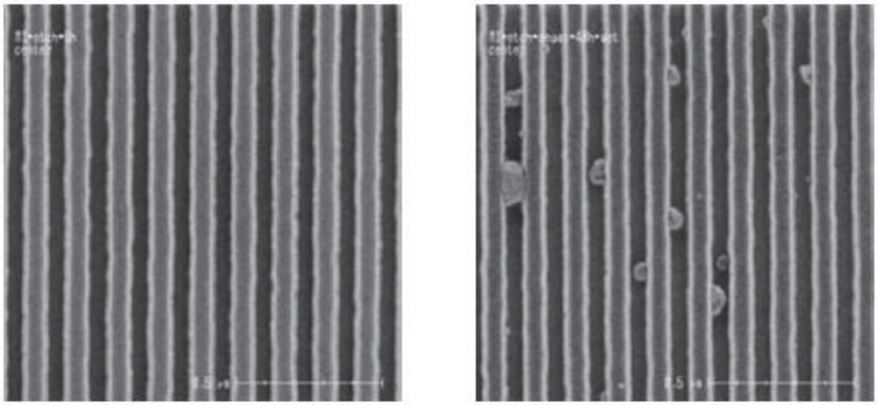

Figure 5.1 Top CD SEM of TiN hardmask, a) after etching and b) 24 hours air exposure [9].

5.2 Experimental

Preparation of TiN blanket wafers

In this work, pristine TiN blanket wafers were prepared by PVD method with a thickness of ~10 nm. TiN thickness was verified by ellipsometry measurement. To study and analyze post-etch residue and growth defects, wafers were gone through CF_x based plasma exposure. Furthermore, effect of post-etch treatments (PET) on residue growth using N_2 and N_2/CO plasmas were also investigated. Five different wafers were prepared and processed as 1) pre-etch: pristine TiN only; 2) trench etch (no PET): CF_x based plasma to etch TiN surface; 3) trench etch + N_2 PET (high temperature, low pressure, 60 sec); 4) trench etch + N_2/CO PET (low temperature, high pressure, 60 sec).

Characterization

Blanket wafers were cut and fabricated into attenuated total reflectance (ATR) parallelograms (10 x 60 x 0.8 mm, 45° bevel angle) for MIR-IR characterization. Both MIR-IR and Transmission IR (T-IR) spectra were measured using a Bruker V-70 FT-IR spectrometer under constant dry air ($CO_2 < 1$ ppm) purge. MIR-IR and T-IR spectra of blanket TiN coupons were taken against clean bare silicon (SC1 cleaned + HF etched) substrates as background at 4 cm^{-1} resolution as the average of 100 individual spectra. XPS analyses were conducted using a PHI 5000 Versa Probe equipped with an Al K_α (1486.7 eV) radiation source. Top down SEM images were obtained with a Hitachi S-5500 FE-SEM (CART). TiN thickness measurements were performed using ellipsometry (LAM).

DIW treatment

Wafer coupons were immersed in DIW and heated at 50 ˚C for ~10 mins. All coupons were thoroughly rinsed with UPW and N_2 blow dry, followed by FT-IR, XPS and SEM analyses.

5.3 Results and Discussion

5.3.1 Residue composition on TiN surface after fluorocarbon plasma etch

In this work, the impact of CF_x plasma etch on TiN etch residue formation was investigated, and correlated to pristine TiN blanket film without plasma exposure. Figure 5.2 (a) shows clean surface of as deposited TiN film, while after 24 hours of air exposure of the same surface after CF_x etch shows residues all over, Figure 5.2 (b). To have a better understanding of the mechanism of residue growth on TiN, surface composition, chemical bonding and surface topography were investigated using XPS, MIR-IR and SEM respectively.

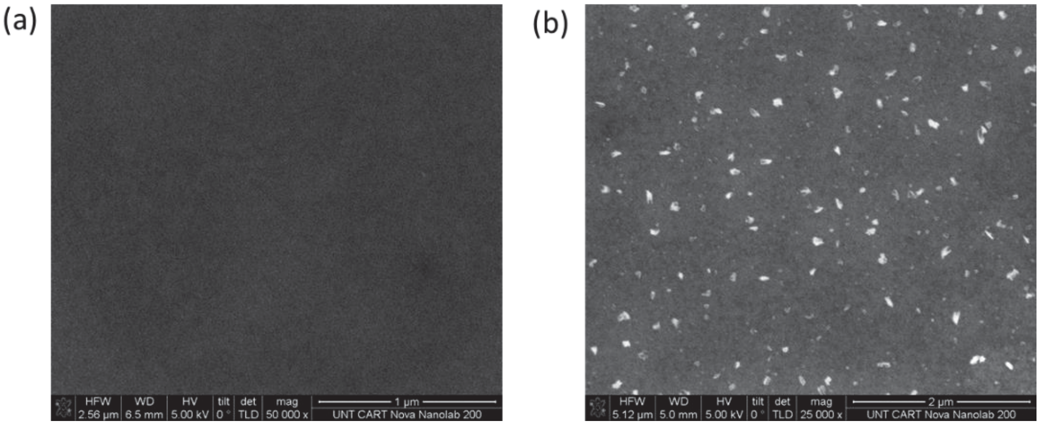

Figure 5.2 Top view SEM of a) TiN hardmask as deposited and b) after FC etching and >24 hours of air exposure.

XPS analysis of pristine TiN shows surface composition of titanium (27.7%), oxygen (25.4%), carbon (22.3%), nitrogen (21.2%), silicon (2.3%), and fluorine (1.0%). The presence of very low level of fluorine in un-etched pristine TiN can come from chamber contamination. The Ti 2p (3/2) core-level spectrum for pristine TiN and etched TiN is depicted in Figure 5.3. The pristine TiN surface shows a major peak at 458.2 eV attributed to titanium bonded to oxygen (Ti-O_2), and 455.4 eV for titanium bonded to nitrogen (Ti-N) [11]. XPS analysis on TiN after etching show that the surface is composed of titanium (15.0%), oxygen (26.9%), carbon (22.0%), nitrogen (9.1%), silicon (6.5%), and fluorine (16.5%). However, after fluorocarbon etch, the oxidized TiN surface shows blue shift in the Ti-O_2 peak, and can be attributed to more electronegative fluorine atoms bonded to Ti-O_2 or just fluorine bonded to titanium (Ti-F_x). As can be seen in Figure 5.3, the peak at 459.6 eV can be assigned to Ti-F_x/Ti-O-F_x [11-12], a part of etch residues composition. The F 1s core-level spectra (Figure 5.4) exhibit one dominant peak at 685.1 eV which can be attributed to fluorine bonded to titanium (Ti-F_x) and or fluorine bonded to oxidized titanium (Ti-O-F_x) [13].

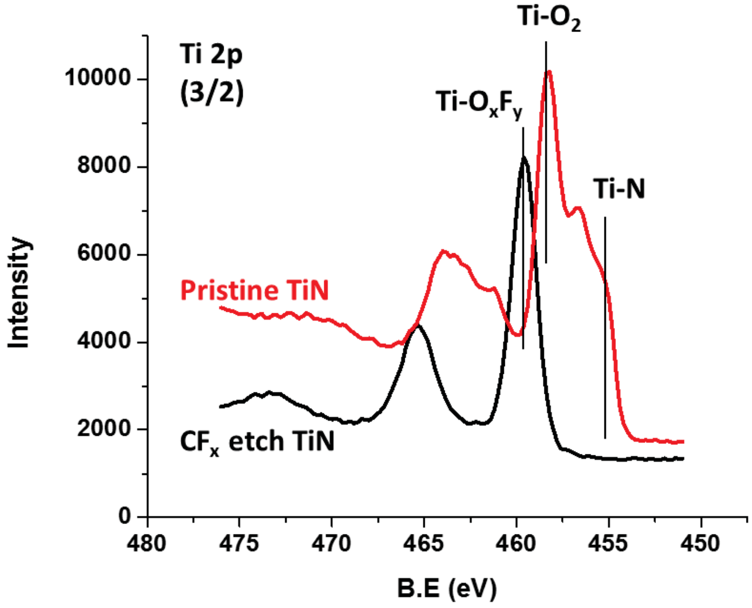

Figure 5.3 XPS Ti 2p (3/2) spectra of un-etched TiN and CF$_x$ etched TiN.

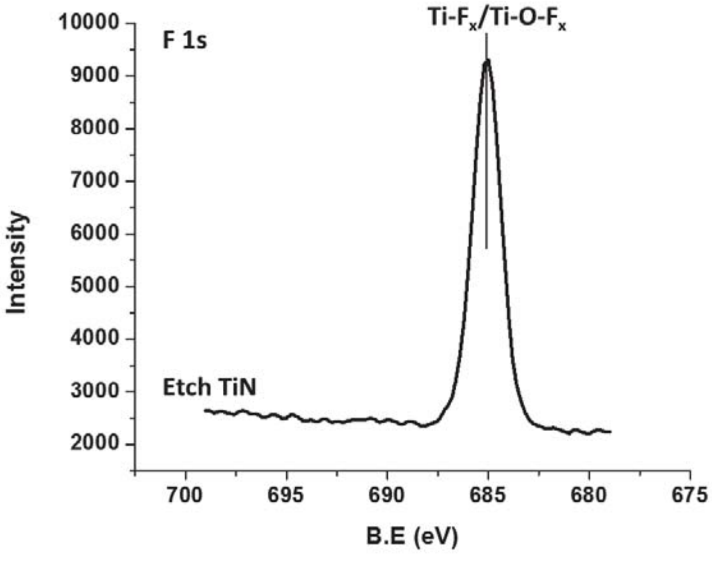

Figure 5.4 XPS F 1s spectra of TiN after CF$_x$ etch.

Interestingly, no peak at 688.5 eV was observed for fluorine bonded to carbon (F-C). This observation was correlated with C 1s spectra, it only showed small peaks of carbon bonded to fluorine at 287.3 eV and 289.4 eV for C-CF_x and C-F respectively [14]. The XPS data suggests that TiN surface after fluorocarbon plasma etch is not mainly covered by C-F_x residues.

An interesting data were observed from XPS N 1s core-level spectra. Pristine TiN surface exhibited a dominant peak at 397.1 eV assigned to nitrogen bonded to titanium [11]. However, two new peaks were observed for TiN after CF_x etch. The peak at 399.4 eV can be attributed to amine group (-NH_2) and the higher binding energy peak at 402.4 eV can be assigned to ammonium group (-NH_3^+), most likely bound to more electronegative fluorine atoms, Figure 5.5. XPS data was very well substantiated with surface enhanced MIR-IR analysis on TiN surface after etching. Figure 5.6 shows MIR-IR spectrum of TiN after CF_x etch with respect to clean bare silicon as background, and exhibits broad overlapping vibrational bands between 2700 – 3700 cm^{-1}. The broad overlapping peaks can be dissected into five peaks. The doublet peaks at 3442 cm^{-1} and 3365 cm^{-1} can be attributed to N-H vibration of primary amines (-NH_2), and the higher intensity peaks

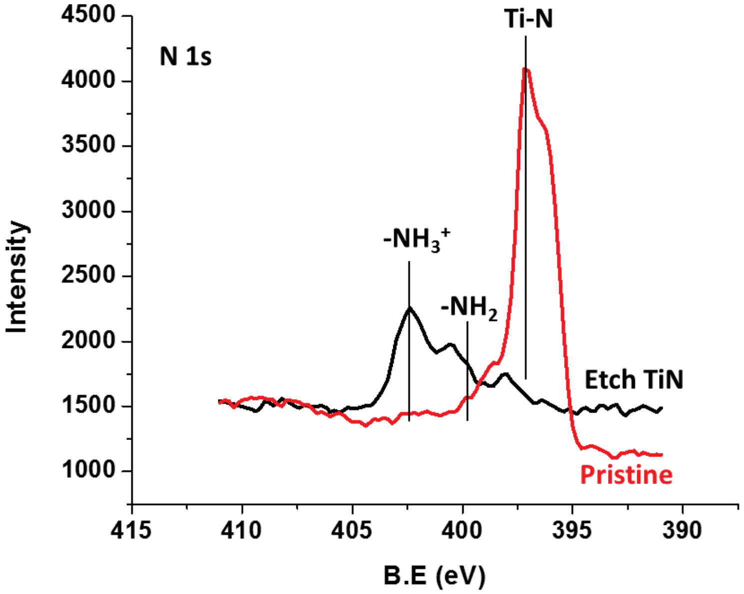

Figure 5.5 XPS N 1s spectra of un-etched TiN and CF_x etched TiN.

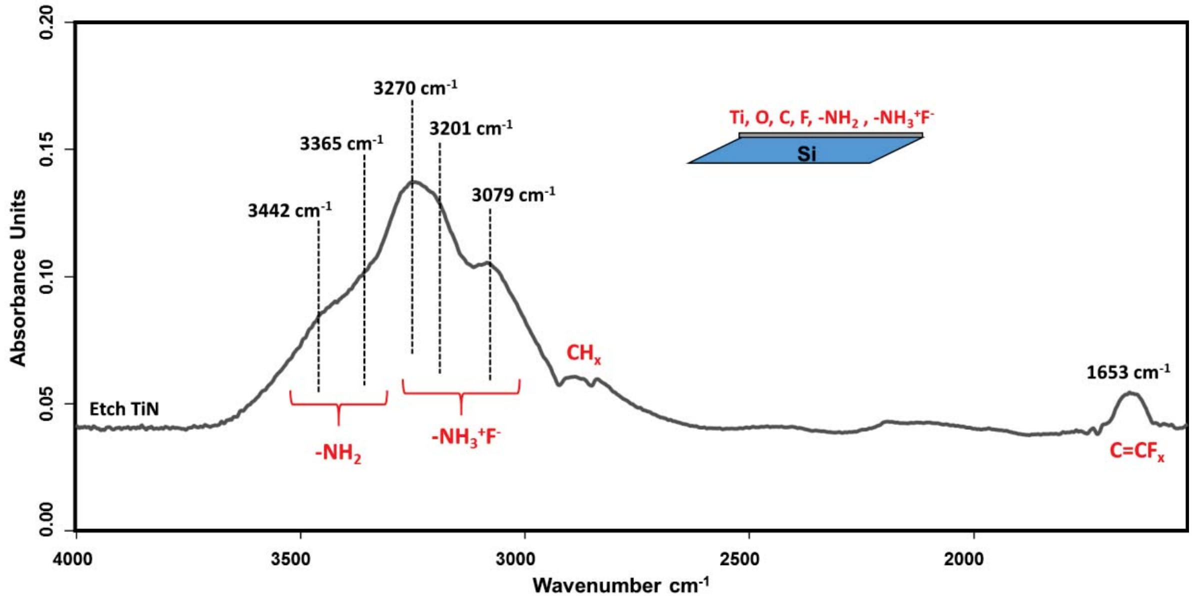

Figure 5.6 MIR-IR spectrum of TiN surface modification after fluorocarbon plasma etching.

at 3270 cm^{-1}, 3201 cm^{-1} and 3079 cm^{-1} for N-H vibrations of the ammonium fluoride salt ($-NH_3^+F^-$) [15]. MIR-IR data clearly suggests that TiN surface after etching is also largely composed of amines and ammonium components and could be a part of TiN hardmask etch residues defects.

5.3.2 Effect of in-situ post-etch treatment on TiN residues growth

Post-etch treatment (PET) is a widely used approach in wafer processing to reduce halogen based residues, and also to minimize cross contamination by volatile halogen by-products [10]. Different types of plasma PETs such as H_2, O_2, NH_3 and CH_4 have been reported in literatures in order to minimize or avoid TiF_x related residues [9-10]. In this work, three different PETs were analyzed: 1) N_2 PET (LTHP=low temperature high pressure), 2) N_2 PET (HTLP=high temperature low pressure), and 3) N_2/CO PET (LTHP= low temperature high pressure), and were compared to etched TiN with no PET. However, our preliminary data showed likely optimized PETs were N_2

(HTLP) and N_2/CO (LTHP), hence other PETs are not reported. Table 5.1 shows surface composition determined by XPS after etching and likely optimized PETs. XPS elemental composition clearly shows total F 1s concentration decrease with PETs (> 70%) compared to TiN after etching. XPS data on Figure 5.7 presents F chemical states on TiN after etch and the following changes after N_2 and N_2/CO PETs. Most of the F residues on TiN surface are in the form of TiF_x residues as depicted by the F-Ti bonds (685.1 eV), and the remaining small contribution are in the form F-CH bonds (686.4 eV). It is clear that N_2 and N_2/CO PETs performed effective TiN defluorination, Figure 5.7. It is also interesting to note that Ti and N concentration decreases with etching process, however it is higher with N_2/CO PET compared to N_2 PET, Table 5.1. XPS analysis on Ti 2p data also shows a slightly higher peak at 455.2 eV for Ti-N on N_2/CO PET (data not shown). XPS data suggests that there is a possibility of Ti-N bond recovery (re-nitridation) taking place with N_2/CO PET. Surprisingly, the observance of Si 2p indicates the thickness of TiN less than 10 nm, or possibility of over-etch of TiN with CF_x etching.

Conditions	**Ti 2p**	**N 1s**	**O 1s**	**C 1s**	**F 1s**	**Si 2p**
Etch	15.0%	9.1%	28.9%	22.0%	16.5%	8.5%
Etch+N_2 (HTLP)	6.6%	6.4%	39.8%	25.4%	4.7%	17.1%
Etch+N_2/CO (LTHP)	11.1%	13.9%	38.2%	18.4%	4.5%	13.9%

Table 5.1 XPS analyses on TiN surface composition after etching, N_2 PET and N_2/CO PET.

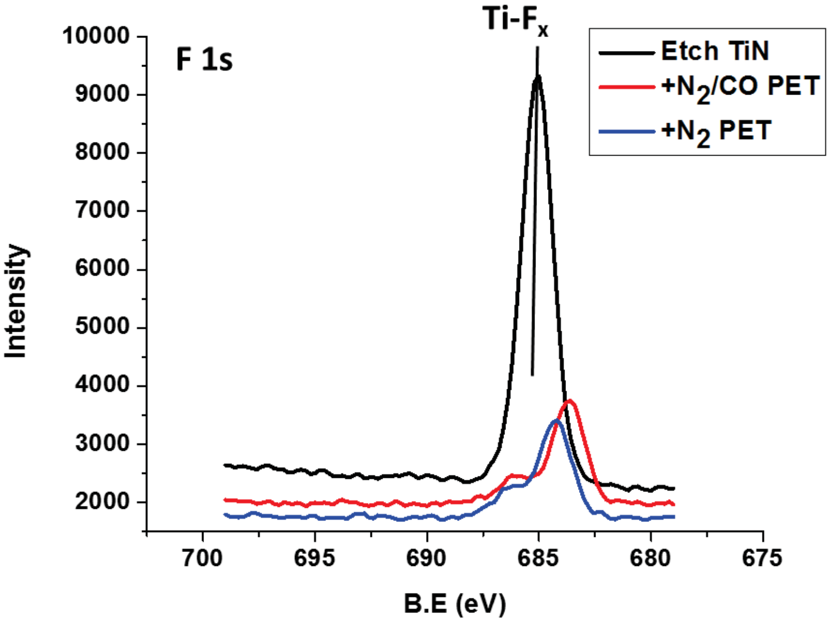

Figure 5.7 XPS F 1s spectra of TiN after etching and with different post-etch treatments.

MIR-IR provides valuable insights into the chemical bonding transformation taking place following different PETs. As discussed earlier, MIR-IR show intense IR absorption peaks of ammonium fluoride ($-NH_3^+F^-$) and relatively less intense peaks of amines ($-NH_2$) on TiN surface after etching. However, with N_2 PET (HTLP) and N_2/CO PET (LTHP) MIR-IR shows effective peak intensity decrease of amines and ammonium components, Figure 5.8. The N_2 PET (HTLP) show surface defluorination as a result of reduced pressure and increased substrate temperature. Higher substrate temperature (>90 °C) assisted in effective defluorination, and can be attributed to surface ammonium fluoride salts being volatilized at higher temperatures. However, other parameters such as power, frequency, N_2 flow, pressure and exposure time also plays a crucial role in further optimization. MIR-IR shows further interesting result after N_2/CO PET compared to N_2 PET. Higher removal of ammonium fluoride salt and slightly increased amine components with

N_2/CO PET, Figure 5.8 correlates well with more defluorination and a possibility of re-nitridation, also corroborates with XPS data.

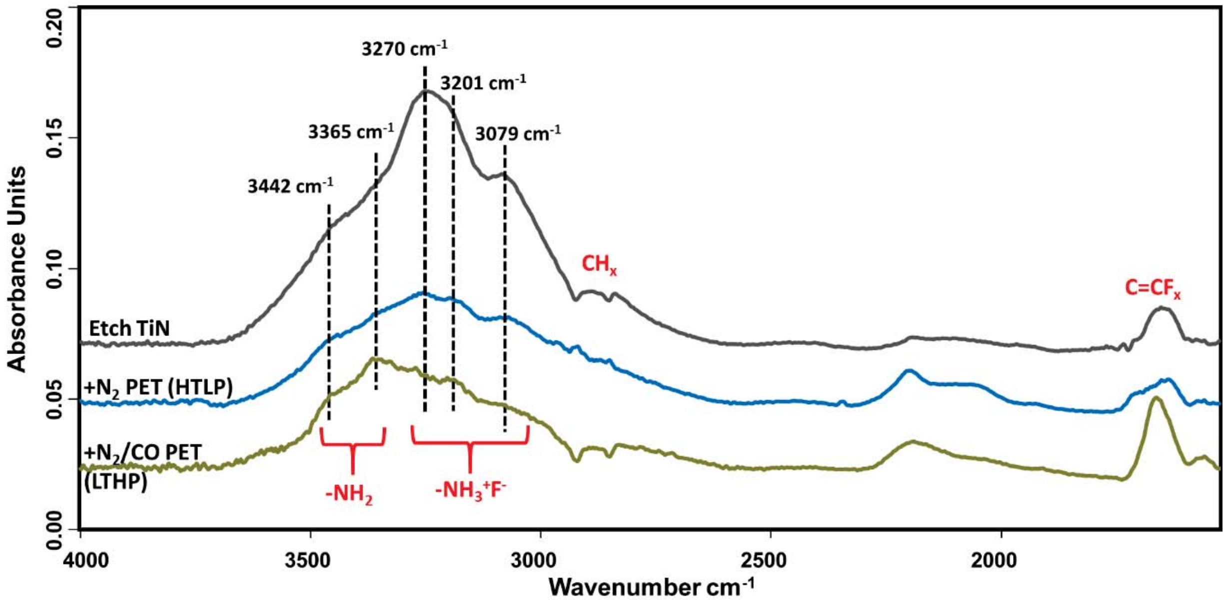

Figure 5.8 MIR-IR spectra of TiN after fluorocarbon plasma etching, +N_2 PET and +N_2/CO PET.

The most comprehensive information regarding TiN etch residue and the effect of N_2/CO PET is provided by comparative analyses of MIR-IR, XPS and SEM as shown in Figure 5.9. MIR-IR shows higher content of ammonium fluoride after etching, whereas N_2/CO PET cause substantial reduction of ammonium fluoride content, however has more of an amine component than ammonium fluoride component, Figure 5.9 (a). XPS N 1s high resolution spectra, Figure 5.9 (b) presents substantial amount of ammonium groups bonded to fluoride ions (-$NH_3^+F^-$ at 402.4 eV) on the etched surface, but the presence of the same components is not observed after N_2/CO PET. The surface is instead mostly composed of amine groups as can be seen by the peak at 399.4 eV (-NH_2). SEM analyses reveals etch residues defect formation all over the surface on CF_x etched TiN surface with thickness of ~125 nm, Figure 5.9 (c). However, no such lumps of residues were observed on N_2/CO PET treated surface. The combined comparative data clearly indicates the presence of residues on etched TiN surface and ammonium fluoride salts (-$NH_3^+F^-$) could likely be a part of etch defects.

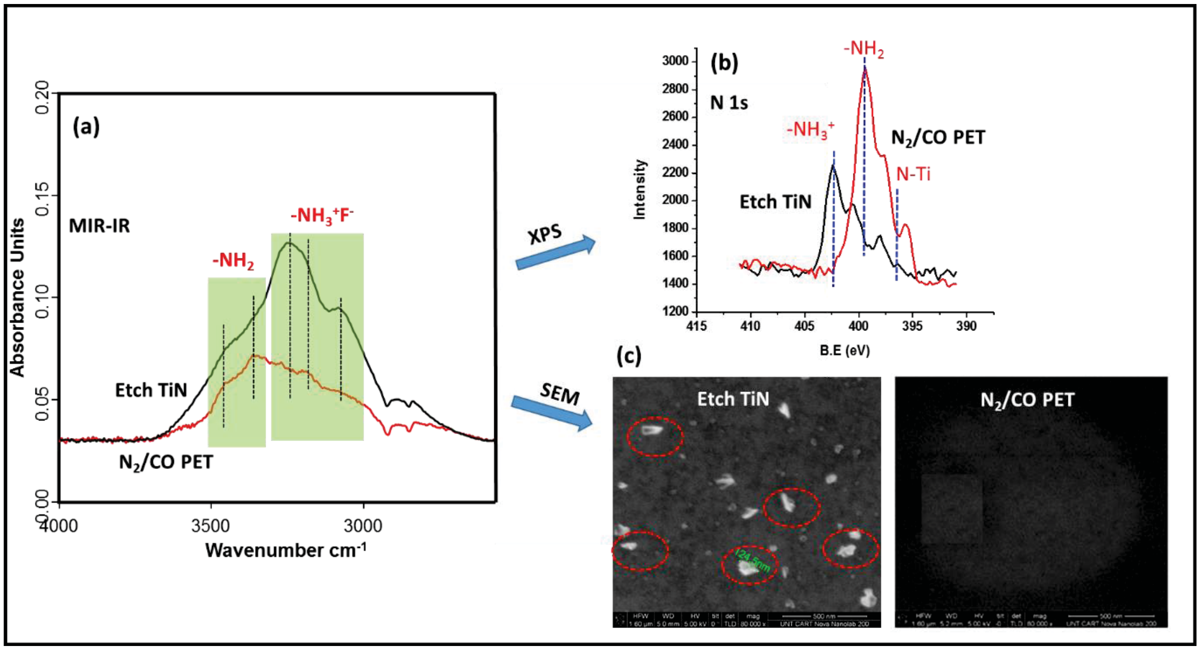

Figure 5.9 Comparative analyses of a) MIR-IR vs. b) XPS and c) SEM on TiN after etching and after N_2/CO PET.

5.3.3 Water soluble amine components identified on TiN surface

MIR-IR analyses revealed the presence of amines (-NH_2) and ammonium fluoride salts (-$NH_3^+F^-$) on the surface after CF_x etch. Amines being a hydrophilic base and ammonium fluoride an ionic salt were treated with polar solvent (water, *k*= ~80). Figure 5.10 present MIR-IR and T-IR spectra of surface modification caused from DIW rinse on etch residues. MIR-IR spectra, Figure 5.10 (a) shows reduction in the IR absorption bands associated of amines and ammonium fluoride with DIW rinse. The etched TiN (no PET) and N_2/CO PET showed maximum removal of the amine related components likely a part of etch residue defects. However, associated peak

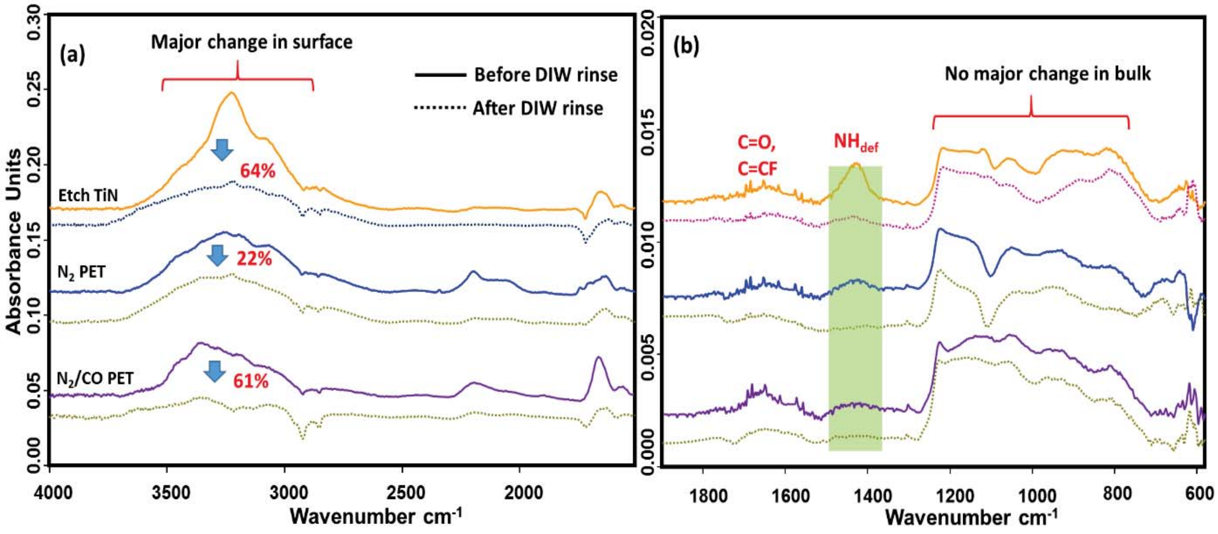

Figure 5.10 MIR-IR (a) and T-IR (b) evaluation of etch residues defect after etched and PETs TiN film before (solid line) and after (dotted line) DIW rinse.

signals were still observed (< 40%) on the surface, and could be attributed to silanol bonds (Si-OH) formation after DIW rinse and or some unreacted amine components left over. T-IR analyses also shows a decrease in N-H deformation bonds (~1420 cm^{-1}) with DIW rinse, however most of the bulk absorption (700 – 1250 cm^{-1}) were not affected by the rinse treatment.

MIR-IR analyses were also complemented by XPS measurement on before and after DIW rinse treatment. MIR-IR spectra on Figure 5.11 (a) is a differential spectra obtained and shows a net change after DIW rinse on etched TiN and N_2/CO PET. DIW rinse treatment at 50 °C for ~10 minutes show effective removal of $–NH_3^+F^-$ component from etched surface along with $–NH_2$ groups. XPS data, Figure 5.11 (b) (top) also supports the major surface coverage of etched TiN with $NH_3^+F^-$ salt (before rinse), however is removed efficiently with DIW rinse as can be observed by the decrease in 402.4 eV peak intensity. The N_2/CO PET surface majorly contained with the amine groups ($-NH_2$) is also removed with DIW rinse as observed by the negative absorbance IR doublet peaks at 3442 cm^{-1} and 3365 cm^{-1}. XPS shows similar result with the decrease of the peak intensity at 399.4 eV for N-H bonding of the $–NH_2$ groups, Figure 5.11 (b) (bottom).

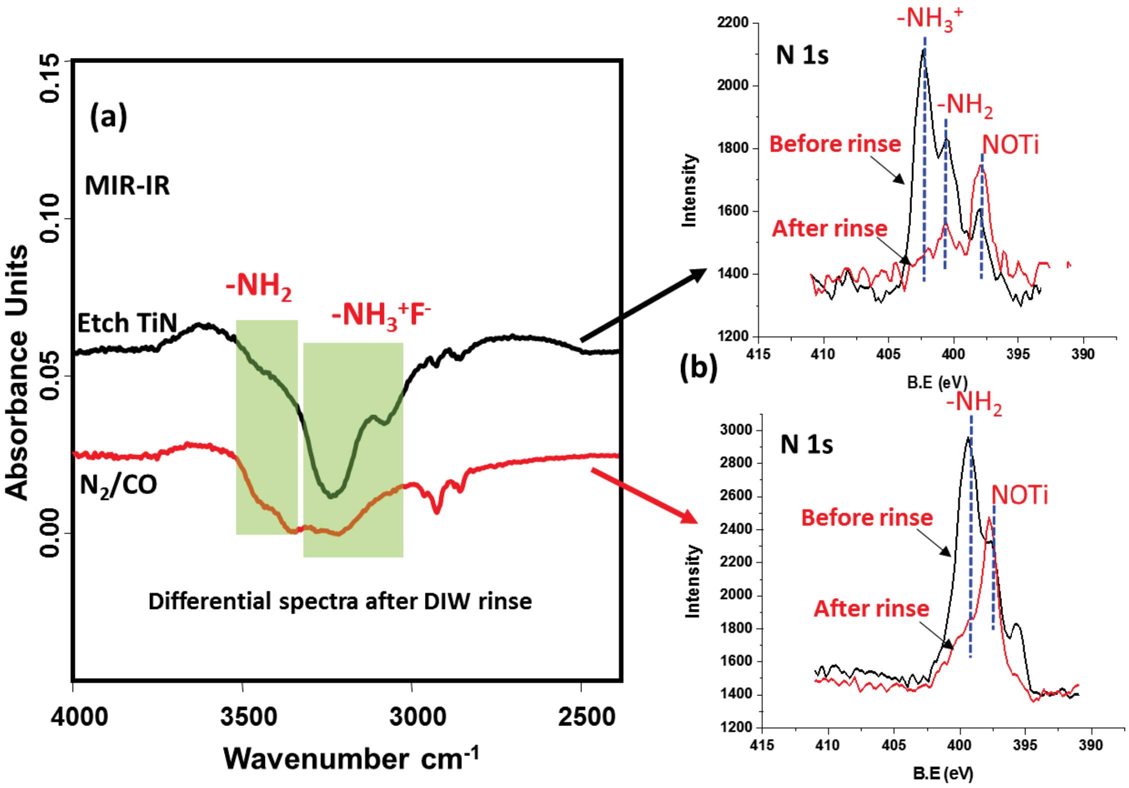

Figure 5.11 Comparative analyses of a) MIR-IR vs. b) XPS before and after DIW rinse on etched and N_2/CO PET surface.

Both MIR-IR and XPS verifies the presence of large quantity of amines and ammonium fluoride components on TiN surface with etch defect after CF_x etch, and a possibility of correlation to defect formation. It was expected that with DIW rinse the etch residues would be removed since ammonium fluoride components were effectively removed with the treatment, Figure 5.11. SEM analyses, Figure 5.12 on etched TiN before and after DIW rinse however shows the presence of etch defects even after the water rinse treatment. SEM data suggests that $–NH_3^+F^-$ and $–NH_2$ groups could be a part of etch defect and/ or on the surface. If ammonium components were fully part of

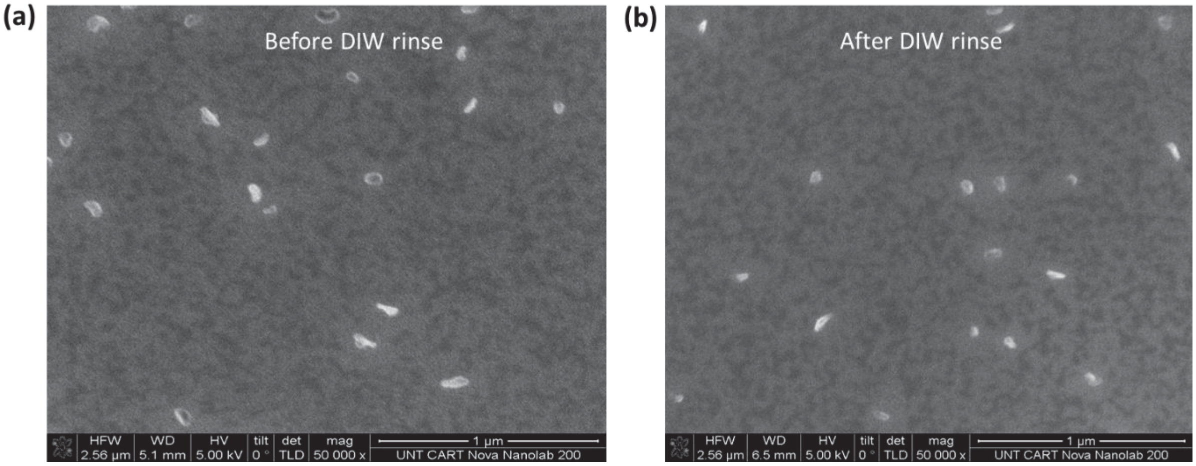

Figure 5.12 Top down SEM images on TiN after etching before (a) and after (b) DIW rinse.

the etch defect then we would observe complete removal of defects after DIW rinse , however the observance of defects still on the surface after rinse (Figure 5.12) suggests that ammonium components are either only on the surface (non-defect surface) and or a catalyzing medium for defect formation (Ti-OF_x)

5.3.4 Possible role of amine components in the etch residue defect formation

The presence of $–NH_3^+F^-$ and $–NH_2$ components observed by MIR-IR and XPS analyses might not be a part of defect but only present on the surface (verified by SEM after DIW rinse). However, the obtained data shows a strong correlation between the two amine components and the etch residue defect formation. XPS data on Figure 5.13 presents two types of TiO_x observed on the surface. The first type is the Ti-O_x observed at higher binding energy that is bound to fluorides, representing a peak at 459.5 eV (Ti-O_xF_y), and showing only on the surface after CF_x etch process (correlates well with increased $–NH_3^+F^-$ components observed in MIR-IR and visual defects observed in SEM). The second type of Ti-O_x is observed at 458.2 eV on the surface where it is not bound to fluorides such as on the un-etched pristine TiN and likely optimized N_2/CO PET. Based on this observation, it was hypothesized that the first type (Ti-O_xF_y) is most likely activated by $NH_3^+F^-$. The ammonium fluoride groups formed on the surface acts as a transporting agent of fluorides to the TiO_x activated sites and catalyzes the growth formation of Ti-O_xF_y etch defects.

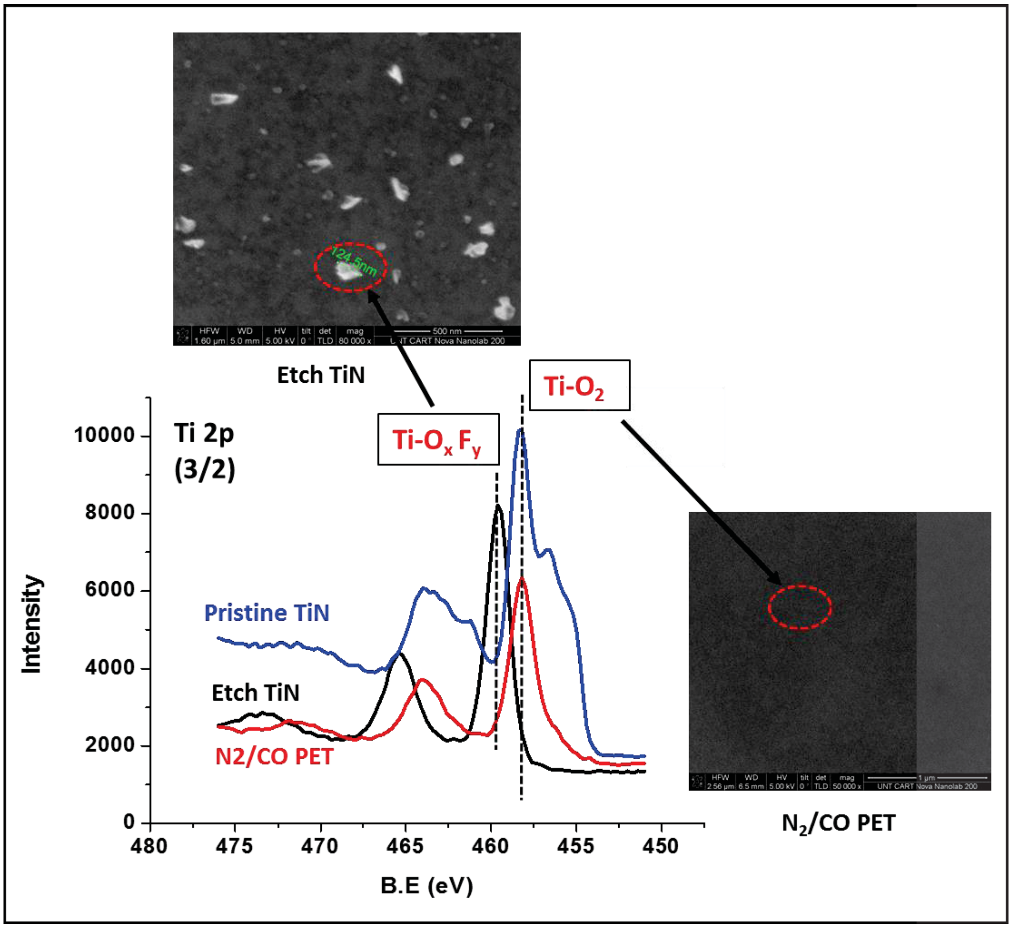

Figure 5.13 XPS Ti 2p (3/2) spectra of pristine TiN, etched TiN and N_2/CO PET and the corresponding SEM images.

5.3.5 Possible mechanism of residue growth on TiN hardmask after fluorocarbon etch

Based on the data observed/obtained (MIR-IR, XPS and SEM) we propose a plausible mechanism of residue defect growth on TiN after CF_x etch, Figure 5.14. The first step involves formation of HF when fluorine species from TiN surface after CF_x etch reacts with moisture, equation 1 [16]. Literature reports have proposed that the following reaction of HF and Ti metal could induce metallic defect formation [14, 16], however in-depth formation mechanism is not proposed. Based on the observance of $-NH_2$ and $–NH_3^+F^-$ components from MIR-IR analysis (Figure 5.9), we propose a different mechanistic route. Amines being a hydrophilic base on the surface reacts with HF to form ammonium fluoride salt as shown in the following equation:

$4F + 2H_2O \rightarrow 4HF + O_2$ (1)

$HF + R\text{-}NH_2 \rightarrow R\text{-}NH_3^+F^-$ (2)

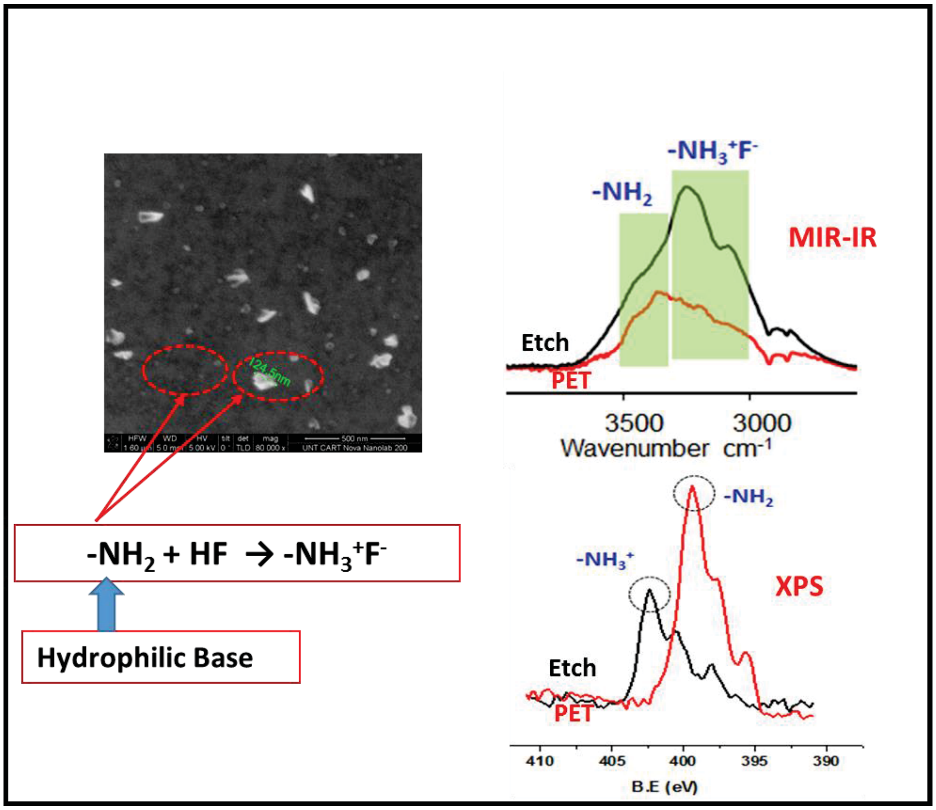

Figure 5.14 Proposed mechanism of TiN etch residue growth.

DIW rinse treatment still showed defects left on the surface (Figure 5.12) which suggests that ammonium component is not directly a part of metallic defects, however could play as a catalyzing medium for defect growth. The likely role of $–NH_3^+F^-$ formed in the reaction (equation 2) plays as a transporting agent of fluorine species to catalyze the partially oxidized TiN surface to induce metallic defects growth. The observance of no defects formed on N_2/CO PET suggests that optimized PET most likely has suppressed the catalytic role of $–NH_3^+F^-$ on the TiN surface. MIR-IR data also verifies the reduced intensity of $–NH_2$ and $-NH_3^+F^-$ after N_2/CO PET.

5.4 Summary

In this study, we have investigated the mechanism of residue growth on TiN hardmask after fluorocarbon etching. MIR-IR complemented by XPS and SEM show the presence of water soluble amine components which plays a significant role in the formation of etch residue defects. The new insights provided by MIR-IR on the amine component required for residue formation can be explored with new etch chemistries to prevent amine formation and the subsequent residue growth formation. Furthermore, we have also investigated the effect of different in-situ PETs and present that N_2 with high substrate temperature and N_2/CO based PETs limit or prevent the residue growth formation.

5.5 References

1. Tatsumi, T. *Appl. Surf. Sci*, **2007**, 253, 6716.
2. Maex, K.; Baklanov, M. R.; Shamiryan, D.; Iacopi, F.; Brongersma, S. H.; Yanovitskaya, Z. S. *J. Appl. Phys.* **2003**, 93, 8793.
3. Havemann, R. H.; Hutchby, J. A. *Proc. IEEE*. **2001**, 586.

4. Lin, Q.; Petrillo, K. Proc SPIE, 3678, High-resolution 248-nm bilayer resist. **1999**, 241.
5. Xie, Z.; Bodke, A.; Fu, J.; Jauhari, R.; Abdelrahman, M. *Applied Materials Inc.* **2007**.
6. Babich, K.; Mahorowala, A. "*Hardmask Technology for sub-100nm Lithographic Imaging*", Proc SPIE. **2003**, 5039, 152.
7. P. Ho et al. "Extending PVD copper barrier process beyond 65nm technology", Proceedings of 2005 Advanced Metallization Conference. **2005**.
8. Darnon, M.; Chevolleau, T.; Joubert.; Torres, J. *Appl. Phys. Lett*. **2007**, 91, 194103.
9. Posseme, N.; Chevolleau, T.; Bouyssou, R.; David, T.; Amal, V.; Barness, J. P.; Verove, C.; Joubert, O. *J. Vac. Sci. Technol. B* 28(4)VST B. **2011**, 29, 011018.
10. Kabansky, A. Y.; Tan, S. H.; Hudson, A.; Delgadino, G.; Gancs, L.; Marks, J. *ECS Trans*. **2013**, 58 (6), 143.
11. Matsuo, P. J.; Standaert, T. E. F. M.; Allen, S. D.; Oehrlein, G. S.; Dalton, T. J. *J. Vac. Sci. Technol*. *B*. **1999**, 17, 1435.
12. R. d'Agostino, F. Fracassi, and C. Pacifico, *J. Appl. Phys*. **1992**, 72, 4351.
13. Darnon, M.; Chevolleau, T.; Eon, D.; Vallier, L.; Torres, J.; Joubert, O. *J. Vac. Sci. Technol. B.* **2006**, 24, 2262.
14. Posseme, N.; Chevolleau, T.; Joubert, O.; Vallier, L.; Mangiagalli, P. *J. Vac. Sci. Technol. B.* **2003**, 21, 2432.
15. Maslennikova, I. G.; Laptash, N. M.; Kaidalova, T. A.; Kavun, V. Y. *Spectroscopy Letts.* **2001**, 34 (6), 775.
16. Posseme, N.; Chevolleau, T.; Bouyssou, R.; David, T.; Arnal, V.; Barnes, J. P.; Verove, C.; Joubert, O. *J. Vac. Sci. Technol. B.* **2010**, 28, 809.